9. SITE 844[1]

Shipboard Scientific Party[2]

HOLE 844A

Date occupied: 8 May 1991

Date departed: 9 May 1991

Time on hole: 15 hr, 33 min

Position: 7°55.279′N, 90°28.846′W

Bottom felt (rig floor; m, drill-pipe measurement): 3425.0

Distance between rig floor and sea level (m): 10.5

Water depth (drill-pipe measurement from sea level, m): 3414.5

Total depth (rig floor, m): 3434.5

Penetration (m): 9.5

Number of cores (including cores with no recovery): 1

Total length of cored section (m): 9.5

Total core recoved (m): 9.94

Core recovery (%): 104.6

   Oldest sediment cored:
   Depth (mbsf): 9.5
   Nature: clayey diatom ooze
   Earliest age: Pleistocene

HOLE 844B

Date occupied: 9 May 1991

Date departed: 11 May 1991

Time on hole: 2 days, 4 hr, 14 min

Position: 7°55.279′N, 90°28.846′W

Bottom felt (rig floor; m, drill-pipe measurement): 3425.0

Distance between rig floor and sea level (m): 10.5

Water depth (drill-pipe measurement from sea level, m): 3414.5

Total depth (rig floor, m): 3715.9

Penetration (m): 290.9

Number of cores (including cores with no recovery): 31

Total length of cored section (m): 290.9

Total core recoved (m): 289.92

Core recovery (%): 99.7

   Oldest sediment cored:
   Depth (mbsf): 290.8
   Nature: metalliferous nannofossil ooze
   Earliest age: lower Miocene

   Basement:
   Depth (mbsf): 290.8
   Nature: basalt

HOLE 844C

Date occupied: 11 May 1991

Date departed: 12 May 1991

Time on hole: 21 hr, 40 min

Position: 7°55.279′N, 90°28.846′W

Bottom felt (rig floor; m, drill-pipe measurement): 3425.0

Distance between rig floor and sea level (m): 10.5

Water depth (drill-pipe measurement from sea level, m): 3414.5

Total depth (rig floor, m): 3605.1

Penetration (m): 180.1

Number of cores (including cores with no recovery): 19

Total length of cored section (m): 180.1

Total core recoved (m): 189.34

Core recovery (%): 105.1

   Oldest sediment cored:
   Depth (mbsf): 180.1
   Nature: nannofossil ooze with diatoms
   Earliest age: middle Miocene

HOLE 844D

Date occupied: 12 May 1991

Date departed: 12 May 1991

Time on hole: 8 hr, 56 min

Position: 7°55.279′N, 90°28.846′W

Bottom felt (rig floor; m, drill-pipe measurement): 3425.0

Distance between rig floor and sea level (m): 10.5

Water depth (drill-pipe measurement from sea level, m): 3414.5

Total depth (rig floor, m): 3458.5

Penetration (m): 33.5

Number of cores (including cores with no recovery): 1

Total length of cored section (m): 9.5

Total core recoved (m): 10.12

Core recovery (%): 106.5

   Oldest sediment cored:
   Depth (mbsf): 33.5
   Nature: clayey diatom ooze
   Earliest age: late Miocene

Principal results: Site 844 (proposed EEQ-2) is located in the Guatemala Basin of the eastern equatorial Pacific Ocean. The oceanographic setting of the site is within the eastward flowing North Equatorial Countercurrent and in the region known as the Costa Rica Dome, where wind-induced shoaling of the thermocline produces surface upwelling and associated high open ocean productivity. The primary paleoceanographic objective of Site 844 was to provide a continuous Neogene record of these components of the equatorial current regime.

Four holes were drilled at the site. Hole 844A, a missed mud-line core was dedicated for detailed physical properties and interstitial-water geochemistry. Hole 844B was APC-cored to 185 mbsf, where excessive pullout required our switching to XCB-coring. The hole was continued to 291 mbsf, where basement was reached. Hole 844C was APC-cored to 181.5 mbsf. Coring in this hole was guided by real-time acquisition, in the sediment laboratory, of magnetic susceptibility and GRAPE-measured sediment density to assure our recovering a complete stratigraphic section. This procedure also indicated that a section of Hole 844B had been double-cored. To rectify this problem, one core was recovered between 24 and 33.5 mbsf in Hole 844D.

Using magnetic susceptibility, GRAPE density, and color spectral data from a newly developed core color-scanning instrument, we show that we recovered a continuous sequence of the upper 185 m of section from these combined three APC-cored holes.

The sediment sequence can be divided into two lithologic units. Unit I (0–68 mbsf) is a Pleistocene to middle Miocene clay-rich and biogenic silica-rich ooze with minimal carbonate. Unit II (68–290.8 mbsf) comprises nannofossil ooze with varying amounts of other microfossil groups and is middle to early Miocene in age.

Calcareous nannofossils, radiolarians, and diatoms generally are present throughout the sequence and provide a well-constrained biostratigraphy. Planktonic foraminifers are rare to absent in the upper 75 m, but are common to abundant through the remaining cored interval.

Paleomagnetic results from Site 844 show that a continuous and unambiguous paleomagnetic stratigraphy is contained in the section spanning the upper Miocene to the Pleistocene. All magnetic events, except for a short normal event at the base of Chron C4, were detected. The relatively good preservation of many of the fossil groups, combined with the paleomagnetic results, will make Site 844 an important stratigraphic reference section for the eastern equatorial Pacific Ocean.

We conducted three logging runs in Hole 844B using the standard lithostratigraphic string, a geochemical string, and the formation microscanner (FMS). Densities measured by the logs show a high degree of correlation with GRAPE densities and should provide a means for correlating log and sediment-measured properties.

Finally, this site was the first site where continuous (at 3-cm intervals) color spectral data were collected for all recovered core sections. These color spectral data consist of 511 channels that span visible and near-infrared wavelength bands, and these data will provide important new quantitative sedimentologic data. Each of the major sediment types found in Site 844 displays a distinct spectral pattern.

The combination of complete recovery, well-defined magnetostratigraphy and biostratigraphy; multiple, continuous high-resolution laboratory records (GRAPE, compressional-wave velocity, susceptibility, and color), and an excellent suite of logs ensure that Site 844 will be an important source for high-resolution paleoclimate and paleoceanographic studies.

BACKGROUND AND SCIENTIFIC OBJECTIVES

Site 844 was the first site drilled along a north-south transect across the eastern equatorial Pacific Ocean current system. The site is located within the eastward-flowing North Equatorial Countercurrent and in the area of the physical oceanographic feature known as the Costa Rica Dome, a shoaling of the thermocline (Fig. 1). This shoaling of the thermocline was first explained in terms of divergence, produced by the northward deflection of the North Equatorial Countercurrent by the Central American landmass (Wyrtki, 1965). Using compiled monthly tropical wind stress and a simple mass transport model, Hofmann et al. (1981) argued that the seasonal doming of the thermocline and associated upwelling are a result of local wind stress curl. The net effect of this upwelling is some of the highest open-ocean productivity in the world's oceans. Our primary paleoceanographic objective at this site was to document the history of the North Equatorial Countercurrent and the history of oceanic productivity in the Costa Rica Dome region during the Neogene.

Preliminary study of cores collected during the Leg 138 site-survey cruise demonstrated that the surface sediments in this region were siliceous clays with the potential of containing a good paleomagnetic record, as well as a good paleoceanographic record (in the siliceous microfossil assemblages). Foraminifers were present in some piston-core samples, but we did not attempt a more complete analysis for potential isotopic studies in the younger part of the section because they occurred rarely.

In addition to the general paleoceanographic objective outlined in Chapter 1, specific objectives for Site 844 include the following:

1. Calibration of equatorial biostratigraphies to the paleomagnetic time scale.
2. Evaluation of a sedimentary system containing all three end-member components used for physical and acoustical property studies and carbonate content modeling.
3. Establishment of a late Neogene record of the North Equatorial Countercurrent and Costa Rica Dome current regime.

Tectonic and Geographic Settings

Site 844 is located on the Cocos Plate, on basement formed at the East Pacific Rise approximately 18 m.y. ago (Hey et al., 1977; Fig. 2). Backtracking the site using poles of rotation based on a hot-spot reference frame (Duncan, pers. comm., 1990) suggests that the site always has been north of the equator. Based on the present position of oceanographic boundaries, this site has remained within the North Equatorial Countercurrent for at least the last 5 m.y.

Seismic and SeaBeam bathymetric data collected during the site-survey cruise (*Thomas Washington* Venture 1; see "Site Survey" chapter, this volume) reveal that the surficial topography in the region is minimal (20–30 m relief), with the exception of a small seamount 8 km southwest of the drill site. This local high rises 300 to 400 m above the surrounding seafloor (Fig. 3). While no local trend is seen in the topography; regionally, it trends northwest-southeast.

The area is a region of generally complex basement structure and disrupted and incoherent seismic reflections. Site 844 was selected at a spot where basement is relatively flat-lying and where coherent and well-stratified internal reflectors can be found (Fig. 4). The section at Site 844 is 0.355 s (two-way traveltime) thick and alternates from zones that are seismically transparent to those that are highly stratified (Fig. 4).

OPERATIONS

Panama to Site 844

JOIDES Resolution cast off the last line at 1348 hr (all times reported in Site 844 operations text are local time, L, or Universal Time Coordinated, UTC, minus 6 hr; all times reported in Table 1 are in UTC), 5 May 1991 and sailed west toward Site 844 (proposed Site EEQ-2). The 727 nmi to the first survey way point was covered at an average speed of 10.6 kt.

At 1000 hr, 8 May, a site survey for Site 844 was begun (see "Underway Geophysics" chapter, this volume, for more details of the site survey). A beacon was deployed at 1437L 8 May, and the survey was concluded at 1524L 8 May. Based upon the precision depth recorder (PDR), depth to the seafloor is 3430 mbrf.

Holes 844A and 844B

Core 138-844A-1H was recovered at a depth of 3425 mbrf at 0540 hr, 9 May. From this core, we recovered more than 9.5 m of sediment (9.94 m) and, consequently, could not use it to establish the mud line. To establish the mud line, the pipe was pulled above the seafloor to start a second hole. Hole 844A was terminated at 0600 hr, 9 May, when the bit cleared the mud line. The ship was offset 20 m, and Hole 844B began successfully when Core 138-844B-1H was recovered at 0630 hr, 9 May.

Cores 138-844B-1H through -3H were recovered successfully from 0 to 23.5 mbsf (Table 1). Orientation began with Core 138-844B-4H;
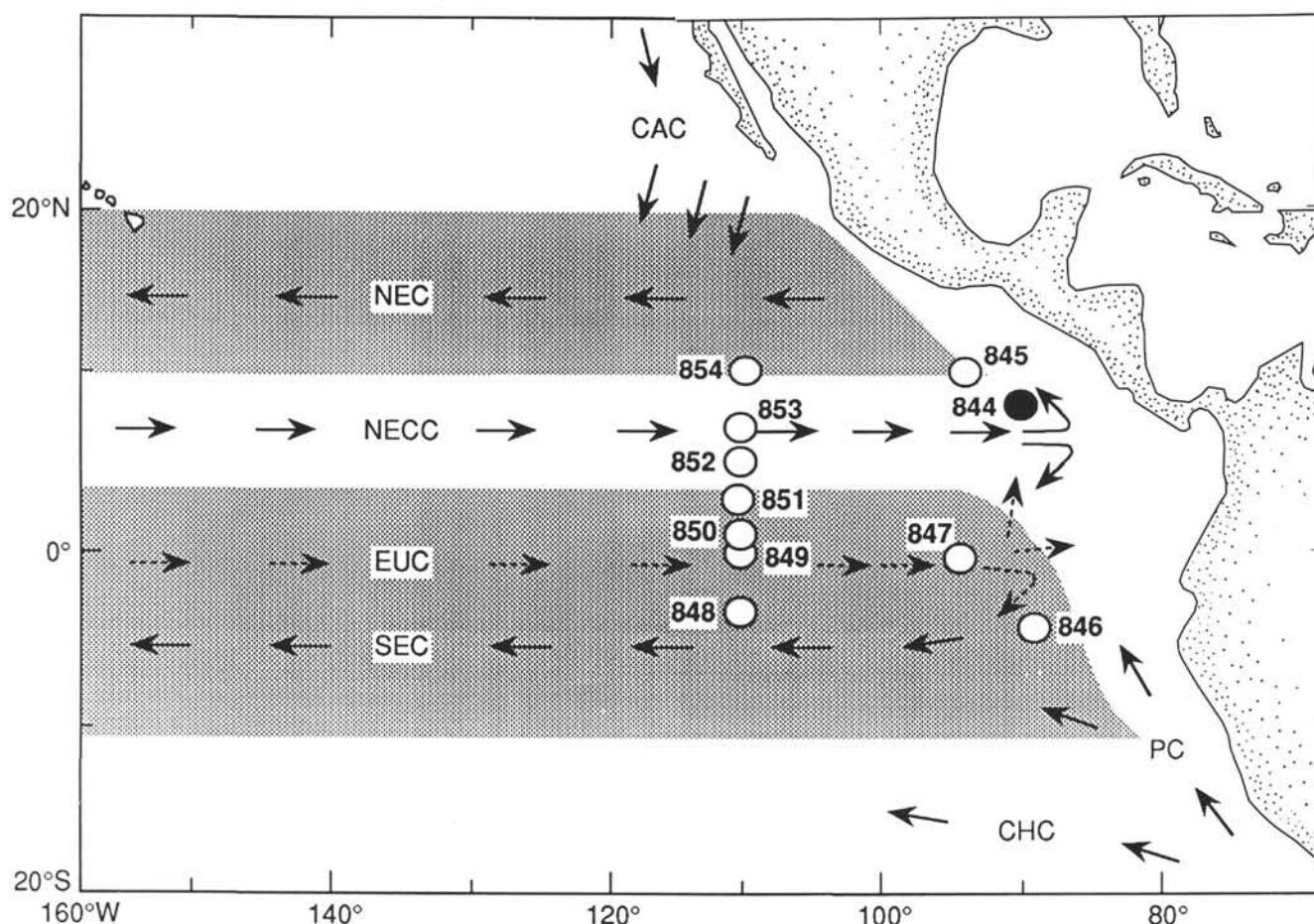
Figure 1. Site location and generalized circulation system of the eastern equatorial Pacific Ocean. Surface current shown as solid arrows, subsurface current as dashed arrows. CAC = California Current; NEC = North Equatorial Current; NECC = North Equatorial Countercurrent; EUC = Equatorial Undercurrent; SEC = South Equatorial Current; PC = Peru Current; and CHC = Chile Current.

the pipe was not advanced after Core 138-844B-3H was recovered. As a result, the same sedimentary interval was cored again with Core 138-844B-4H. The pipe was then advanced 19 m before Core 138-844B-5H (33.0–42.5 mbsf) was recovered. Cores 138-844B-6H through -19H were recovered over the interval from 42.5 to 175.5 mbsf. Approximately 150,000 lb of overpull was required to retrieve Core 138-844B-20H, which forced the termination of the APC-coring program for this hole. Average sediment recovery for the APC section at Hole 844B was 104.7%.

Coring was resumed using the XCB system at Core 138-844B-21X, and pipe was advanced without incident to 290.9 mbsf (Core 138-844B-31X), where contact with basaltic basement was confirmed by the recovery of 10 cm of basalt. The depth objective for the hole was reached at this point, and the seismologists began to prepare for logging. The average recovery for the XCB section of Hole 844B was 90.8%. Recovery for the entire hole was 99.7%.

Downhole Measurements (Hole 844B)

After sweeping the hole with mud, pipe was pulled back to a logging depth of 71.9 mbsf, when the seismologists began downhole measurements (see "Downhole Measurements" section, this chapter, for more details of logging operations). Hole 844B was logged with the three standard ODP tool strings. A summary of these operations can be found in Table 2. All logging tools performed well, but getting

them in or out of the pipe proved problematic during two of the logging runs.

During the first run with the geophysical string, problems developed with this tool when getting it out of the base of the drill string during both the main and repeated logging passes. During the main pass, the logging string jammed about 15 m above the bit, within the bottom-hole assembly (BHA). After careful pumping, the drillers were able to free the tool string and the seismologists to log the hole to 285.9 mbsf, 5 m above the total depth drilled. At the base of the hole, the wireline heave compensator broke down and could not be restarted. Because the seas were calm, the absence of the heave compensator did not significantly affect logging results. Logging up the hole was successful. During the repeat pass (156.5.9–83.2 mbsf), the tool string would not pass the bit as it was lowered. Another stand of pipe was lowered, which broke through the obstruction, allowing the logging string to reenter the open hole.

The first geochemical log was run from 289.6 mbsf to the mud line, with measurements taken through pipe. No operational problems were encountered during this logging run.

The FMS tool was used to log the section from 290.5 to 65 mbsf and again from 156.5 to 65 mbsf. No problems were encountered until the tool was brought into the drill pipe. Apparently, the lockable flapper valve on the XCB bit had unlatched and was blocking the tool string from reentering. Again, with gentle pumping, the drillers were able to pull the tool string into the pipe.
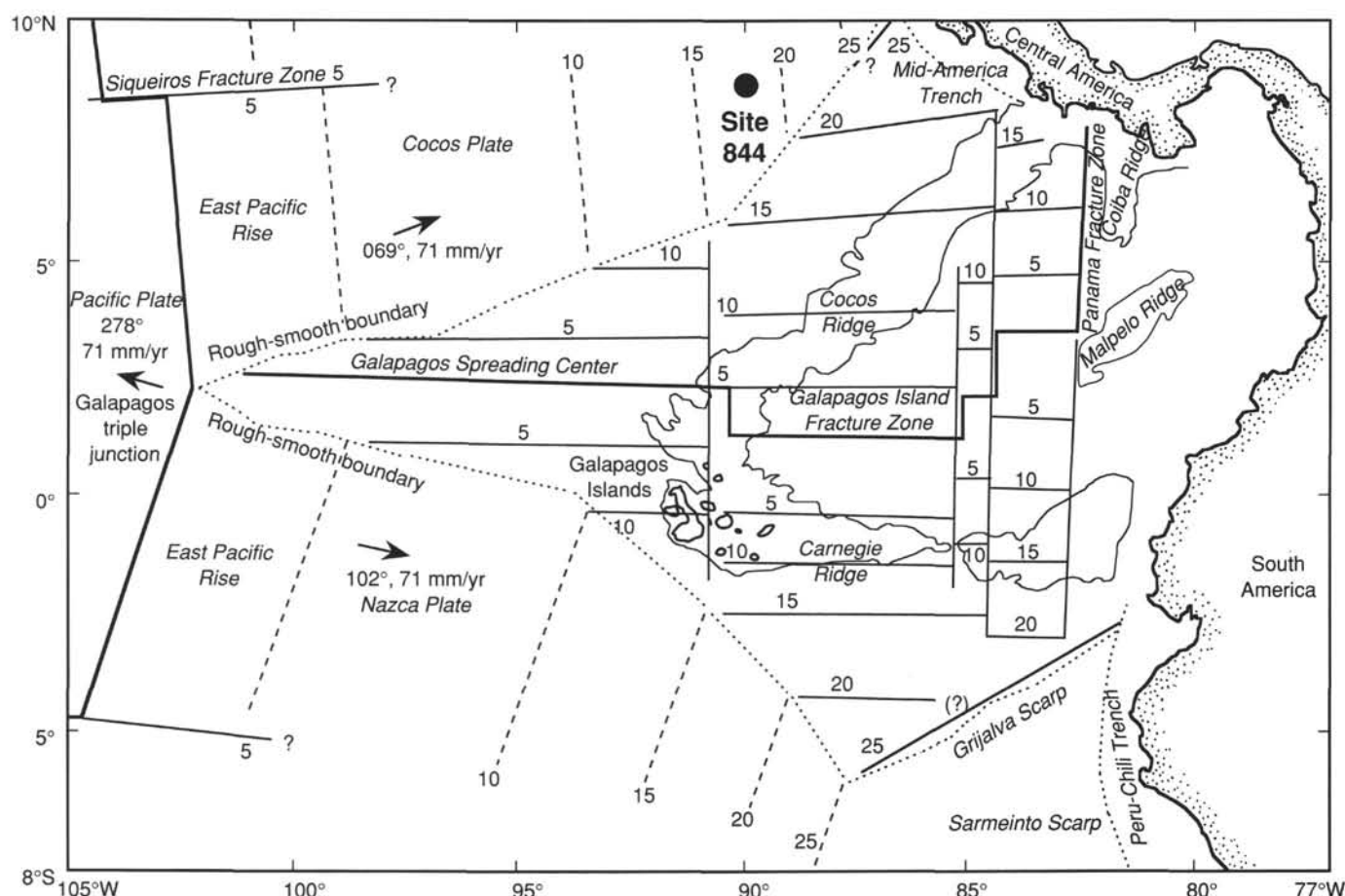
Figure 2. Tectonic setting and basement ages for the eastern equatorial Pacific Ocean (from Hey et al., 1977) and location of Site 844.

At the conclusion of the logging program, all tools were recovered and the derrick was rigged down from logging. Then, the pipe was pulled out of the hole and it cleared the mud line at 1024L 11 May, ending Hole 844B.

Hole 844C

The vessel was offset 20 m south, and Hole 844C began when Core 138-844C-1H was recovered at 1145L 11 May. Eighteen APC cores (0–170.6 mbsf) were recovered successfully, with orientation beginning in Core 138-844C-4H. The core barrel became stuck in the hole after Core 138-844C-19H (170.6–180.1 mbsf) was recovered. After washing 6 m over the barrel and applying 130,000 lb of overpull, the drilleres were able to retrieve the core barrel. Coring operations were concluded in Hole 844C after the recovery of Core 138-844C-19H. At this point, the pipe was pulled out of the hole; the bit cleared the mud line at 0804L 12 May, thereby ending Hole 844C. Recovery for Hole 844C was 105.1%.

Hole 844D

To recover the sedimentary interval missed during coring at Hole 844B, the vessel was offset 20 m west, and Hole 844D was washed down to 24 mbsf. A single core, 138-844D-1H, was recovered over the interval from 24.0 to 33.5 mbsf, with a recovery of 10.12 m of sediment (106.5%). After retrieval of Core 138-844A-1H, the pipe was pulled to the surface, and the bit reached the drill floor at 1622L 9 May, thereby ending Hole 844D.

The beacon was successfully retrieved at 1345L 12 May, after its leisurely ascent from the seafloor at a rate of 40 m/min. At 1700L 9 May, the vessel began its transit to the next site, officially ending Site 844.

LITHOSTRATIGRAPHY

Introduction

The sediments at Site 844 are biogenic oozes, with minor intervals of clay-rich sediment (Fig. 5) The entire sediment column was recovered above basalt basement. The sediments become more calcareous with depth, but show considerable variation in lithology. Calcareous nanno-fossils dominate the calcareous sediment fractions, but some intervals of siliceous sediment are dominated by both radiolarians and diatoms.

While describing the sediments of Site 844, the sedimentologists were fortunate to have available data for lithologic parameters that are continuously measured during core processing (including density and magnetic susceptibility), as well as data from an automated color analysis system (Fig. 6). These data were used together with normal sedimentological criteria (percentages of microfossil and mineral groups in smear slides, sedimentary structures, color, and general appearance) to divide the sediment column into lithologic units.

Because the sediments at the site were primarily biogenic oozes, the primary density contrast was between calcite and biogenic silica. The density of calcite ($\rho = 2.6$–2.7) is greater than that of biogenic silica/silicate minerals ($\rho = 2.1$–2.3), and biogenic calcite also is more closely packed in deep-sea sediments than is biogenic silica (Mayer, 1991). Thus, these continuously recorded bulk density measurements (GRAPE) provided a first-order estimate of carbonate content that
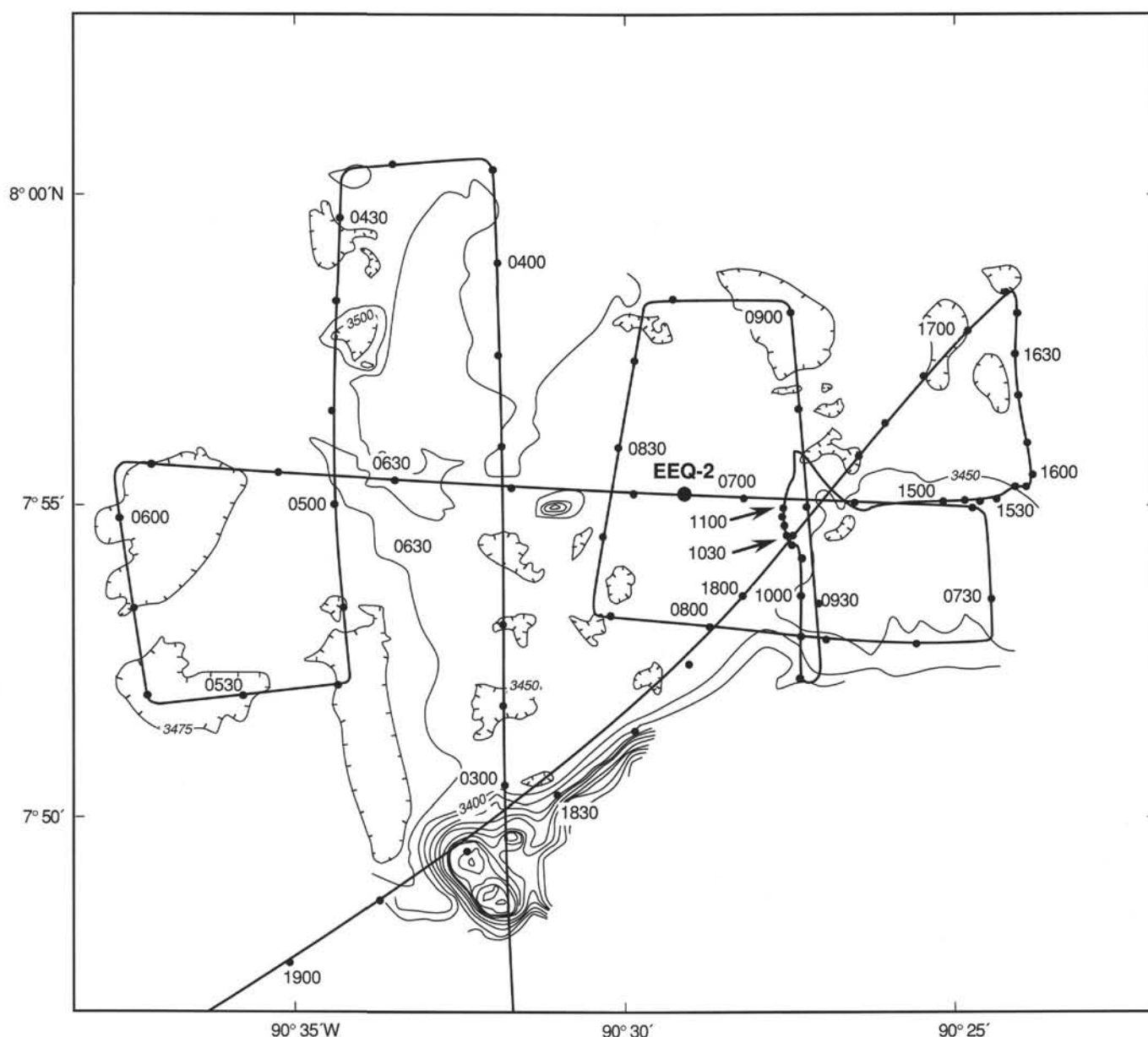
Figure 3. SeaBeam map, hand-contoured from navigation-adjusted SeaBeam contour maps that were collected on the *Thomas Washington* during the Venture 1 cruise, September 1989. Location of proposed Site EEQ-2 is shown.

supplemented our direct observations from smear slides and chemical analyses (see "Inorganic Geochemistry" section, this chapter).

The three data channels from the automated color analysis system that are included on the barrel sheet as "% reflectance" indicate averages across intervals from 450 to 500 nm (blue), 650 to 700 nm (red), and 850 to 900 nm (near-infrared) reflectance bands. All three vary with lithology (Fig. 6). To first approximation, average reflectance varies because of carbonate content. Darker layers that were diatom- or radiolarian-rich in the core generally had lower reflectance in the visible part of the spectrum than in the near-infrared part (Fig. 6B). Comparison of these bands helped to identify the exact boundaries among these lithologies even when they were not visually distinct.

The color and density measurements were found to be particularly useful for identifying lithologic variation within sedimentary units of very high concentrations of calcium carbonate. Such variations are generally subtle and can be difficult to discern visually.

Correlations among holes were performed on the basis of matching density, magnetic susceptibility, and continuously measured color data, as well as on the basis of sedimentological features. These data were used to help identify coring gaps, intervals that had been cored twice, and overlaps among holes. We have mentioned major gaps and duplications in our descriptions of lithology. A composite description of the entire site (Fig. 7) shows the relationship among lithologies and the continuously measured parameters.

The sediments from Site 844 were divided into two lithologic units (Fig. 5), primarily on the basis of carbonate content. Unit I is a biogenic silica and clay-rich unit having a few carbonate-rich intervals. Unit II is dominated by carbonate.
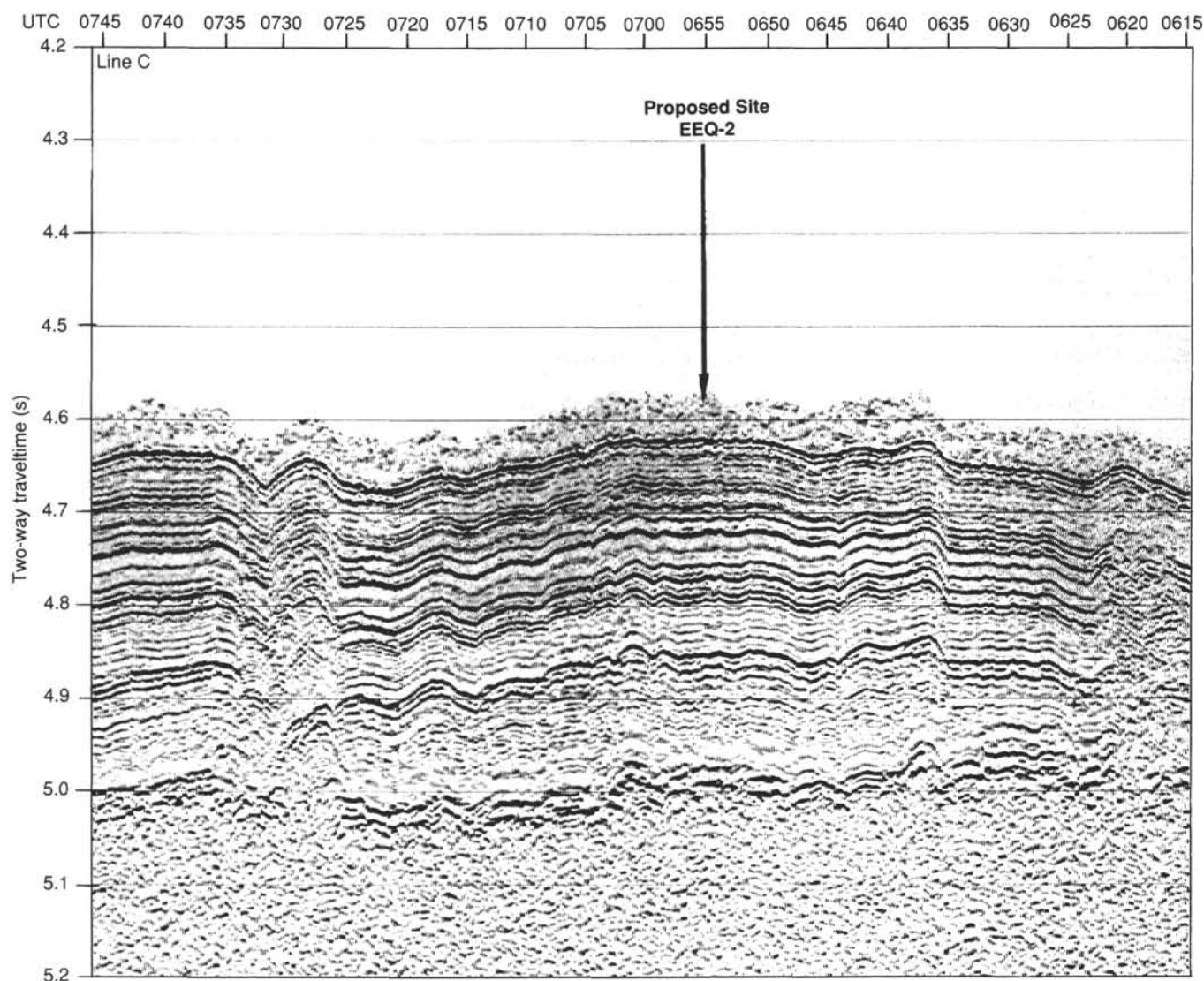
Figure 4. Seismic Line C, 80-in.^{3} water-gun record collected during the *Thomas Washington* Venture 1 cruise. Location of proposed Site EEQ-2 is shown.

Description of Units

Unit I

Intervals:
  Hole 844A, Core 138-844A-1H
  Hole 844B, Cores 138-844B-1H through -8H-6
  Hole 844C, Cores 138-844C-1H through -8H-1
  Hole 844D, Core 138-844D-1H
Age: Pleistocene to middle Miocene
Depth: 0–67.7 mbsf, Hole 844B; 68.7 mbsf, Hole 844C

The siliceous and clay-rich sediments of Unit I were divided into two subunits. Subunit IA is Pleistocene to Pliocene, siliceous and clay-rich sediments. The dominant siliceous microfossil group is diatoms, which represent 40% to 60% of the sediment (smear-slide descriptions have been tabulated as an appendix following the visual core descriptions). Subunit IB comprises upper Miocene to middle Miocene, alternating siliceous and calcareous sediments. The siliceous intervals generally are diatom-rich, although one extremely radiolarian-rich interval does occur. The calcareous intervals are nannofossil-rich. Clay is a minor component.

Subunit IA

Intervals:
  Hole 844A, Core 138-844A-1H1
  Hole 844B, Cores 138-844B-1H through -4H-7 (except for-3H-6, see text)
  Hole 844C, Cores 138-844C-1H through -3H-3
Age: Pleistocene to upper Pliocene
Depth: 0–22.5 mbsf, Hole 844B; 22.3 mbsf, Hole 844C

Subunit IA contains ~22.5 m of clayey diatom ooze, clayey nannofossil diatom ooze, and clayey radiolarian diatom ooze and diatomaceous clay. The proportion of clay varies, but rapidly increases to more than 70% in the basal 1.5 m of the subunit (Fig. 8). Few foraminifers and only traces of calcareous nannofossils can be seen, except between 6 and 15 mbsf (Hole 844B), where abundances of calcareous nannofossils range up to 10%. The only other lithology is a pale gray vitric ash in Sections 138-844A-1H-1 (19–24 cm), -844B-1H-1 (120–126 cm), -844C-1H-1 (99–101 cm), and an ash-rich layer associated with some fine laminations at Section 138-844B-3H-2 at 0 to 40 cm. Some discrete color bands and isolated groups of bluish-gray laminations also occur. These are of a similar color to

Table 1. Summary of coring operations at Site 844.

Core no.	Date (May 1991)	Time (UTC)	Depth (mbsf) (m)	Length cored (m)	Length recovered	Recovery (%)
Hole 844A-1H	9	1140	0–9.5	9.5	9.94	104.0
Coring totals				9.5	9.94	104.0
Hole 844B-1H	9	1230	0–4.5	4.5	4.53	100.0
2H	9	1340	4.5–14.0	9.5	9.98	105.0
3H	9	1430	14.0–23.5	9.5	10.05	105.8
4H	9	1525	23.5–33.0	9.5	9.98	105.0
5H	9	1620	33.0–42.5	9.5	9.90	104.0
6H	9	1710	42.5–52.0	9.5	10.02	105.5
7H	9	1815	52.0–61.5	9.5	10.06	105.9
8H	9	1915	61.5–71.0	9.5	9.94	104.0
9H	9	2015	71.0–80.5	9.5	10.10	106.3
10H	9	2155	80.5–90.0	9.5	9.77	103.0
11H	9	2255	90.0–99.5	9.5	9.99	105.0
12H	9	2355	99.5–109.0	9.5	10.09	106.2
13H	10	0055	109.0–118.5	9.5	9.95	105.0
14H	10	0150	118.5–128.0	9.5	9.76	103.0
15H	10	0255	128.0–137.5	9.5	9.82	103.0
16H	10	0355	137.5–147.0	9.5	9.93	104.0
17H	10	0445	147.0–156.5	9.5	10.07	106.0
18H	10	0550	156.5–166.0	9.5	9.93	104.0
19H	10	0645	166.0–175.5	9.5	9.83	103.0
20H	10	0755	175.5–185.0	9.5	10.08	106.1
21X	10	0950	185.0–194.6	9.6	9.69	101.0
22X	10	0950	194.6–204.3	9.7	9.67	99.7
23X	10	1035	204.3–213.9	9.6	9.60	100.0
24X	10	1125	213.9–223.6	9.7	9.75	100.0
25X	10	1220	223.6–233.3	9.7	8.44	87.0
26X	10	1305	233.3–242.9	9.6	9.76	101.0
27X	10	1350	242.9–252.6	9.7	0.40	4.1
28X	10	1445	252.6–261.9	9.3	9.06	97.4
29X	10	1535	261.9–271.6	9.7	9.85	101.0
30X	10	1630	271.6–281.2	9.6	9.87	103.0
31X	10	1755	281.2–290.9	9.7	10.05	103.6
Coring totals				290.9	289.92	99.7
Hole 844C-1H	11	1745	0–9.1	9.1	9.10	100.0
2H	11	1845	9.1–18.6	9.5	9.52	100.0
3H	11	1945	18.6–28.1	9.5	10.06	105.9
4H	11	2045	28.1–37.6	9.5	10.08	106.1
5H	11	2145	37.6–47.1	9.5	9.96	105.0
6H	11	2240	47.1–56.6	9.5	10.10	106.3
7H	11	2345	56.6–66.1	9.5	10.13	106.6
8H	12	0035	66.1–75.6	9.5	10.20	107.3
9H	12	0140	75.6–85.1	9.5	10.18	107.1
10H	12	0300	85.1–94.6	9.5	9.82	103.0
11H	12	0355	94.6–104.1	9.5	10.06	105.9
12H	12	0455	104.1–113.6	9.5	10.05	105.8
13H	12	0550	113.6–123.1	9.5	10.02	105.5
14H	12	0645	123.1–132.6	9.5	9.61	101.0
15H	12	0815	132.6–142.1	9.5	10.20	107.3
16H	12	0910	142.1–151.6	9.5	10.06	105.9
17H	12	1005	151.6–161.1	9.5	9.90	104.0
18H	12	1120	161.1–170.6	9.5	10.09	106.2
19H	12	1330	170.6–180.1	9.5	10.20	107.3
Coring totals				180.1	189.34	105.1
Hole 844D-1H	12	1640	24.0–33.5	9.5	10.12	106.5
Coring totals				9.5	10.12	106.5

some rinds around burrows. A distinctive 15-cm horizon containing green granular smectite, ash, and associated bluish laminations occurs in Sections 138-844B-3H-2 (15–32 cm) and -844C-2H-6 (0–20 cm).

Dominant colors are shades of greenish-gray that are variegated and mottled throughout (10Y 5/1, 10Y 5/2 to 10Y 6/2 and 5GY 9/1). The topmost 52 cm is mottled dark olive green to brown (5Y 3/2). The dominant color changes gradationally to light tan (10YR 5/6) toward the base of the subunit. The upper 15 m, especially, contains

mottles and some subvertical streaks of bluish-gray. This color also is characteristic of scattered thin banding and lamination observed and the outer ring of rind burrows. This subunit has the lowest percentage of reflectance of any of the sediments at the site, and the overall greenish color of the subunit is indicated by its strong reflectance in the blue (450–500 nm) band (Fig. 7).

Bioturbation is common throughout. The most common trace fossils are rind burrows and *Planolites*. Individual *Zoophycos* bur-

125

Table 2. Summary of logging operations at Site 844.

Date (local; May 1991)	Time (local)	Cumulative (hr)	Depth (mbsf-base of string)	Procedure
10	1200	0.0		Last core on deck
10	1500	3.0		Start rig up
10	1700	5.0		Quad tool rigged up (NGT/SDT/HLDT/DIT/TLT); going down
10	1830	6.5		Stuck in pipe about 15 m above drill bit
10	1930	7.5		Pumped obstruction clear, go out into open hole
10	2005	8.1	285.9	At TD, start main log up
10	2051	8.9	83.2	Stop up-going log, go in pipe
10	2100	9.0		Hole plugged when trying repeat
10	2120	9.3	156.5	Broke into open hole by lowering stand; repeat section up to pipe
10	2130	9.5	83.2	End repeat, POOH
11	0049	12.8		RIH w/ Geochem String (NGT/ACT/GST/TLT); going down
11	0205	14.1	289.6	At TD; start logging up to mudline at 600'/hr
11	0355	15.9	0.0	Enter pipe and log to mudline; then POOH
11	0500	17.0		Geochemical String at rig floor, post-calibration
11	0600	18.0		RIH w/FMS string (NGT/GPIT/FMS/TLT).
11	0720	19.3	290.5	At TD, start FMS main log up the hole.
11	0750	19.8	65.0	Stop main log; drop back to 156.5 mbsf for repeat section
11	0755	19.9	156.5	Start repeat FMS log
11	0805	20.1	65.0	Stop repeat FMS log
11	0805	20.1		POOH; trouble getting back into pipe because of flapper valve
11	1030	22.5		Rigged down from logging

rows occur between 9 and 12 mbsf. Near the base of this subunit in Section 138-844B-3H-3 at 82 cm (17.82 mbsf, Hole 844B), a prominent horizon of truncated burrows shows evidence of erosion. The base of Subunit IA was taken at the burrowed top of a distinctive 45-cm-thick bed of nannofossil ooze at Sections 138-844B-3H-6, -844B-4H-CC, and -844C-3H-4 (22.53 mbsf in Hole 844B; 22.35 mbsf in Hole 844C).

The lower portion of Subunit IA recovered in Core 138-844B-3H was re-cored in Core 138-844B-4H. The last section of Core 138-844B-3H (7) is sediment assigned to Subunit IB; however, all of Core 138-844B-4H in Hole 844B is material from Subunit IA.

Subunit IB

Intervals:
Hole 844B, Sections 138-844B-3H-6 and -5H-1 through -8H-6
Hole 844C, Sections 138-844C-3H-4 through -8H-1
Hole 844D, Core 138-844D-1H
Age: Pliocene to middle Miocene
Depth: 22.5–67.7 mbsf, Hole 844B; 22.3–68.7 mbsf, Hole 844C

Subunit IB is characterized by an alternation on a variety of scales of carbonate-rich and siliceous and/or clay-rich lithologies. Most of the upper ~9 m of this subunit was not recovered in Hole 844B; therefore, our description of the upper portion of the subunit is based on Hole 844C. The top 15 m (22.3–37.3 mbsf, Hole 844C) comprises alternations on a meter-scale of radiolarian diatom clay and foraminifer nannofossil ooze. Below this interval, to approximately 47 mbsf, an alternation of lightly bioturbated light brown to light gray nannofossil ooze and heavily bioturbated brown to light greenish-brown radiolarian diatom ooze is present. In Cores 138-844B-6H-5 to 7H-4 and -844C-6H-1 to -CC (47–56 mbsf), a radiolarian-rich (commonly >50%) sequence is punctuated by a minor (1.5 m) interval of diatom nannofossil ooze. A distinctive bed of very dark grayish-brown burrowed radiolarian ooze (Fig. 9) occurs in the middle of this sequence in Sections 138-844B-7H-1 at 60–90 cm (52.60–52.90 mbsf) and -844C-6H-4 at 123 cm (52.74 mbsf). This interval is characterized by high water content and low density (see "Physical Properties" section, this chapter). X-ray diffraction analyses indicate that these clay-rich intervals are dominated by smectite, with minor amounts of quartz and plagioclase feldspar and traces of illite.

Below 56 mbsf, little clay is seen, and the lithology is a white to light bluish-gray nannofossil ooze interbedded with greenish-gray nannofossil diatom ooze. This nannofossil ooze is similar to that in Unit II (below). The base of the subunit is at Sections 138-844B-8H-6, 95 cm, and -844C-8H-2, 15 cm, where the first darker diatom-rich sediment occurs.

Dominant colors, as with lithologies, are variable, and decimeter- to meter-scale color banding is common. In the top 3 m of diatom-rich clay, a decimeter-scale alternation of very pale brown and dark grayish brown is seen (10YR 8/3 and 10YR 4/2). The nannofossil ooze between ~20 and 40 mbsf ranges from light brown to light gray (5Y 6/2 to 5Y 7/1), while the interbedded diatom ooze is brown to very pale brown (10YR 5/3 to 10YR 7/2). Below about 57 mbsf, the nannofossil ooze is light bluish-gray to light greenish-gray (5B 7/1 to 5G 7/1). The radiolarian ooze at 52.8 mbsf (Hole 844B) is very dark grayish-brown (2.5Y 3/2) and has a distinctive signature on the color reflectance records from both Hole 844B and 844C (Fig. 6). Purplish and dark-bluish hues (indicating pyrite or monosulfides) are associated with rings around burrows, burrow fill, and faint lamination below 48 mbsf. The percentage of reflectance of sediments above 48 mbsf is highly variable, with amplitude changes of up to 50% reflectance.

Bioturbation is moderate to strong throughout. Burrows are more common (or more clearly visible) in some of the darker brownish bands. Solid burrows, *Skolithos, Planolites,* and *Zoophycos* are all common. Rind burrows are rare, and burrows having purplish rings or haloes are not present between 17 and 48 mbsf. *Zoophycos* burrows are particularly abundant in the radiolarian oozes between 41 and 55 mbsf (Fig. 10).

Unit II

Intervals:
Hole 844B, Sections 138-844B-8H-6 through -31X-CC
Hole 844C, Sections 138-884C-8H-2 through -19H-CC (base of hole)
Age: middle to early Miocene
Depth: 67.7–290.8 mbsf, Hole 844B; 68.7–180.1 mbsf, Hole 844C

Unit II comprises nannofossil ooze with varying amounts of other microfossil groups. The amount of foraminifer-rich sediment increases with depth. Nannofossil diatom ooze is a significant minor component preserved mainly in burrow fills, but also is seen in laminated intervals at 69.5 to 72 mbsf (Hole 844B; 67.7–72.4 mbsf,

Hole 844C), 109–111 mbsf (Hole 844C), 128–129 mbsf (Hole 844C). The average concentration of $CaCO_3$ in the subunit is 80% (see "Organic Geochemistry" section, this chapter). The percentage of reflectance of this sedimentary subunit is much less variable than that of Subunit IB.

Subunit IIA

Intervals:
Hole 844B, Cores 138-844B-8H-6 through -17H-4
Hole 844C, Sections138-884C-8H-2 through -18H-1
Age: middle Miocene
Depth: 67.7–151 mbsf, Hole 844B; 68.7–148.5, Hole 844C

Subunit IIA contains about 75 m of diatom nannofossil ooze, nannofossil ooze, and clayey diatom nannofossil ooze. The nannofossil content of the sediment estimated from smear slides is 60% to 80%. The average concentration of $CaCO_3$ in the subunit is 80%. Diatoms generally are the most abundant siliceous microfossil group in the subunit (10%–15%), but radiolarians are present (<5%). Foraminifers also are present (<5%).

At about 106 mbsf (Hole 844B; 108 mbsf in Hole 844C), the diatom content of the sediment increases. The sediment between 107 and 113 mbsf (Hole 844B; 108–111.5 mbsf in Hole 844C) and between 127 and 128 mbsf (Hole 844B; 127–128 mbsf in Hole 844C) is a nannofossil diatom ooze (diatoms 50%) that has an average concentration of $CaCO_3$ of 55%. Two distinctive intervals of diatom ooze and nannofossil diatom ooze are very finely laminated: Sections 138-844B-8H-6 through -9H-2 and Sections 138-844C-8H-2 through -8H-5 (69.5–72.3 mbsf, Hole B; 67.7–72.9 mbsf, Hole C). Ash pods occur in Sections 1, 3, and 6 of Core 138-844B-11H (81–89 mbsf).

The subunit is very light gray in color (N8) and has the highest average percentage of reflectance values in the core (Fig. 6). The sediment is subtly mottled throughout, with slightly lighter and darker shades of gray. Superimposed on this mottling are distinct solid burrows that are slightly yellower (5Y 8/1) and more diatom-rich than the dominant sediment. In addition, purple to grayish-purple and faint green color mottling and banding can be seen (5YR 8/1, 5GY 8/1, and 5B 8/2), presumably because of reduction diagenesis. The diatom-rich burrows often have purplish and greenish diagenetic haloes. The sediment within many small burrows has undergone extensive diagenesis and contains fine-grained pyrite. The most common trace fossils are solid burrows. Isolated individual *Zoophycos* burrows occur at 113 mbsf (Hole 844B). With the exception of the diatom-rich intervals, the subunit has uniform lithology, appearance, and color. Its reflectance is the most uniform of any portion of the sediment at the site, and is generally between 50% and 60%.

The nannofossil diatom ooze between 69.5 and 72.3, 107 and 113, and 127 and 128 mbsf (Hole 844B; 67.7–72.9, 109–111.5, and 127–128 mbsf, Hole 844C) is darker (5Y 7/2) in color than the nannofossil ooze. The darker colors of this lithology appear distinctly in the percentage of reflectance of the core (Fig. 6). The oozes in this interval are more strongly banded (and more weakly bioturbated) than the nannofossil oozes above and below.

The transition to the subunit below is marked by a distinct increase in the concentration of foraminifers and a decrease in the percent reflectance.

Subunit IIB

Intervals:
Hole 844B, Sections 138-844B-17H-5 to -31X-CC
Hole 844C, Sections 138-844C-18H-2 to -19H-CC
Age: middle to early Miocene
Depth: 151–290.8 mbsf, Hole 844B; 148.5–180.1 mbsf, Hole 844C

Subunit IIB contains 139.8 m (Hole 844B) of foraminifer nannofossil ooze. Hole 844C did not reach the base of the unit. Estimates from smear slides suggest that the nannofossil content of the sediment is about 60%. Diatoms are the most abundant siliceous microfossil group in the subunit (5%–10%); radiolarians are present in trace quantities. The concentration of foraminifers in the subunit ranges from 10% to 25%, but increases with depth from about 10% at the top of the subunit to about 20% at the bottom of the subunit and unit. Between 175 and 195 mbsf (Hole 844B), several intervals of more diatom-rich (up to 25%) and clay-rich (up to 15%) sediment can be seen. The sediment in these intervals has carbonate contents of 55% to 60%.

Subunit IIB is very light gray in color (N8) at the top, then grades to very light greenish-gray (5G 9/1) toward the bottom. A gradual decrease in percentage of reflectance accompanies this color change. Like the sediments of Subunit IIA, this ooze is subtly mottled with lighter and darker shades of gray and is also mottled and subtly banded with faint purplish and greenish colors resulting from organic matter diagenesis. Fewer mottles and burrows filled with the dark purplish gray (5PB 4/2) color (associated with fine-grained pyrite in the sediment) can be seen in this subunit than in Subunit IIA.

Cores 138-844-26X to -31X (233.3–290.9 mbsf) were split by saw, rather than wire. The bioturbation features and trace fossils were clearer in these cores than in the wire-cut cores. *Planolites, Chondrites,* individual *Zoophycos,* and rind burrows are present to common in these cores (see "Trace Fossils" section, this chapter).

An abrupt color change to light reddish-brown (5YR 6/4) diatom nannofossil ooze occurs at a depth of 32 cm in the core-catcher section (138-844B-31X-CC). Sediments near the basal contact show evidence of redeposition, including conglomeratic horizons (Fig. 11A). The contact between the two sediment types was fractured.

Based on its occurrence near basalt basement, its color, chemistry, and the presence of reddish semi-opaque oxides in smear slides, we interpreted this light reddish-brown sediment as metalliferous sediment. X-ray diffraction analyses indicate only the presence of plagioclase feldspar (Na-intermediate anorthite), calcite, and quartz. The metalliferous sediment grades downward into very light gray (N8) diatom nannofossil ooze near a depth of 30 cm in the core-catcher sample. Below a depth of 30 cm in the core-catcher sample, a 10-cm-thick interval of dark greenish-gray clayey nannofossil ooze can be seen to overlie basalt (Fig. 11B).

Trace Fossils

Trace fossils encountered in the sediments are recorded in detail on individual core barrel sheets. Bioturbation is common to abundant throughout the sediments recovered in Site 844. Two distinct ichnofacies were identified. The trace fossils typical of Unit I are solid burrows, rind burrows, *Planolites* and common to locally abundant *Zoophycos* (Fig. 12). *Chondrites* is very rare and was observed only in carbonate-rich sections. The carbonate-rich lithologies of Subunit IB are characterized by the presence of common *Chondrites* that commonly cut *Skolithos,* solid burrows, rind burrows, and *Planolites.*

The only intervals in which we did not observe bioturbation were thin intervals of laminated diatom ooze and nannofossil diatom ooze at 68 to 72, 109 to 112, and 128 to 129 mbsf (Hole 844B, Fig. 13). Burrows are cut by common dark purplish lamination (Fig. 14), indicating that this type of lamination must have formed later than the bioturbation.

Color Banding and Lamination

Color banding and lamination are common in much of the sediment recovered at Site 844. Both banding and lamination can be divided into three broad types: (1) depositional banding and lamination (associated with variation in type of sediment supplied); (2) pre-bioturbation redox banding, which may also be associated with variation in sediment supply; and (3) early diagenetic (post-bioturbation) lamination and banding.
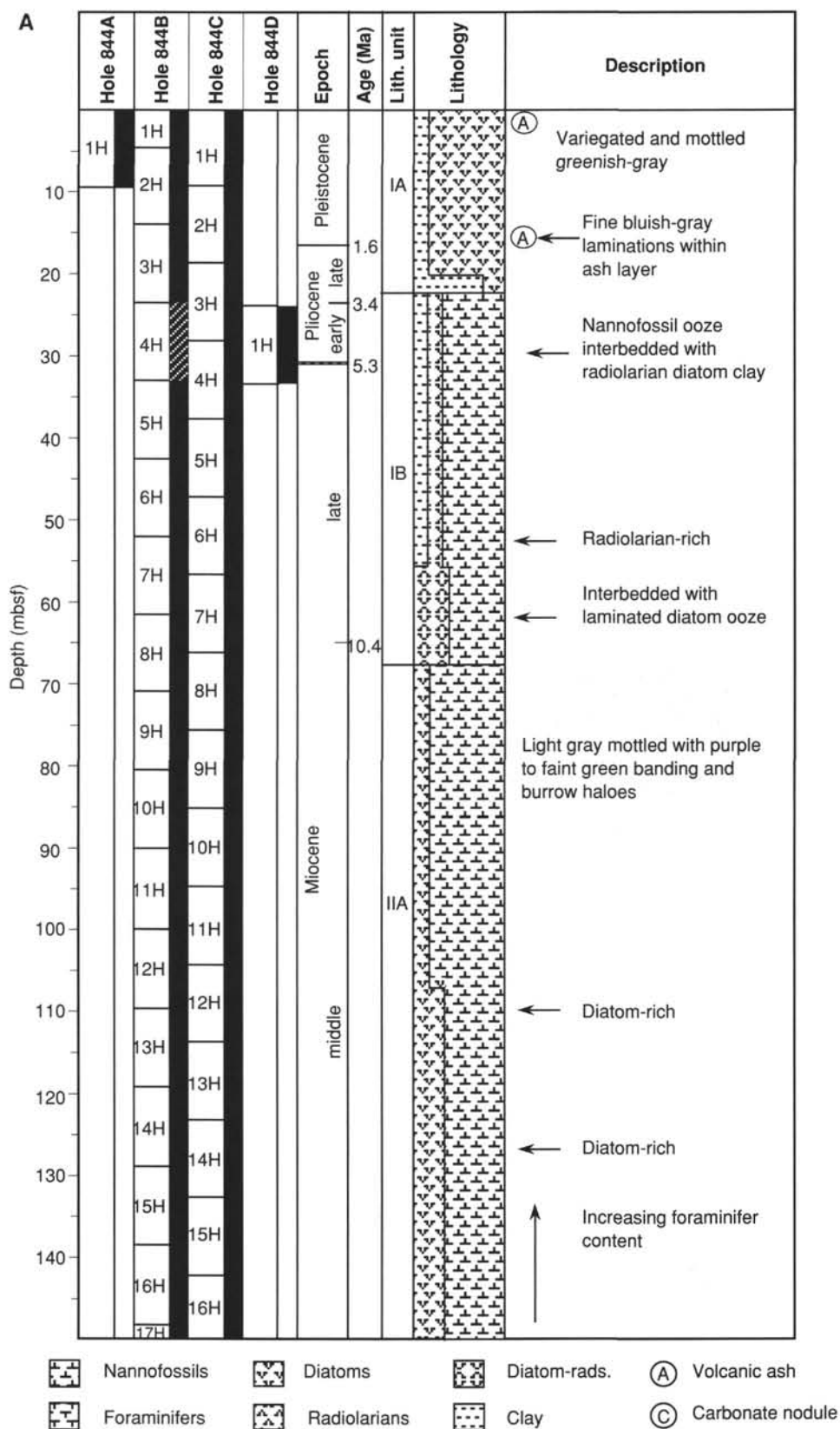
Figure 5. **A.** Site 844 lithologic summary (0–150 mbsf). **B.** Site 844 lithologic summary (150–290.8 mbsf).
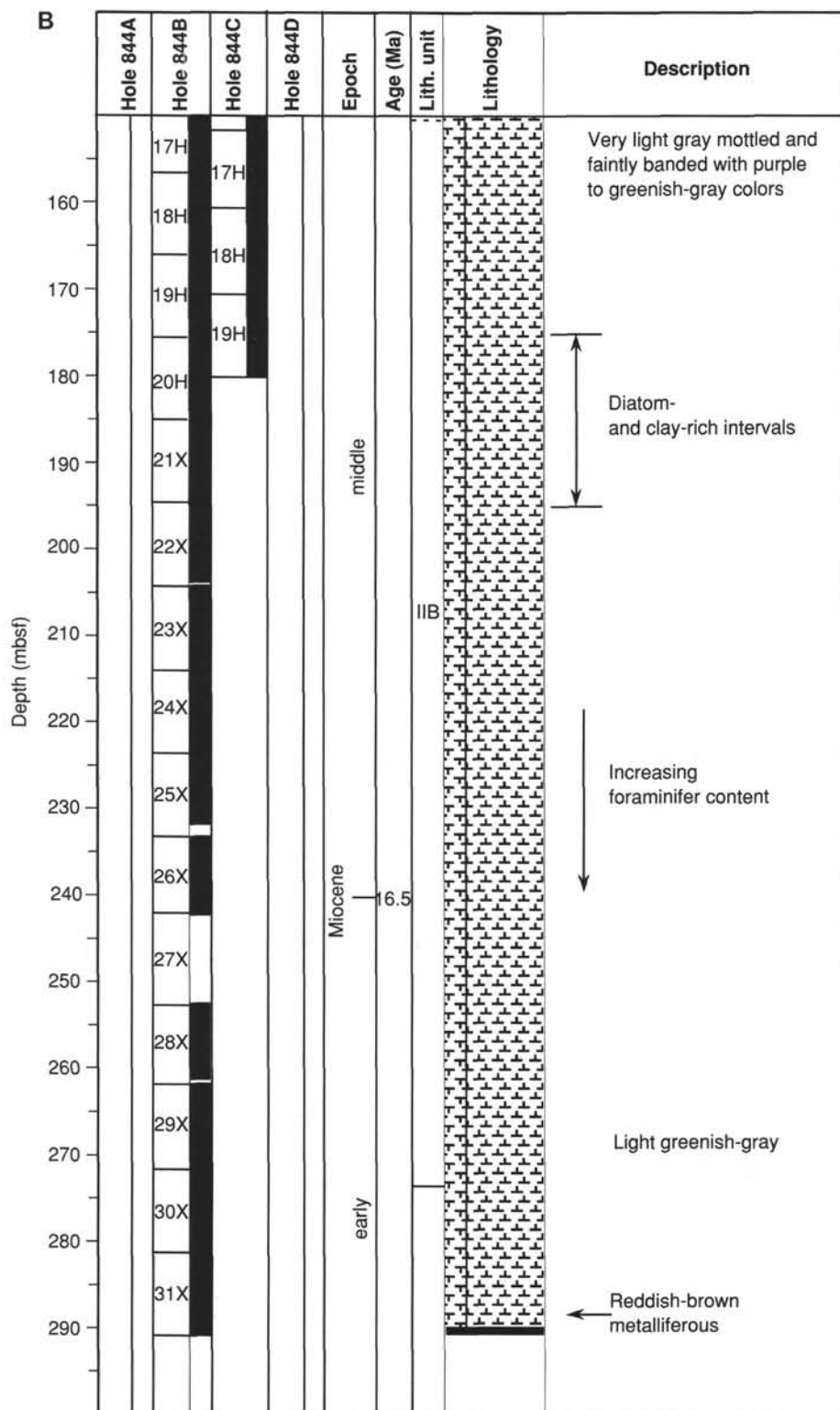
Figure 5 (continued).

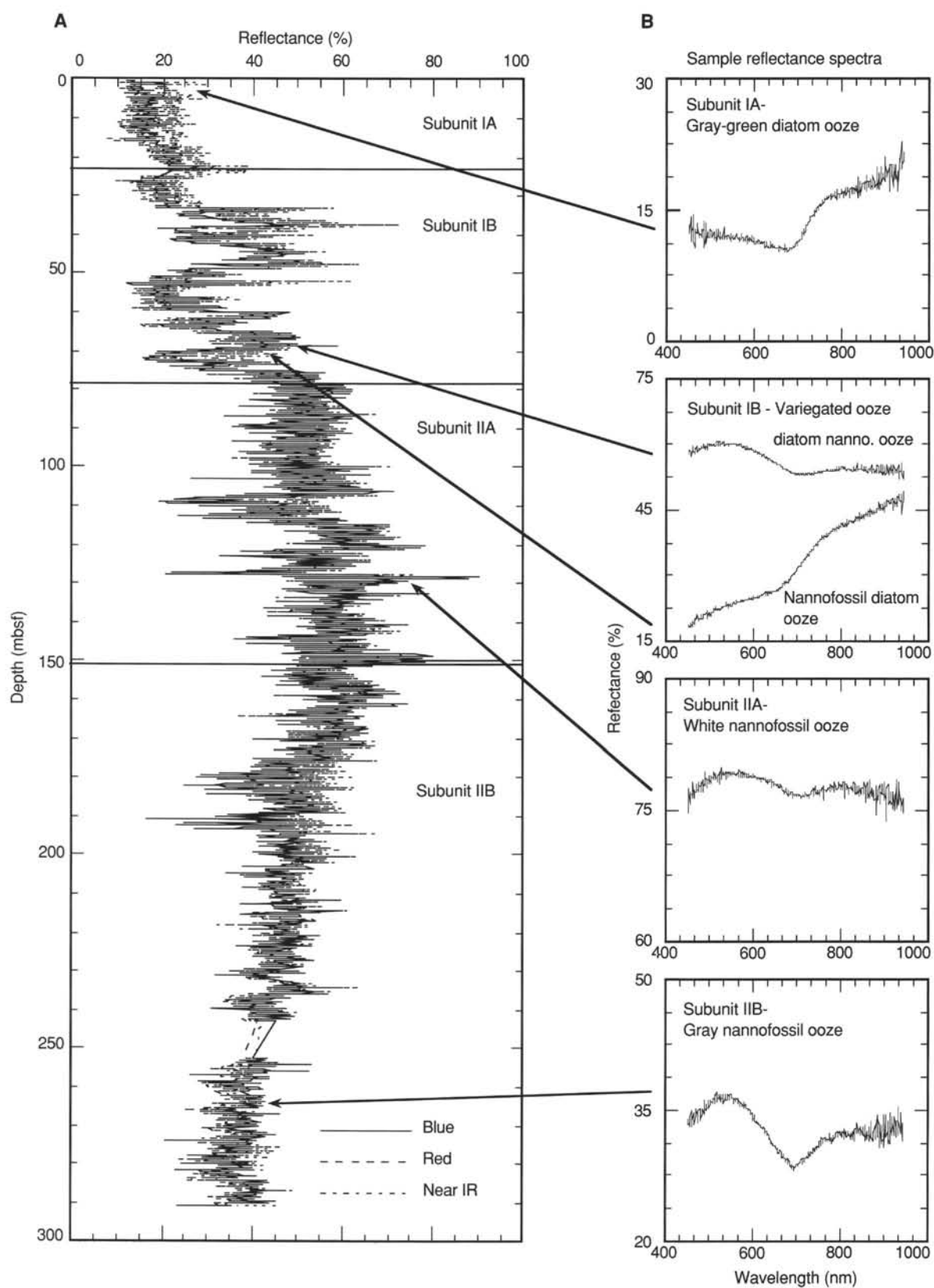**A**

Reflectance (%)

B

Sample reflectance spectra

Figure 6. **A.** Percentage of reflectance of sediments from Hole 844B. **B.** Representative color spectra of sediments from each lithology.

Early Diagenetic Lamination and Banding

Dark bluish-gray, purplish, and black lamination and banding is common throughout Site 844, except in the lowermost part of Subunit IA and the upper part of Subunit IB (16–47 mbsf), i.e., the sediments having the lowest sedimentation rates (see "Sedimentation Rates" section, this chapter). This banding and lamination was often observed to cut burrows (Fig. 14). Other features having this distinctive color are halos and rinds around burrows and burrow fill. Pyrite sometimes was identified within bands and burrow-fill zones, where these colors were intense. Some of the dark bluish lamination and banding in cores left for close-up photography was observed to fade rapidly, suggesting that these result from monosulfides, which oxidize rapidly.

The halos around burrows may be explained by the advance of local redox fronts associated with diagenesis of organic matter in the burrow fill or wall linings. Much of the dark bluish lamination is bedding-parallel, and sometimes cross-cuts burrows. This is best explained by changes in the composition and flux of accumulating sediment, especially changes in Fe and C_{org} that cause migration of redox fronts in the bulk sediment pile.

Compositional Banding

Compositional banding is not visually discernable in Subunit IA, is common in Subunit IB, and is occasionally discernable in Unit II. Comparison with sedimentation rates (see "Sedimentation Rates" section, this chapter) indicates that some of the banding is on a scale that is within the common Milankovitch frequencies. Near the top of Subunit IB (27–37 mbsf, Hole 844C), very pale brown foraminifer-nannofossil ooze is interbedded with grayish-brown siliceous ooze on a decimeter-scale. Bedding contacts among these lithologies are obscured by extensive bioturbation. This banding changes character between 37 to 47 mbsf to an alternation on a similar scale between light/medium gray to light brown nannofossil ooze and darker brown to light greenish-brown siliceous ooze. The darker siliceous oozes appear more heavily bioturbated than the lighter nannofossil oozes (Fig. 15). Below 47 mbsf (Hole 844B), nannofossil ooze is interbedded with thicker (greater than 1 m) intervals of clayey radiolarian ooze. Between 51 and 55 mbsf (Hole 844C), decimeter-scale beds of very pale brown siliceous nannofossil ooze are interbedded with dark brown (possibly Mn-oxide-rich) bands of diatom radiolarian clay.

Immediately above and below the laminated diatom ooze at the top of Unit II, between 70 and 73 mbsf (Hole 844C), a decimeter-scale interbedding is seen between the dominant pale gray nannofossil ooze and the olive-gray diatom ooze. Within the diatom ooze itself, an alternation on a similar scale was observed between lightly bioturbated and laminated intervals. This style of alternation is also present in the diatom ooze intervals in Unit II at 109 to 111 mbsf (Hole 844B) and 128 to 129 mbsf (Hole 844B). A faint color banding is seen in Subunit IIB that comprises a decimeter-scale alternation between paler and darker shades of gray, which examination of smear slides suggests is related to a variation in silica content.

Compositional Lamination

Very fine-scale lamination comprising distinct submillimeter layers of monospecific diatoms and alternations between diatom and diatom-nannofossil oozes occurs at the base of Unit I (70–73 mbsf) and in Subunit IB (109–111 and 128–129 mbsf). The total absence of bioturbation in parts of these intervals suggests that they occurred during episodes in which bottom waters were low in oxygen. Detailed interpretation of these laminated sequences must await more detailed electron microscope studies.

Early Redox Banding

The very dark brown bedding alternation in Subunit IB at the top and between 51 and 55 mbsf may be associated with the development of Fe-Mn-oxides and may represent periods of slower deposition, consistent with their siliceous clay/clay composition.

BIOSTRATIGRAPHY

Sediments recovered from the four holes cored at Site 844 provide a continuous sedimentary record for the upper Pleistocene through the upper-lower Miocene. Calcareous nannofossils, radiolarians, and diatoms are generally present throughout and provide a well-constrained stratigraphy for the recovered sequence (Tables 3, 5, and 6; Fig. 16). Planktonic foraminifers are rare or absent in the upper 75 m, but are common to abundant through the remaining cored interval (total depth, 290.9 mbsf). The following discussion focuses on results from Holes 844B and 844C because only one core each was recovered from Holes 844A (equivalent to CN14a) and 844D (equivalent to Zone CN9).

Epoch boundaries have been placed at the following depths:

Boundary	Hole	Depth (mbsf)	Depth (mcd)	Event
Pleistocene/ Pliocene	844C	16.18	18.10	Olduvai (T)
late/early Pliocene	844C	23.10	25.35	Gauss (O)
Pliocene/Miocene	844C	30.95	35.10	Gilbert (O)
late/middle Miocene	844C	65.00	72.65	B *Discoaster hamatus*
late/middle Miocene	844B	65.00	72.15	B *Discoaster hamatus*
middle/early Miocene	844B	23.92	57.63	T *Helicosphaera ampliaperta*

(T) = termination; (O) onset; B = bottom occurrence; T = top occurrence.

Calcareous Nannofossils

Calcareous nannofossils recovered at Site 844 represent a stratigraphic succession from the upper Pleistocene (Zone CN14b from Okada and Bukry, 1980, and Zone NN20 from Martini, 1971) through the lower Miocene (Zones CN3–NN4). Calcareous nannofossils generally are present, but their relative abundance and preservation vary throughout the recovered sequence. In the Pleistocene–Pliocene interval (Cores 138-844B-1H through -4H), calcareous nannofossils are rare and often exhibit severe dissolution. The presence of a few age-diagnostic species (e.g., *Pseudoemiliania lacunosa* and *Gephyrocapsa oceanica* s.l.) provide stratigraphic subdivision of the upper sequence.

Although calcareous nannofossils are generally well-preserved in the Miocene samples examined, discoasterids show moderate overgrowth in some intervals. The Miocene assemblage is characterized by discoasterids, sphenoliths, helicoliths and placoliths, mainly *Reticulofenestra* spp. and *Coccolithus* spp.

The calcareous nannofossil events recognized at Site 844 are presented in Table 3. The presence of *Gephyrocapsa oceanica* s.l. in samples examined from the upper two cores of Hole 844B allowed us to place these cores into Pleistocene Zone CN14. The occurrence of *Pseudoemiliania lacunosa* in Sample 138-844B-2H-CC indicates that Samples 138-844B-1H-CC and -2H-CC are equivalent to Subzone CN14b and CN14a, respectively.

Calcareous nannofossils generally are absent in samples assigned to the Pliocene on the basis of other biostratigraphies. Exceptions to this include Samples 138-844B-4H-CC, -844C-3H-CC, and -4H-1, 75 cm, which contain common-to-abundant and moderately well-preserved specimens. Sample 138-844B-4H-CC was assigned to
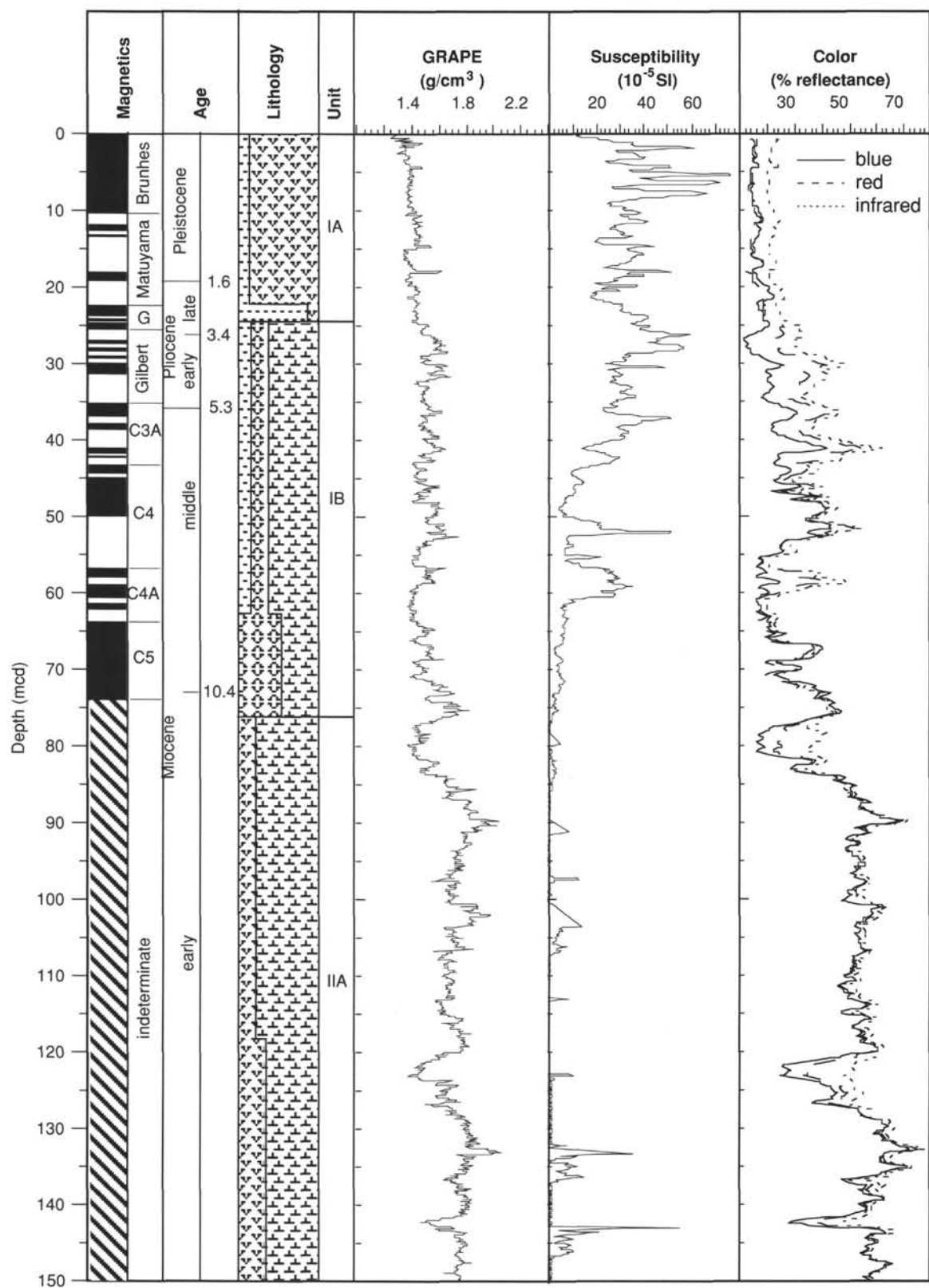
Figure 7. Composite summary of magnetics, age, graphic lithology, GRAPE, magnetic susceptibility, and color reflectance for Site 844. Composite data consist of sections spliced together from multiple holes drilled at the site. Data are shown plotted vs. composite depth (mcd), the new depth scale used when composite sections are constructed. GRAPE, susceptibility, and color data are smoothed using a 20-point Gaussian filter.
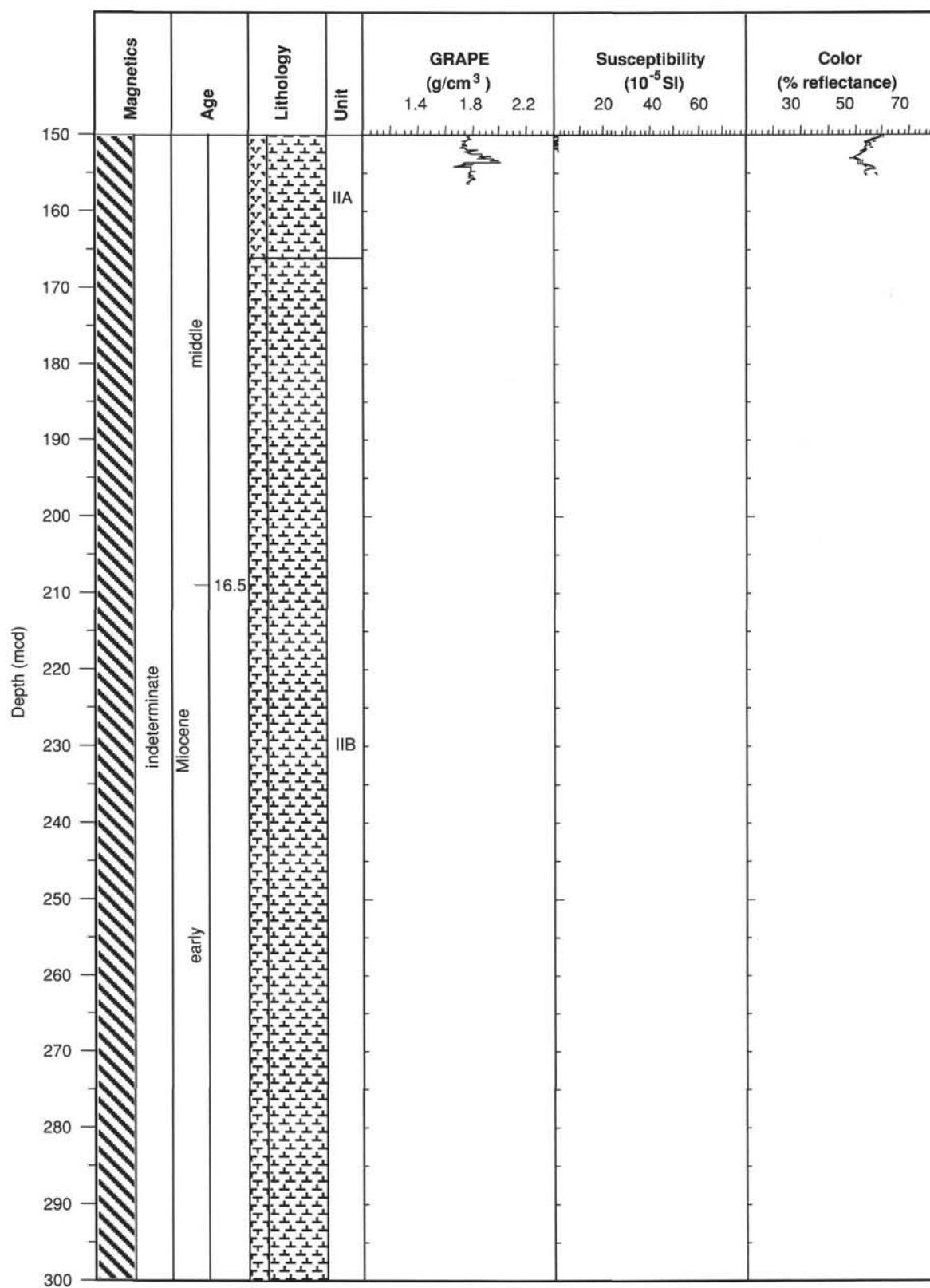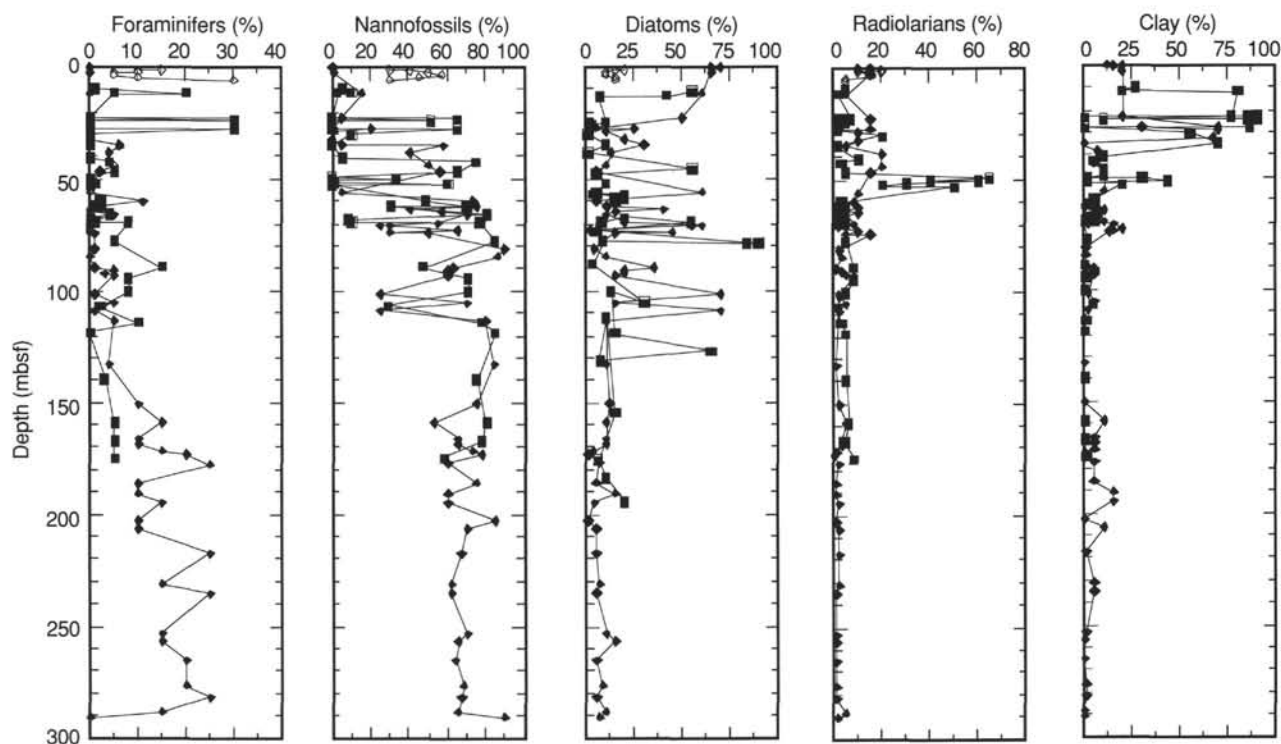
Figure 7 (continued).

SITE 844

Figure 8. Summary of smear slide data from Site 844. Open diamond = Hole 844A; solid diamond = Hole 844B; filled square = Hole 844C.

Zone CN12 on the basis of the occurrence of *Discoaster brouweri, Discoaster surculus,* and *Discoaster pentaradiatus.* Samples 138-844C-3H-CC and -4H-1, 75 cm, were placed in Zone CN10 on the basis of the occurrence of *D. brouweri, D. surculus, D. pentaradiatus, Amaurolithus delicatus,* and *Ceratolithus acutus.*

Samples 138-844B-5H-2, 60 cm, and -6H-3, 60 cm, and Samples 138-844C-4H-1, 75 cm, and -5H-6, 148 cm, are characterized by *Discoaster berggreni, D. quinqueramus,* and *Amaurolithus* spp. These samples were placed in Subzone CN9b. In addition to the above species, Sample 138-844B-5H-2, 60 cm, also contains specimens of *Amaurolithus amplificus,* suggesting that this sample approximates the middle portion of this zone.

The CN7/CN8 (NN9/NN10) boundary was defined by the last occurrence of *Discoaster hamatus* (Okada and Bukry, 1980). In Hole 844B, the first occurrence of *Minylitha convallis* approximates the last occurrence of *D. hamatus* and was used to identify this zonal boundary (following the previous suggestion of Rio et al., 1990). The co-occurrence of these two events indicates that Samples 138-844B-7H-1, 60 cm, and 138-844C-7H-6, 14 cm, approximate this zonal boundary. The presence of *D. hamatus* without *M. convallis* indicates that Samples 138-844B-8H-2, 60 cm, and -844C-7H-6, 143 cm, are equivalent to Zone CN7.

The middle Miocene is represented by Zones CN6 through the uppermost portion of CN3. The first occurrence of *Catinaster coalitus,* definition of the CN6/CN5 (NN8/NN9) zonal boundary, was placed in Samples 138-844B-8H-5, 60 cm, and -844C-7H-CC. The last occurrence of *Coccolithus miopelagicus* occurs within this interval in Samples 138-844B-8H-2, 60 cm, and -844C-7H-CC.

The CN5a/CN4 (NN6/NN5) zonal boundary is defined by the last occurrence of *Sphenolithus heteromorphus.* This event occurs in Samples 138-844B-9H-7, 65 cm, and -844C-18H-CC. The first occurrence of *Discoaster kugleri,* which marks the Subzone CN5b/CN5a (NN7/NN6) boundary, was observed in Samples 138-844B-13H-5, 60 cm, and -844C-16H-CC. Other events observed in this interval include the first occurrence of *Reticulofenestra pseudoumbilicus* (Sample 138-844B-19H-6, 65 cm); the last occurrence of *Coronocyclus nitescens*

(Sample 138-844B-13H-4, 60 cm); and the first occurrence of *Triquetrorhabdulus rugosus* (Sample 138-844B-14H-1, 60 cm). The CN4/CN3 (NN5/NN4) zonal boundary was marked by the last occurrence of *Helicosphaera ampliaperta,* recorded in Samples 138-844B-26X-5, 90 cm. The lowermost portion of Hole 844B (Cores 138-844B-26X through -31X) was assigned to the lower Miocene Zone CN3 (NN4) on the basis of the presence of *Helicosphaera ampliaperta.*

Planktonic Foraminifers

Planktonic foraminifers are rare to absent in the Pleistocene through upper Miocene sequence from Cores 138-844B-1H-CC through -8H-CC. When present, their preservation is poor (core-catcher Samples 138-844B-1H-CC, -2H-CC, -4H-CC, and -6H-CC). Samples 138-844B-3H-CC and -6H-CC through -8H-CC are barren of foraminifers. In this entire upper Neogene interval, the coarse fraction residues are dominated by abundant radiolarians and volcanic ash. Less common components include sponge spicules and fish teeth. Glauconite pellets occur in Sample 138-844B-4H-CC.

The middle to lower Miocene sequence (Table 4) from Cores 138-844B-9H through -30X yielded common-to-abundant planktonic foraminifers that are moderately well- to poorly preserved. Preservation varies from sample to sample, with intervals of alternating preservation observed. Intervals having moderately well-preserved foraminiferal faunas include Samples 138-844B-9H-CC through -11H-CC, -13H-CC, and -15H-CC through -18H-CC, whereas those having poorly preserved foraminifers include Samples 138-844B-12H-CC, -14H-CC, and -19H-CC through -30X-CC. Coarse fraction residues are dominated by foraminifers and radiolarians, with the latter being largely dominant in the intervals of poorly preserved foraminifers. Other less common coarse-fraction components include diatoms, sponge spicules, fish teeth, and echinoid spines. Volcanic ash was noted in Samples 138-844B-15H-CC through -17H-CC.

The assemblages in the interval from Samples 138-844B-1H-CC through -2H-CC are dominated by the solution-resistant spe-
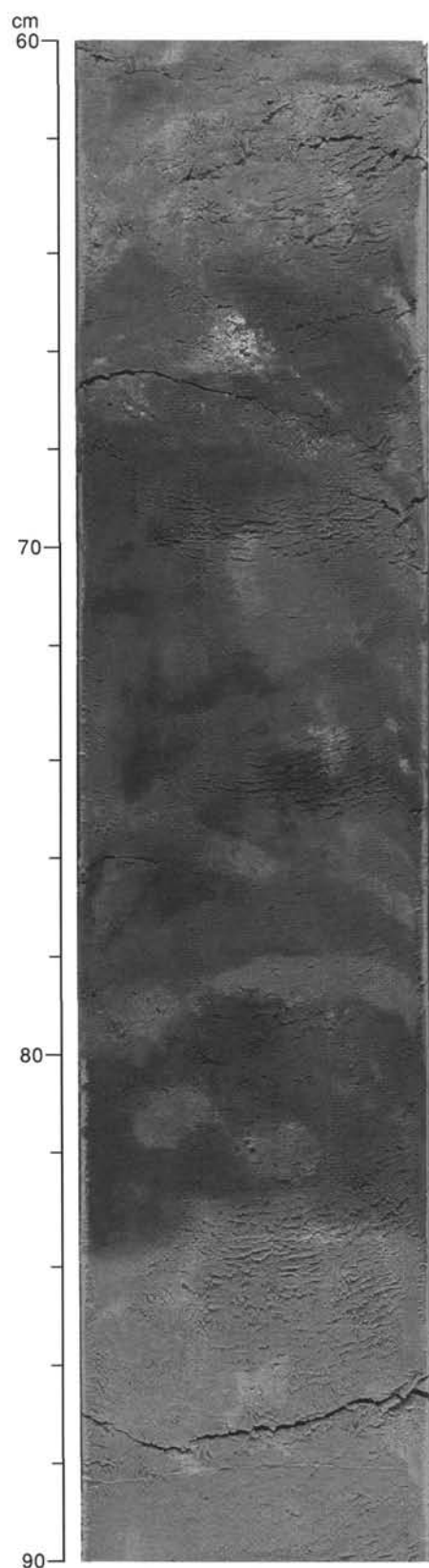
Figure 9. Distinctive bed of very dark grayish-brown, burrowed radiolarian ooze that occurs in the middle of a radiolarian-rich interval (47–56 mbsf, Hole 844C) in lithologic Subunit IB (interval at 138-844B-7H-1, 60–90 cm).
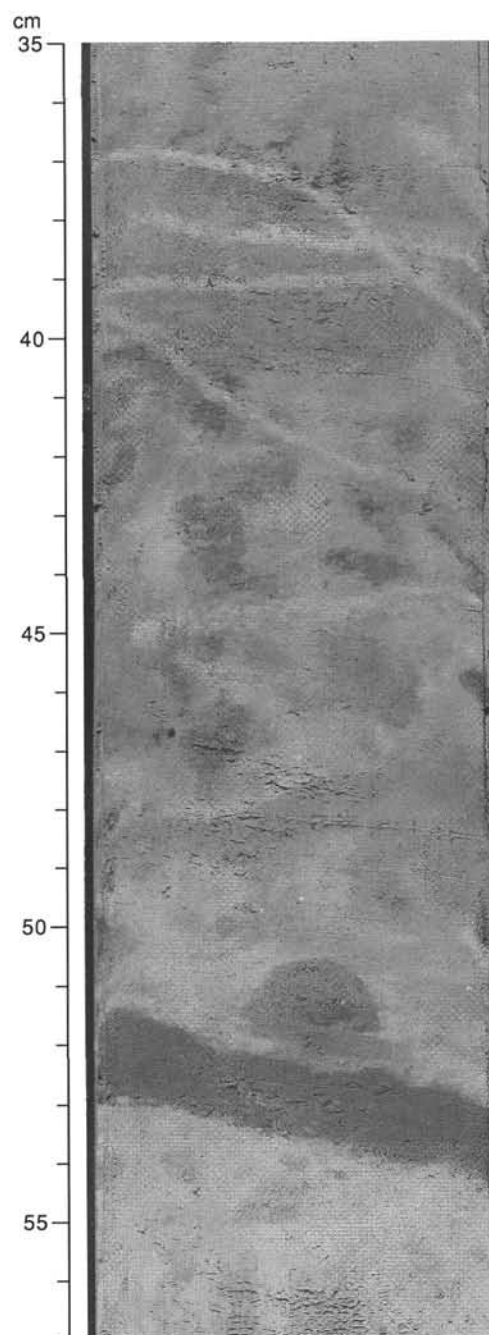

Figure 10. Common *Zoophycos* burrows between 41 and 55 mbsf (interval at 138-844B-5H-3, 35–57 cm).

cies, *Globorotalia menardii*, *G. tumida*, and *Neogloboquadrina dutertrei*. The species *Globigerinoides sacculifer*, *G. ruber*, and *Pulleniatina obliquiloculata* are rare. *Pulleniatina obliquiloculata* assemblages are right-coiling in Sample 138-844B-1H-CC and left-coiling in Sample 138-844B-2H-CC. This interval, dated as Pleistocene in age from other microfossil data, was assigned to Zone N22, although the nominate taxon for this zone is not present. Sample 138-844B-3H-CC is barren of planktonic foraminifers. The interval from Sample 138-844B-4H-CC through Section 138-844B-6H-4 is older than 3 Ma, as indicated by the presence of *Globorotalia limbata*, *Sphaeroidinellopsis* spp. and *Dentoglobig-*
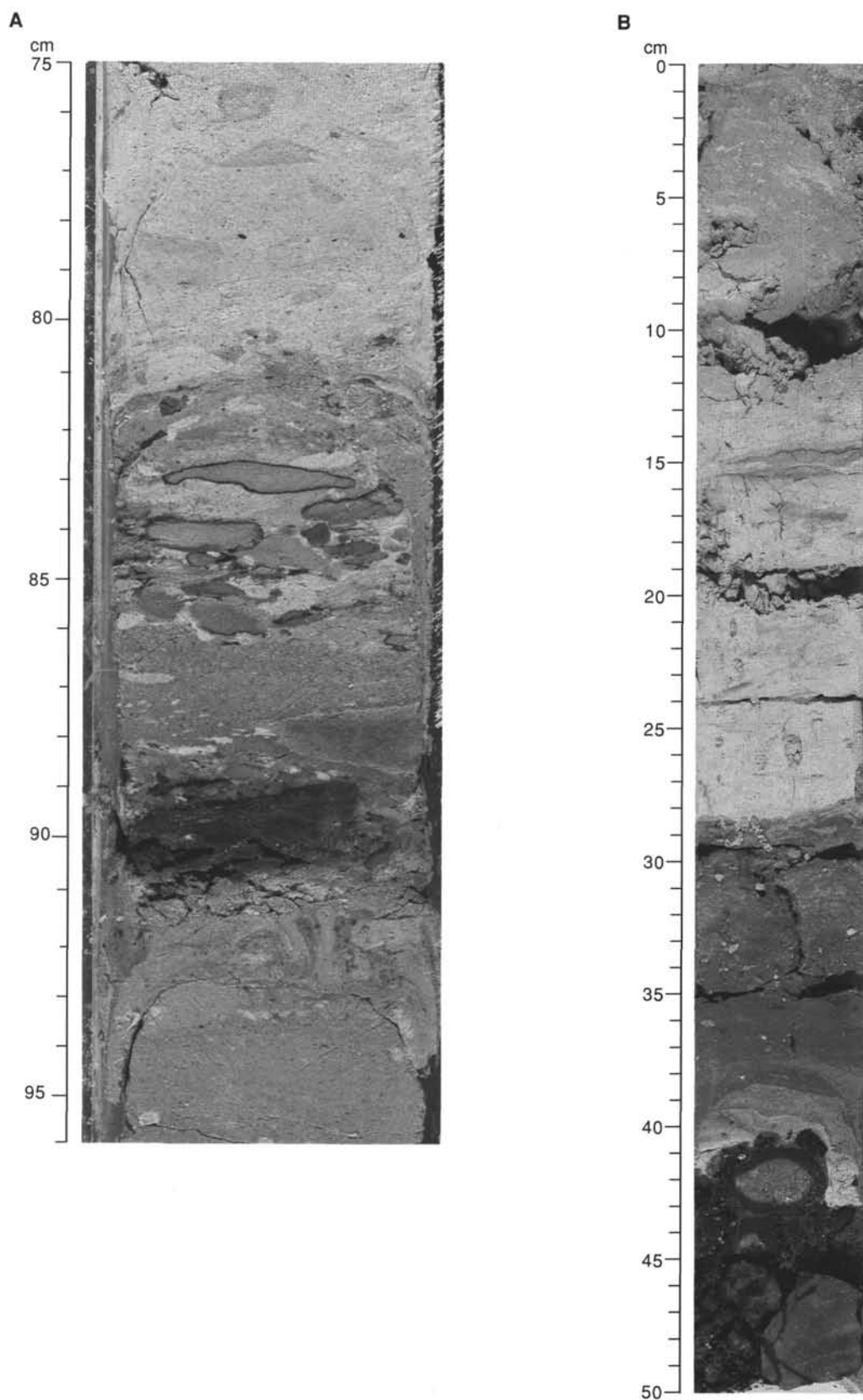
A

B

Figure 11. **A.** Conglomeratic horizon in the sequence of nannofossil ooze immediately above basement in Subunit IIB (interval at 138-844B-30X-2, 75–96 cm). **B.** Contact between lithologic Unit II and basement, showing interbedding of nannofossil age and metalliferous sediment (138-844B-31X-CC).
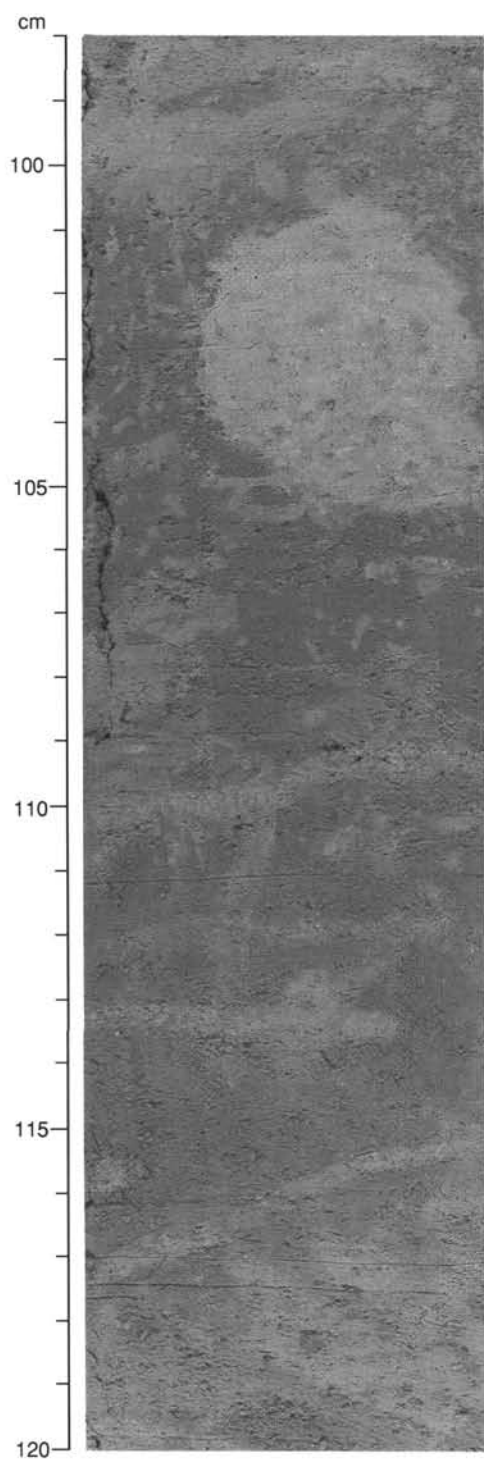
Figure 12. *Chondrites* cutting a large solid burrow with three *Zoophycos* burrows cutting an indistinct vertical burrow. The darker material is radiolarian diatom ooze; the paler material is nannofossil ooze. Interval is near the top of Subunit IB at 138-844C-3H-6, 98–120 cm.
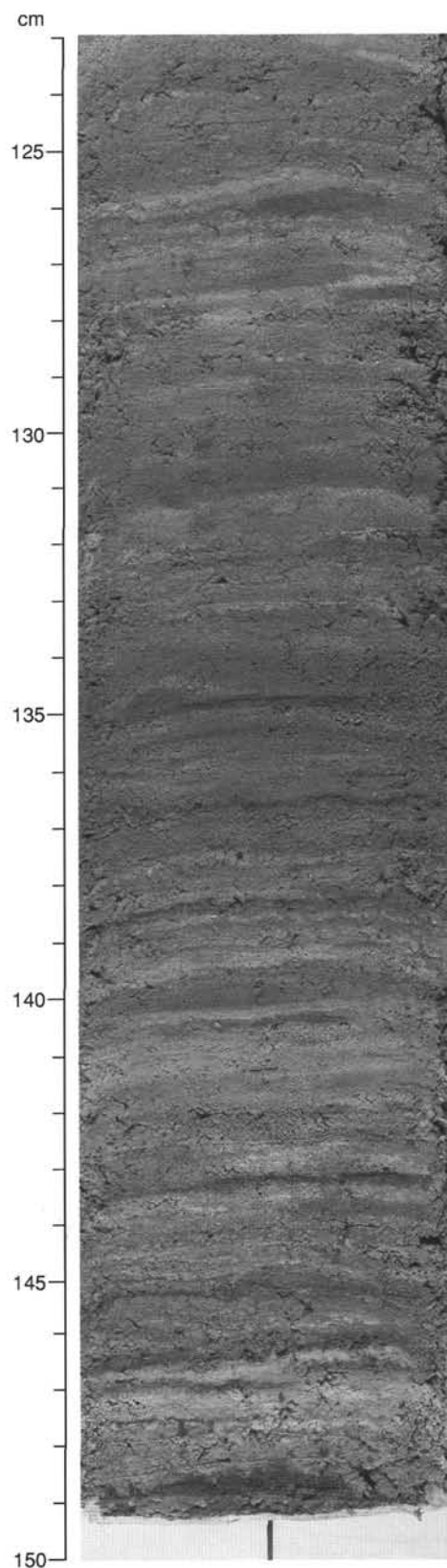

Figure 13. Finely laminated, unbioturbated diatom ooze in Unit II (138-844C-8H-3, 123–150 cm).
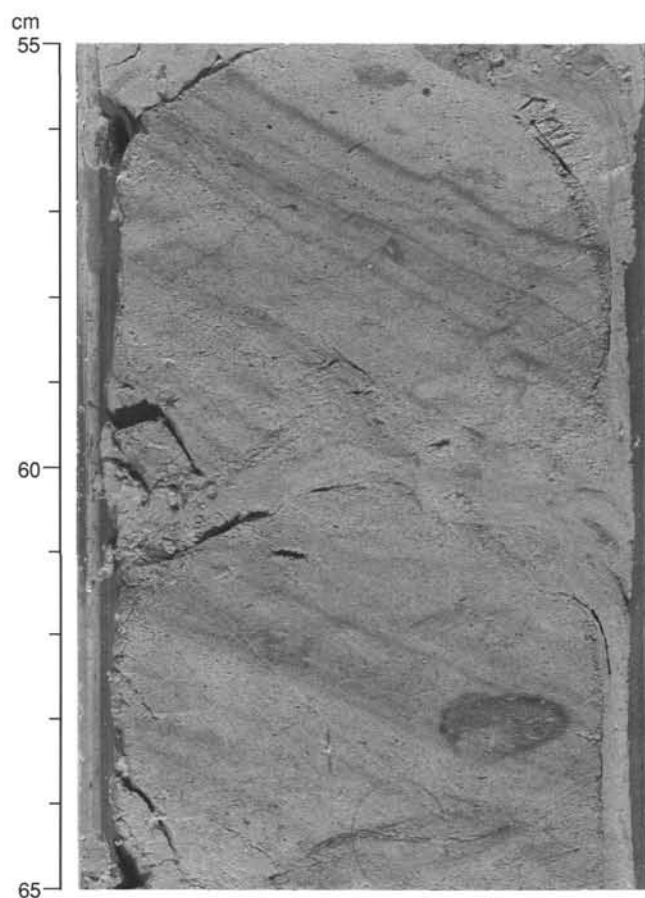
Figure 14. Fine, dark-bluish, early diagenetic color lamination cutting a *Planolites* burrow in Unit II (138-844B-30X-3, 55–65 cm).

erinaaltispira. Sample 138-844B-4H-CC, which contains *G. tumida,* is younger than 5 Ma. Sample 138-844B-4H-CC was assigned to the undifferentiated Pliocene zonal interval N19-N18, whereas the interval from Sample 138-844B-5H-CC through Section 138-844B-6H-4, which contains *Neogloboquadrina humerosa* without *G. tumida,* has been attributed to upper Miocene Zone N17.

Assemblages of the middle to lower Miocene fauna are dominated by *D. altispira, Globoquadrina venezuelana, Globorotalia mayeri,* and *Globigerinoides* spp. (*G. sacculifer, G. obliquus,* and *G. subquadratus*). In intervals having pronounced dissolution, the resistant species *G. venezuelana, G. mayeri,* and *Sphaeroidinellopsis* spp. become dominant. The interval from Sample 138-844B-9H-CC through -10H-CC was assigned to Zone N13 on the basis of the first occurrence of *Sphaeroidinellopsis subdehiscens* in Sample 138-844B-10H-CC. The absence of *Globigerina nepentes* in those samples supports this zonal assignment. The interval from Samples 138-844B-11H-CC through -14H-CC was assigned to Zone N12 on the basis of the co-occurrence of *Globorotalia fohsi lobata* and *G. praemenardii.* The interval between Samples 138-844B-15H-CC through -18H-CC below the first occurrence of *G. fohsi lobata* was assigned to undifferentiated Zone N12-N11. Members of the *G. fohsi* lineage are too rare to identify the first occurrence of *G. fohsi fohsi* confidently from its ancestor, *G. praefohsi.* *Globorotalia peripheroacuta* was not observed in the samples examined. As such, Zone N10 was not identified. The interval from Sample 138-844B-19H-CC through -20H-CC was assigned to Zone N9 on the basis of the co-occurrence of *Praeorbulina glomerosa circularis* and
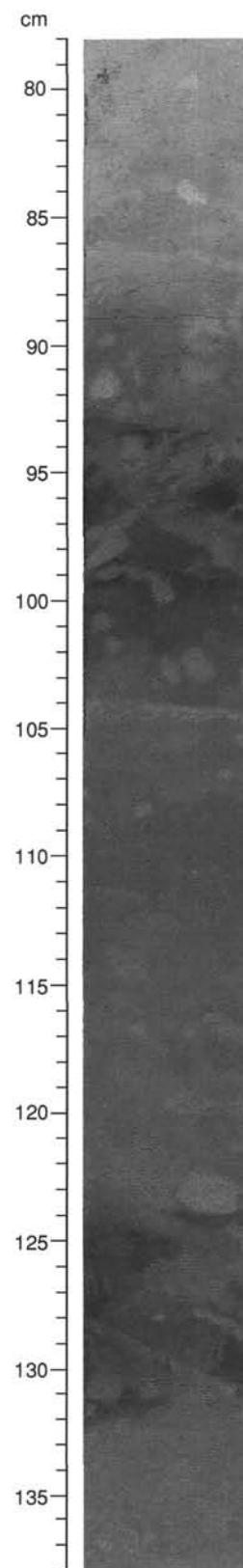

Figure 15. Heavily burrowed dark radiolarian diatom ooze interbedded with pale, less bioturbated nannofossil ooze in Subunit IB (138-844B-6H-3, 78–138 cm).

Orbulinay suturalis. The interval from Sample 138-844B-21H-CC through -28H-CC was assigned to Zone N8, between the first occurrence of *Orbulina suturalis* in Sample 138-844B-20H-CC and the first occurrence of *Praeorbulina sicana* in Sample 138-844B-28H-CC. Samples 138-844B-29H-CC and -30H-CC were assigned to Zone N7 on the basis of the absence of *Catapsydrax dissimilis,* whose last occurrence marks the base of this zone.

Radiolarians

Radiolarians sampled at Site 844 range in age from the Quaternary (*Collosphaera tuberosa* Zone) to the latest part of the early Miocene (*Calocycletta costata* Zone). The most recent radiolarian zone (*Buccinosphaera invaginata*) was not identified in any of the holes, although it may be present in the unsampled, uppermost part of the section. In general, radiolarians are well preserved and abundant in the samples studied. However, a more thorough study of the fauna was hindered by several factors. First, in the Pleistocene–Pliocene part of the section, the accumulation rate is low; thus, with the rather broad sampling scheme used (two samples per core plus core catchers), not all of the zonal boundaries and datum events could be located precisely. Second, in the lower Pliocene–uppermost Miocene section, the samples contain abundant reworked radiolarians from its older part (upper and middle Miocene). This reworking was accompanied by a decrease in preservation and served to make zonal identifications more difficult. Third, many samples contain abundant diatoms. Although a boon to diatom stratigraphers, these floods of diatoms in the acid-treated samples often made both sample preparation and identification of radiolarian species more difficult. Finally, preservation was not uniformly good. In addition to the moderate preservation in the lower Pliocene and uppermost Miocene sequence, preservation in the upper part of the *Diartus pettersoni* Zone and in the lower part of the *Calocycletta costata* Zone was only moderate. In spite of these difficulties, the recovered section appears to be nearly complete and offers an excellent opportunity to integrate the radiolarian stratigraphy (Table 5) more closely with other biostratigraphies and with magnetostratigraphy. Aside from the uppermost zone, the only other radiolarian zone not encountered in the sampling performed on material from this site was the *Phormostichoartus fistula* Zone of the Pliocene. Its absence may represent a real break in the section, or it may result from the broadly spaced samples taken from a part of the section having relatively low accumulation rates.

Of the many species often identified in studies of radiolarians from tropical regions, a few do not seem to appear at this site. It may be that the very rare occurrence of *Collosphaera tuberosa* and our failure to locate a specimen of *Buccinosphaera invaginata* may have resulted from these species not appearing in this region of relatively high productivity. In addition, we did not find *Spongaster pentas* in any of the samples and found *Spongaster berminghami* only rarely. However, *Spongaster tetras,* appeared to be present consistently. *Lamprocyclas neoheteroporous, as well as L. heteroporous* and *Pterocanium prismatium,* appear intermittently, and the locations of their first and last appearance datums may not be reliable. Tropical species, such as *Dorcadospyris alata* and *D. dentata,* never dominate parts of the assemblage and were even more rare than usual in the samples studied. All of these rather slight differences noted in the assemblages of this site might be attributed to the highly productive character of waters in the eastern tropical Pacific Ocean.

Diatoms

Diatoms recovered from Site 844 represent a continuous stratigraphic interval from the Holocene *Pseudoeunotia doliolus* Zone through Subzone B of the lower Miocene *Crucidenticula nicobarica* Zone of Barron (1985). Diatom abundance and preservation varies from sample to sample, but diatoms generally are common to abundant and well preserved in the samples examined.

The diatom assemblage is dominated by specimens of *Thalassiothrix longissima* and *Thalassionema nitzschioides,* both of which are typical in regions of high surface-water productivity. In addition, the flora is characterized by species indicative of a tropical environment. The upper Miocene to Holocene assemblage is characterized by *Azpeitia nodulifer, Hemidiscus cuneformis, Nitzschia cylindrica, Nitzschia marina, Nitzschia reinholdii, Pseudoeunotia doliolus, Thalassiosira convexa, Thalassiosira oestrupii,* and *Thalassiosira yabei.* The lower and middle Miocene diatom assemblage is characterized by *Actinocyclus ingens, Cestodiscus pulchellus, Craspedodiscus coscinodiscus, Crucidenticula nicobarica, Denticulopsis hustedtii,* and *Rossiella paleacea.*

The diatom flora present provide more than 45 stratigraphic events for the 290.9 m recovered from this site (Table 6). The majority of these events were stratigraphically constrained by data from Hole 844B. Cores 138-844A-1H and -844B-1H correspond to the Quaternary *Pseudoeunotia doliolus* Zone on the basis of the occurrence of *P. doliolus* without *N. reinholdii.* The interval representing the *P. doliolus* Zone was not observed in Hole 844C.

Samples 138-844B-2H-CC and -3H-2, 60 cm, and Sample 138-844C-1H-CC were assigned to the Quaternary *N. reinholdii* Zone on the basis of the co-occurrence of *N. reinholdii* and *P. doliolus.* Diatoms generally are well preserved and common throughout this interval.

Samples were assigned to the *Rhizosolenia praebergonii, Nitzschia jouseae,* and *Thalassiosira convexa* zones on the basis of the marker taxa. Samples 138-844B-3H-3, 82 cm, through -4H-CC and 138-844C-2H-CC were assigned to the *Rhizosolenia praebergonii* Zone. This zonal assignment was based on the occurrence of *R. praebergonii* stratigraphically below the first occurrence of *P. doliolus.* The occurrence of *R. praebergonii* in Sample 138-844C-2H-CC without *P. doliolus,* or *Thalassiosira convexa* allowed us to assign this sample to Subzone C of the *R. praebergonii* Zone. Sample 138-844B-3H-CC was barren of diatoms.

Nitzschia jouseae was observed in Sample 138-844B-4H-CC. The occurrence of this species with *Thalassiosira convexa* and without *R. praebergonii* suggests that this sample is equivalent to the *N. jouseae* Zone as defined by Barron (1985). *Nitzschia jouseae* was not observed in samples examined from Hole 844C.

The *Thalassiosira convexa* Zone, defined as the interval from the first occurrence of *T. convexa* to the last occurrence of *N. jouseae,* is represented by the diatom assemblage in Section 138-844B-5H-1 and Sample 138-844C-3H-CC. Although this zone spans a 1.6-m.y. interval, the low sedimentation rates at this site (see "Sedimentation Rates" section, this chapter) results in a short stratigraphic interval representing this zone. The occurrence of *Thalassiosira praeconvexa, Nitzschia miocenica,* and *Nitzschia miocenica* var. *elongata* in Sample 138-844B-5H-1, 120–121 cm, indicates that this sample is equivalent to Subzone A of this zone. The first occurrence of *T. convexa* occurs between Samples 138-844B-5H-1, 120–121 cm, and -5H-2, 120–121 cm (Table 6).

Samples 138-844B-2H, 120–122 cm, -5H-3, 120–121 cm, and 844C-4H-CC were placed in the *Nitzschia miocenica* Zone on the basis of the occurrence of *Nitzschia miocenica.* The occurrence of *Thalassiosira preaconvexa* in Sample 138-844B-5H-2, 120–121 cm, suggests that this sample represents the uppermost portion of this zone and is equivalent to Subzone B. The absence of this species in Samples 138-844B-5H-3, 120–121 cm, and -844C-4H-CC suggests placement of this sample in Subzone A of the *N. miocenica* Zone. Diatoms are well preserved and common to abundant in this interval.

The interval from the last occurrence of *Thalassiosira yabei* (Sample 138-844B-6H-1, 120–121 cm) to the first occurrence of *N. miocenica* (Sample 138-844B-5H-5, 114–116 cm) defines the *Nitzschia porteri* Zone. The first occurrence of *Nitzschia cylindrica* in Sample 138-844B-5H-CC approximates the last occurrence of *T. yabei* and supports the stratigraphic placement of the *T. yabei/N. porteri* zonal boundary. Beginning with the interval equivalent to the *N. porteri* Zone and continuing stratigraphically lower, specimens of *Thalassiothrix longissima* become common to abundant in numerous samples examined. In
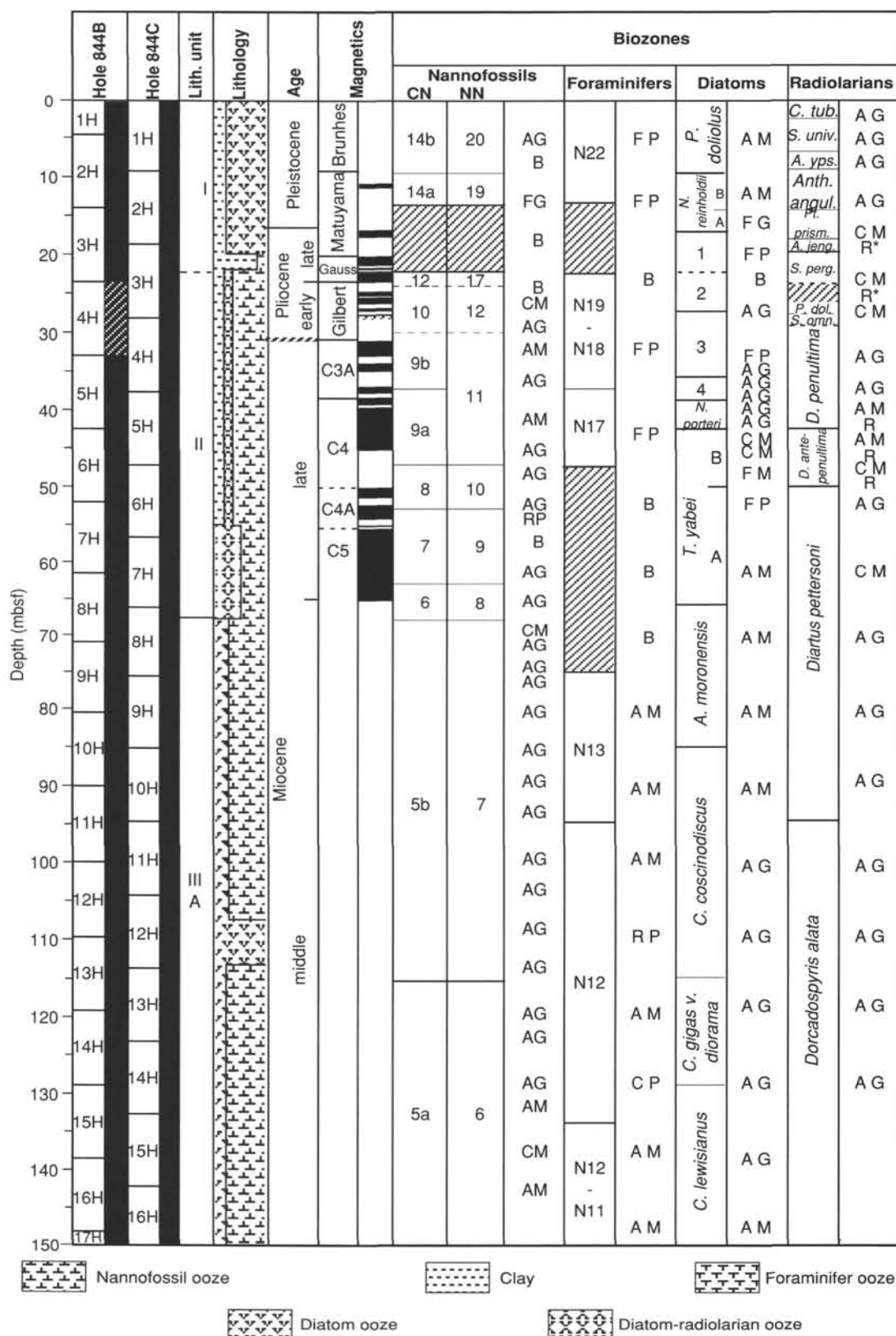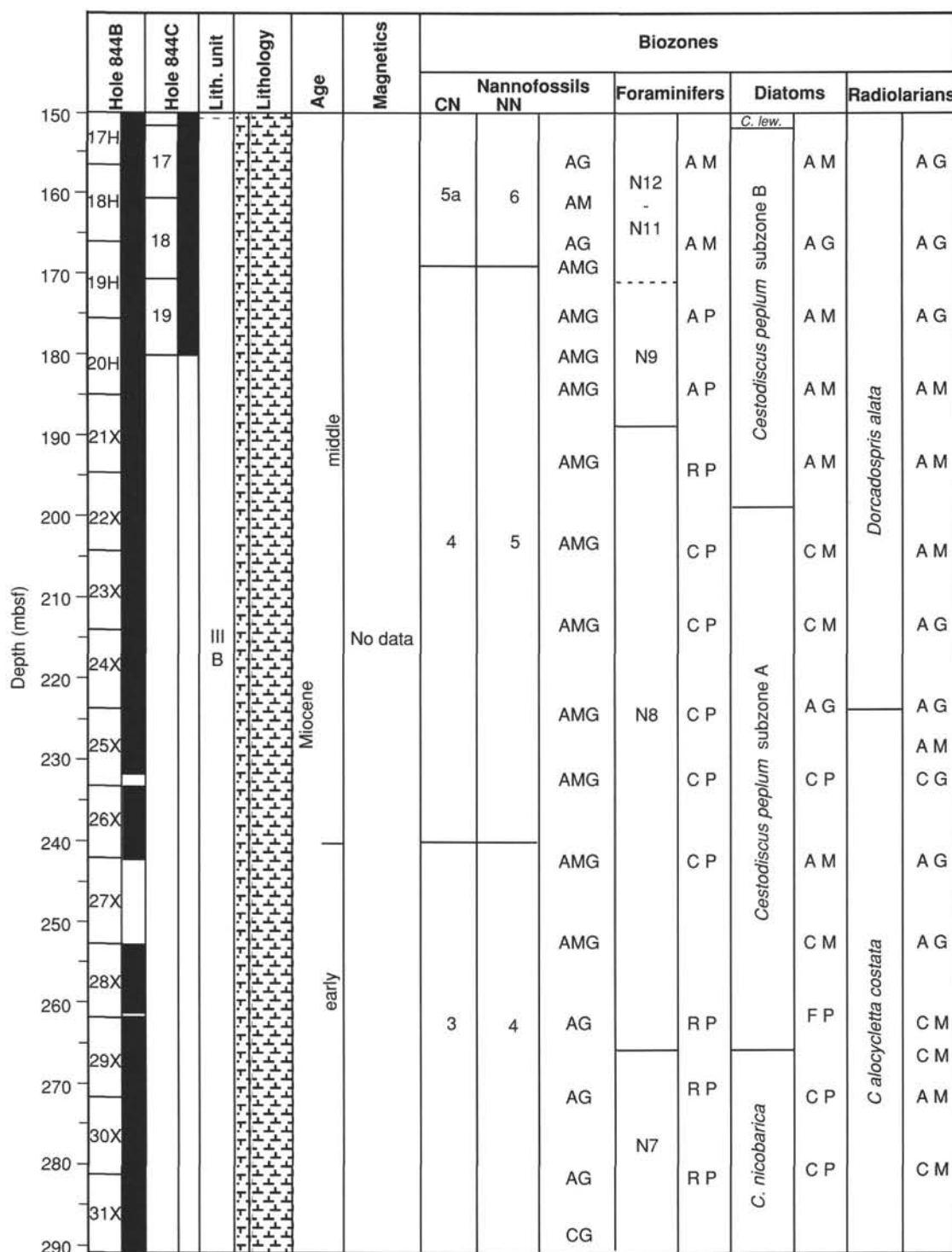
Figure 16.

Figure 16 (continued). Stratigraphic summary for Site 844. Depth is in meters below seafloor (mbsf). Hatched area in Core 138-844B-4H represents a drilling-induced disturbed stratigraphic sequence. Other hatched areas represent intervals where specimens of a particular microfossil group are rare or absent, which prevented zonal assignment. Dashed lines represent uncertainty in placement of a zonal boundary. Diatoms zones: 1 = *Rhozosolenia praebersonii*, 2 = *Nitzschia jouseae*, 3 = *Thalassiosira convexa*, 4 = *Nitzschia miocenica*. Microfossil abundance is recorded as A = abundant; C = common; F = few; R = B = barren. Microfossil preservation is recorded as G = good; M = moderate; P = poor. This figure presents a general overview of the stratigraphic results at Site 844. Placement of specific stratigraphic boundaries may differ slightly between Holes 844A and 844B. Data presented in this figure are based on results from Holes 844C (0-60 mbsf) and 844B (60-290.90 mbsf).

Table 3. Interval (core and section) and depth (mbsf and mcd) constraints of calcareous nannofossil events for Site 844.

Event	Hole 844B			Hole 844C		
	Interval (cm)	Depth (mbsf)	Depth (mcd)	Interval (cm)	Depth (mbsf)	Depth (mcd)
T *Discoaster quinqueramus*				4H-1, 75–4H-2, 97	28.85–30.57	33.00–34.72
T *Amaurolithus amplificus*				4H-3, 78–4H-3, 148	31.88–32.58	36.03–36.73
B *Amaurolithus amplificus*	5H-2, 60–5H-3, 60	35.10–36.60	38.75–40.25			
B *Amaurolithus primus*	5H-3, 60–5H-4, 60	36.60–38.10	40.25–41.75	4H-CC–5H-1, 75	38.18–38.35	42.33–43.60
B *Discoaster berggreni*	6H-3, 60–6H-4, 60	46.10–47.60	50.20–51.70	5H-6, 148–5H-7, 10	46.58–46.70	51.83–51.95
B *Minylita convallis*	6H-CC–7H-1, 60	52.52–52.60	52.62–59.30			
T *Discoaster hamatus*	7H-1, 60–7H-1, 140	52.60–53.40	59.30–60.10			
B *Discoaster hamatus*	8H-1, 60–8H-2, 60	62.10–63.60	69.25–70.75	7H-4, 47–7H-6, 143	60.57–64.53	68.22–72.18
T *Coccolithus miopelagicus*	8H-1, 60–8H-2, 60	62.10–63.60	69.25–70.75	7H-6, 143–7H-CC	64.53–66.73	72.18–74.38
B *Catinaster coalitus*	8H-5, 60–8H-6, 60	68.10–69.60	75.25–76.75	7H-CC–8H-CC	66.73–76.30	74.38–85.61
T *Coronocyclus nitescens*	13H-3, 60–13H-4, 60	112.60–114.10	126.40–127.90			
B *Discoaster kugleri*	13H-4, 60–13H-5, 60	114.10–115.60	127.90–129.40	15H-CC–16H-CC	142.80–152.16	157.70–167.66
B *Triquetrorhabdulus rugosus*	14H-1, 60–14H-2, 60	119.10–120.60	133.93–135.43			
T *Cyclicargolithus floridanus*	17H-6, 50–17H-7, 60	155.10–156.60	170.60–172.20			
T *Sphenolithus heteromorphus*	19H-4, 65–19H-5, 65	171.15–172.65	188.35–189.85	17H-CC–18H-CC	161.50–171.19	178.50–188.14
B *Reticulofenestra pseudoumbilicus*	19H-6, 65–19H-7, 55	174.15–175.55	191.35–192.85			
T *Helicosphaera ampliaperta*	26X-4, 90–26X-5, 90	238.70–240.20	257.33–258.83			

T = top occurrence; B = bottom occurrence.

several samples, specimens of this species are so abundant that they mask the rest of the diatom assemblage.

Samples examined from 138-844B-6H-2, 120–121 cm, through -8H-1, 60 cm, and -844C-6H-CC were assigned to the *T. yabei* Zone on the basis of the last occurrence of *Actinocyclus moronensis* in Samples 138-844B-8H-CC and -844C-7H-CC. The *A. moronensis* Zone is represented by Samples 138-844B-8H-CC and -9H-CC and Samples 138-844C-7H-CC and -8H-CC. This interval is characterized by few-to-common specimens of *Denticulopsis hustedtii*, and few specimens of *T. yabei* and *R. paleacea*.

The *Craspedodiscus coscinodiscus* Zone is defined as the interval from the first *Thalassiosira temperi* var. *delicata* to the last *Craspedodiscus coscinodiscus*. Unfortunately, *Thalassiosira temperi* var. *delicata* is rare in the few samples examined, making placement of the *C. coscinodiscus/C. gigas* var. *diorama* zonal boundary tentative. Additional markers used to constrain this boundary include (1) the last occurrence of *Cestodiscus pulchellus*, which is consistently present throughout this interval and has a last occurrence that approximates the last occurrence of *T. temperi* var. *delicata*; (2) the last occurrence of *Crucidenticula nicobarica*; and (3) the first occurrence of *Nitzschia porteri*. Samples assigned to the *C. coscinodiscus* Zone include Samples 138-844B-10H-CC, -12H-CC, -844C-11H, and -12H-CC. Samples assigned to the *C. gigas* var. *diorama* Zone include Samples 138-844B-13H-CC and -14H-CC and -844C-13H-CC and -14H-CC.

The last occurrence of *Coscinodiscus lewisianus* marks the top of the *C. lewisianus* Zone. This event occurs in Samples 138-844B-15H-CC and -844C-15H-CC. The *C. lewisianus* Zone extends from the base of Cores 138-844B-15H and -844C-15H through

Cores 138-844B-17H and -844C-17H. The base of the *C. lewisianus* Zone is defined by the last occurrence of *Cestodiscus peplum*. The last occurrence of this species was placed in Sample 138-844B-18H-CC. The base of the *C. peplum* Zone was placed at the first occurrence of *C. peplum*, which was observed in Sample 138-844B-28H-CC and which allowed us to place the interval from Sample 138-844B-18H-CC through -844B-28H-CC in the *C. peplum* Zone. The occurrence of *Annellus californicus* in Samples 138-844B-22X-CC through -29X-CC suggests that the Subzone a/b boundary approximates the depth of Sample 138-844B-22X-CC.

The lowermost portion of Hole 844B contains common diatoms that exhibit moderate to poor preservation. The occurrence of *C. nicobarica*, *Nitzschia maleinterpretaria*, and *Raphidodiscus marylandicus*, and *Thalassiosira fraga* without *C. peplum* allowed us to place Samples 138-845B-29H-CC and -30H-CC in the *C. nicobarica* Zone. The absence of *Thalassiosira bukryi* suggests placement of these samples into the upper portion of this zone and suggests an age younger than 17 Ma. The occurrence of *C. coscinodiscus* in these samples indicates that these samples are no older than 17.3 Ma.

PALEOMAGNETISM

Introduction

The investigations in paleomagnetism performed at Site 844 included remanence measurements (of archive-half sections of APC cores and discrete samples from critical intervals), as well as routine measurement of low-field initial susceptibilities in whole-round sections. In Table 7, we list all cores studied.

Table 4. Interval (core and section) and depth (mbsf and mcd) constraints of planktonic foraminifer events for Site 844.

Event	Hole 844B		
	Interval (section)	Depth (mbsf)	Depth (mcd)
B *Sphaeroidinellopsis subdehiscens*	10H-CC–11H-CC	90.27–99.99	100.90–113.49
B *Globorotalia fohsi lobata*	14H-CC–15H-CC	128.26–137.82	143.09–152.82
B *Globorotalia fohsi* group	18H-CC–19H-CC	166.43–175.83	183.48–193.03
T *Globorotalia archamenardii*	18H-CC–19H-CC	166.43–175.83	183.48–193.03
B *Orbulina suturalis*	21H-CC–22H-CC	194.69–204.27	213.32–222.90
B *Praeorbulina dicana*	28H-CC–29H-CC	261.66–271.75	280.29–290.38

T = top occurrence; B = bottom occurrence.

Table 5. Interval (core and section) and depth (mbsf and mcd) constraints of radiolarian events for Site 844.

	Hole 844B			Hole 844C		
Event	Interval (section)	Depth (mbsf)	Depth (mcd)	Interval (section)	Depth (mbsf)	Depth (mcd)
B *Buccinosphaera invaginata*						
T *Stylatractus universus*	1H-1–1H-3	0.00–4.09	0.00–4.09			
B *Collosphaera tuberosa*	1H-3–1H-CC	4.09–4.53	4.09–4.53			
T *Lamprocyrtis neoheteroporos*	2H-3–2H-5	8.60–11.60	9.73–14.60			
T *Anthocyrtidium angulare*	2H-3–2H-5	8.60–11.60	9.73–14.60			
T *Theocorythium vetulum*	2H-5–2H-CC	11.60–14.48	14.60–15.61			
B *Lamprocyrtis nigriniae*	2H-5–2H-CC	11.60–14.48	14.60–15.61			
B *Theocorythium trachelium*	2H-CC–4H-3	14.48–27.63	15.61–19.08			
B *Pterocorys minythorax*	2H-CC–4H-3	14.48–27.63	15.61–19.08			
B *Anthocyrtidium angulare*	2H-CC–4H-3	14.48–27.63	15.61–19.08			
T *Pterocanium prismatium*	2H-CC–4H-3	14.48–27.63	15.61–19.08			
T *Lamprocyrtis heteroporos*	2H-5–2H-CC	11.60–14.48	14.60–20.35			
T *Anthocyrtidium jenghisi*	3H-3–4H-5	18.10–30.63	20.35–22.08			
B *Theocalyptra davisiana*	4H-5–3H-5	30.63–21.10	22.08–23.35			
T *Stichocorys peregrina*	4H-5–3H-5	30.63–21.10	22.08–23.35			
T *Anthocyrtidium pliocenica*	4H-CC–5H-3	33.48–37.14	24.93–31.01	2H-CC–3H-CC	18.62–28.66	19.92–31.01
B *Lamprocyrtis neoheteroporos*	3H-3–4H-5	18.10–30.63	20.35–22.08			
T *Phormostichoartus fistula*	4H-CC–5H-3	33.48–37.14	24.93–31.01	2H-CC–3H-CC	18.62–28.66	19.92–31.01
T *Lychnodictyum audax*	4H-CC–5H-3	33.48–37.14	24.93–31.01	2H-CC–3H-CC	18.62–28.66	19.92–31.01
T *Phormostichoartus doliolum*	4H-CC–5H-3	33.48–37.14	24.93–31.01	2H-CC–3H-CC	18.62–28.66	19.92–31.01
B *Amphirhopalum ypsilon*	4H-CC–5H-3	33.48–37.14	24.93–31.01	2H-CC–3H-CC	18.62–28.66	19.92–31.01
B *Spongaster tetras*	4H-CC–5H-3	33.48–37.14	24.93–31.01	2H-CC–3H-CC	18.62–28.66	19.92–31.01
T *Didymocyrtis penultima*	4H-CC–5H-3	33.48–37.14	24.93–31.01	2H-CC–3H-CC	18.62–28.66	19.92–31.01
T *Solenosphaera omnitubus*	4H-CC–5H-3	33.48–37.14	31.70–33.20			
T *Siphostichartus corona*	4H-CC–5H-3	33.48–37.14	34.47–40.71			
T *Acrobotrys tritubus*	4H-CC–5H-3	33.48–37.14	34.47–40.71			
T *Stichocorys johnsoni*	4H-CC–5H-3	33.48–37.14	34.47–40.71			
Stichocorys delmontensis > *S. peregrina*	4H-CC–5H-3	33.48–37.14	34.47–40.71			
T *Calocycletta caepa*	4H-CC–5H-3	33.48–37.14	34.47–40.71			
B *Solenosphaera omnitubus*	5H-3–5H-5	37.14–40.14	42.33–43.71	4H-CC–5H-CC	38.18–47.56	42.33–32.81
T *Diartus hughesi*	5H-5–5H-CC	39.14–42.90	43.71–46.55			
B *Acrobotrys tritubus*	5H-3–5H-5	37.14–40.14	40.71–42.33	3H-CC–4H-CC	28.66–38.18	31.01–42.33
B *Spongaster berminghami*	5H-3–5H-5	37.14–40.14	40.71–42.33	3H-CC–4H-CC	28.66–38.18	31.01–42.33
T *Stichocorys wolffii*	6H-5–6H-CC	49.60–52.52	53.70–56.62			
T *Botryostrobus miralestensis*	6H-5–6H-CC	49.60–52.52	53.70–56.62			
T *Diartus pettersoni*	6H-3–6H-4	46.60–48.50	50.70–52.60			
B *Lithopera bacca*	7H-CC–8H-3	62.06–65.00	68.76–72.30			
Diartus pettersoni > *D. hughesi*	6H-5–6H-CC	49.60–52.52	53.70–56.62			
B *Diartus hughesi*	6H-CC–7H-3	52.52–56.10	56.62–62.80			
T *Cyrtocapsella japonica*	6H-CC–7H-3	52.52–56.10	56.62–62.80			
T *Lithopera thornburgi*	6H-CC–7H-3	52.52–56.10	56.62–62.80			
T *Carpocanium cristata*	7H-CC–8H-3	62.06–65.60	68.76–72.30			
T *Lithopera renzae*	11H-5–11H-CC	97.10–99.99	110.60–113.49			
T *Cyrtocapsella cornuta*	11H-3–11H-5	94.10–97.10	107.60–110.60			
B *Diartus pettersoni*	11H-5–11H-CC	97.10–99.99	110.60–113.49			
T *Dorcadospyris alata*	11H-5–11H-CC	97.10–99.99	110.60–113.49			
B *Cyrtocapsella japonica*	12H-CC–13H-3	109.59–113.09	126.15–126.89	12H-CC–13H-CC	114.20–123.62	126.15–136.62
B *Calocycletta caepa* s.s.	17H-5–17H-CC	154.10–157.07	169.70–172.67			
B *Lithopera thornburgi*	15H-5–15H-CC	135.10–137.82	150.10–152.82			
T *Stichocorys armata*	18H-3–18H-CC	160.60–166.43	178.50–183.48	17H-CC–18H-CC	161.50–171.19	178.50–188.14
T *Liriospyris parkerae*	20H-5–20H-CC	182.60–185.58	201.23–204.21			
T *Carpocanium bramlettei*	23X-5–23X-CC	211.40–213.90	230.03–232.53			
T *Calocycletta costata*	24X-CC–25X-3	223.65–227.69	242.28–246.32			
Dorcadospyris dentata > *Dorcadospyris alata*	25X-CC–26X-3	232.04–237.42	250.67–256.25			
T *Liriospyris stauropora*	25X-CC–26X-3	232.04–237.42	250.67–256.25			
B *Liriospyris parkerae*	26X-3–26X-5	237.42–240.39	256.25–259.22			
T *Stichocorys diaphenes*	27X-CC–28X-CC	243.3–261.66	261.93–280.29			
B *Carpocanium bramlettei*	29X-CC–30X-CC	271.75–281.47	290.38–300.10			
B *Acrocubus octopyle*	29X-3–29X-5	266.00–268.99	284.63–287.62			
T *Carpocanium cingulata*	29X-CC–30X-CC	271.75–281.47	290.38–300.10			
B *Giraffospyris toxaria*	30X-CC–31X-5	281.47–288.30	300.10–306.93			

T = top occurrence; B = bottom occurrence.

Measurements of discrete samples confirmed that two distinct polarities could be isolated after removal with AF demagnetization of a large vertical upward overprint (Fig. 17). The pass-through magnetometer results from Hole 844B indicated that one of the two APC cores used produced an overprint that was considerably more severe than the other (the even-numbered cores showed overprints that resisted demagnetization, compared with the odd-numbered cores). Thus, before coring Hole 844C, the even-numbered barrel was replaced with a barrel that appeared (on the basis of the core technician's mechanical meter) to have a lower external field. Replacement of the even-numbered barrel appears to have improved the paleomagnetic record obtained in Holes 844C and 844D, in comparison

Table 5 (continued).

	Hole 844D		
Event	Interval (section)	Depth (mbsf)	Depth (mcd)
B *Buccinosphaera invaginata*			
T *Stylatractus universus*			
B *Collosphaera tuberosa*			
T *Lamprocyrtis neoheteroporos*			
T *Anthocyrtidium angulare*			
T *Theocorythium vetulum*			
B *Lamprocyrtis nigriniae*			
B *Theocorythium trachelium*			
B *Pterocorys minythorax*			
B *Anthocyrtidium angulare*			
T *Pterocanium prismatium*			
T *Lamprocyrtis heteroporos*			
T *Anthocyrtidium jenghisi*			
B *Theocalyptra davisiana*			
T *Stichocorys peregrina*			
T *Anthocyrtidium pliocenica*	1H-3	27.00	31.70
B *Lamprocyrtis neoheteroporos*			
T *Phormostichoartus fistula*	1H-3	27.00	31.70
T *Lychnodictyum audax*	1H-3	27.00	31.70
T *Phormostichoartus doliolum*	1H-3	27.00	31.70
B *Amphirhopalum ypsilon*	1H-3	27.00	31.70
B *Spongaster tetras*	1H-3	27.00	31.70
T *Didymocyrtis penultima*			
T *Solenosphaera omnitubus*	1H-3	27.00	31.70
T *Siphostichartus corona*	1H-4	30.00	34.70
T *Acrobotrys tritubus*	1H-4	30.00	34.70
T *Stichocorys johnsoni*	1H-4	30.00	34.70
Stichocorys delmontensis	1H-4	30.00	34.70
> *S. peregrina*	1H-4	30.00	34.70
T *Calocycletta caepa*	1H-4	30.00	34.70
B *Solenosphaera omnitubus*			
T *Diartus hughesi*			
B *Acrobotrys tritubus*			
B *Spongaster berminghami*			
T *Stichocorys wolffii*			
T *Botryostrobus miralestensis*			
T *Diartus pettersoni*			
B *Lithopera bacca*			
Diartus pettersoni			
> *D. hughesi*			
B *Diartus hughesi*			
T *Cyrtocapsella japonica*			
T *Lithopera thornburgi*			
T *Carpocanium cristata*			
T *Lithopera renzae*			
T *Cyrtocapsella cornuta*			
B *Diartus pettersoni*			
T *Dorcadospyris alata*			
B *Cyrtocapsella japonica*			
B *Calocycletta caepa* s.s.			
B *Lithopera thornburgi*			
T *Stichocorys armata*			
T *Liriospyris parkerae*			
T *Carpocanium bramlettei*			
T *Calocycletta costata*			
Dorcadospyris dentata			
> *Dorcadospyris alata*			
T *Liriospyris stauropora*			
B *Liriospyris parkerae*			
T *Stichocorys diaphenes*			
B *Carpocanium bramlettei*			
B *Acrocubus octopyle*			
T *Carpocanium cingulata*			
B *Giraffospyris toxaria*			

with the highly overprinted records recovered from even-numbered cores in Hole 844B (Fig. 18).

Results

Remanence Intensity and Low-Field Magnetic Susceptibility

An excellent correspondence is seen between remanence intensity and low-field susceptibility (Fig. 19). The most prominent feature of these records is an overall decrease of both parameters down the core. We obtained no reliable determination of remanence directions below about 70 mcd (~65 mbsf) from pass-through measurements; single samples could not be demagnetized on board the ship because the NRM remanence intensity decreased below the sensitivity of the spinner magnetometer. The pass-through measurements below 70 mcd show a consistent decrease in intensity from the top to the bottom of each core measured (Fig. 20). This perhaps reflects a small amount of contamination introduced to the top of each core that spread downward during coring.

Paleomagnetic Directions

Results of discrete sample measurements (Table 8) compare well with the pass-through magnetometer records, except, of course, for those intervals where the pass-through records remain highly over-printed (e.g., those shown in Fig. 18A). In particular, the declination results are in good agreement for all samples measured. The characteristic component, as determined from the discrete sample results (Table 8), has a mean inclination of 13°, in good agreement with the dipole latitude expected for this site (16°). These results confirm that the characteristic component of magnetization is, for the most part, being reasonably revealed by AF cleaning to 15 mT; however, the pass-through magnetometer record (from the archive halves) does commonly show anomalously steep inclinations.

The uppermost 65 mbsf showed generally stable directions after AF treatment in both Holes 844B (Figs. 21 and 22) and 844C (Figs. 23 and 24). For the most part, orientation was provided by the multishot orientation tool. The topmost cores (138-844A-1H, -844B-1H to -3H, -844C-1H to -3H, and -844D-1H) could not be oriented (see "Explanatory Notes" chapter, this volume), and so we adjusted the declinations uniformly in each of these cores to bring the mean declination of the normal polarity zones to approximately 0°. Both adjusted and multishot orientations are listed in Table 9. At this site, the multishot orientation appears generally to be reliable to within 30° or 40°.

Magnetostratigraphic Synthesis

The magnetostratigraphy obtained correlates well from core to core when plotted on a composite depth scale (Fig. 25). The only significant discrepancy is found in Cores 138-844B-7H and -844C-7H. Generally, this reflects the increasing difficulty when resolving reversal boundaries at increasing depths. For example, our correlation with the termination of Chron C5 in Core 138-844C-7H may not prove correct. However, we anticipate that such minor difficulties may be resolved with further shore-based work on discrete samples.

The correlation of the various magnetozones to the magnetic polarity time scale generally is straightforward (Table 10). Our original identification of the various magnetozones in Hole 844B, based on core-catcher biostratigraphic constraints, proved to be consistent with

Table 6. Sample and depth (mbsf) constraints of diatom events for Site 844.

Event	Hole 844B			Hole 844C		
	Interval (section)	Depth (mbsf)	Depth (mcd)	Interval (section)	Depth (mbsf)	Depth (mcd)
T *Nitzschia reinholdii*	1H-CC–2H-CC	4.53–14.48	4.53–15.60	<1H-CC	<9.10	<9.60
B *Pseudoeunotia doliolus*	3H-2–3H-4	14.75–19.30	17.00–21.55	1H-CC–2H-CC	9.10–18.62	9.60–19.92
T *Nitzschia jouseae*	4H-3–4H-CC	26.10–33.48	17.55–24.93			
B *Rhizosolenia praebergonii*	4H-3–4H-CC	26.10–33.48	17.55–24.93	2H-CC–3H-CC	18.62–28.66	19.92–31.01
B *Nitzschia jouseae*	4H-CC–5H-1	33.48–34.20	24.93–37.85			
T *Nitzschia miocenica*	4H-CC–5H-1	33.48–34.20	24.93–37.85	3H-CC–4H-CC	28.66–38.18	31.01–42.33
T *Nitzschia miocenica* var. *elongata*	4H-CC–5H-1	33.48–34.20	24.93–37.85			
T *Thalassiosira praeconvexa*	4H-CC–5H-1	33.48–34.20	24.93–37.85			
B *Thalassiosira convexa*	5H-1–5H-2	34.20–35.70	37.85–39.35	3H-CC–4H-CC	28.66–38.18	31.01–42.33
B *Thalassiosira praeconvexa*	5H-2–5H-3	35.70–37.90	39.35–41.55			
B *Nitzschia miocenica*	5H-3–5H-5	37.90–40.20	41.55–43.85	4H-CC–5H-CC	38.18–47.56	42.33–52.81
T *Rossiella paleacea*	5H-3–5H-5	37.90–40.20	41.55–43.85	4H-CC–5H-CC	38.18–47.56	42.33–52.81
B *Nitzschia reinholdii* s. ampl.	5H-5–5H-6	40.20–41.70	43.85–45.35	4H-CC–5H-CC	38.18–47.56	42.33–52.81
T *Thalassiosira yabei*	5H-CC–6H-1	42.90–43.70	46.55–47.80	5H-CC–6H-CC	47.56–57.20	52.81–63.85
B *Nitzschia cylindrica* s. ampl.	6H-1–6H-2	43.70–45.20	47.80–49.30			
T *Coscinodiscus loeblichii*	6H-4–6H-CC	49.70–52.52	53.80–56.62			
B *Thalassiosira burcklina*	6H-4–6H-CC	49.70–52.52	53.80–56.62			
B *Coscinodiscus loeblichii*	6H-CC–7H-CC	52.52–62.06	56.62–68.76			
T *Denticulopsis hustedtii*	7H-5–7H-CC	59.00–62.06	65.70–68.76	6H-CC–7H-CC	57.20–66.73	63.85–74.38
T *Actinocyclus moronensis*	8H-1–8H-2	62.70–64.20	69.85–71.35	6H-CC–7H-CC	57.20–66.73	63.85–74.38
T *Synedra jouseana*	9H-CC–10H-CC	81.10–90.27	89.75–100.90			
T *Crasepedodiscus coscinodiscus*	9H-CC–10H-CC	81.10–90.27	89.75–100.90	8H-CC–9H-CC	76.30–85.78	85.61–95.96
B *Rossiella paleacea* var. *elongata*	9H-CC–10H-CC	81.10–90.27	89.75–100.90			
T *Actinocyclus ingens*	12H-CC–13H-CC	109.59–118.95	123.12–132.75	12H-CC–13H-CC	114.15–123.62	126.15–136.62
T *Cestodiscus pulchellus*	12H-CC–13H-CC	109.59–118.95	123.12–132.75			
B *Coscinodiscus temperi* var. *delicata*	12H-CC–13H-CC	109.59–118.95	123.12–132.75			
T *Annellus californicus*	12H-CC–13H-CC	109.59–118.95	123.12–132.75	12H-CC–13H-CC	114.15–123.62	126.15–136.62
T *Coscinodiscus lewisianus*	14H-CC–15H-CC	128.26–137.82	143.09–152.82	14H-CC–15H-CC	132.71–142.80	147.71–157.70
T *Thalassiosira tappanae*	15H-CC–16H-CC	137.82–147.43	152.82–163.61			
B *Triceratium cinnamomeum*	15H-CC–16H-CC	137.82–147.43	152.82–163.61	15H-CC–16H-CC	142.80–152.16	157.70–167.66
B *Denticulopsis hustedtii*	16H-CC–17H-CC	147.43–157.07	163.61–172.67			
T *Cestodiscus peplum*	17H-CC–18H-CC	157.07–166.43	172.67–183.48			
B *Actinocyclus ellipticus*	18H-CC–19H-CC	166.43–175.83	183.48–193.03			
B *Coscinodiscus blysmos*	19H-CC–20H-CC	175.83–185.58	193.03–204.21			
T *Annellus californicus*	21H-CC–22H-CC	194.69–204.27	213.32–222.90			
B *Actinocyclus ingens*	23H-CC–24H-CC	213.90–223.65	232.53–242.28			
T *Coscinodiscus lewisanus* var. *similis*	24H-CC–25H-CC	223.65–232.04	242.28–250.67			
T *Thalassiosira fraga*	28H-CC–29H-7	261.66–270.70	280.29–289.33			
B *Cestodiscus peplum*	28H-CC–29H-7	261.66–270.70	280.29–289.33			
T *Raphidodiscus marylandicus*	28H-CC–29H-7	261.66–270.70	280.29–289.33			
B *Craspedodiscus coscinodiscus* s. str.	>30H-CC	>281.47	>300.10			
B *Crucidenticula nicobarica*	>30H-CC	>281.47	>300.10			

T = top occurrence; B = bottom occurrence.

the more detailed determination of zonal boundaries obtained later. Indeed, the record appeared so uniform that the initial interpretation of Hole 844C, performed without direct reference to biostratigraphic control, proved consistent with all available constraints. Thus, the shipboard results from this site appear to show a continuous magnetostratigraphy that spans the interval from the Holocene to approximately 10 Ma.

SEDIMENTATION RATES

A sedimentary section almost 300 m thick that covers the time interval from the late Pleistocene to the early Miocene was recovered at Site 844. Biostratigraphic age control was provided by all four of the chief planktonic microfossil groups. In addition, an excellent paleomagnetic record was obtained for the upper part of the section. To use these data to best advantage, we thought it appropriate to use the shipboard composite depths (see Chapter 5, this volume). Over short time intervals, the uncertainties involved when using unadjusted depths would add significantly to the errors when estimating sedimentation rates.

The composite depth section for Site 844 is given in Table 11. This composite was formed by comparing shipboard measurements of GRAPE, magnetic susceptibility, and percent reflectance (from the automated color analyzer) at adjacent holes. These comparisons were

integrated to form a single composite depth section for Site 844 (a detailed discussion about the construction of composite sections during Leg 138 is presented in Hagelberg et al., this volume). For the holes and cores listed in Column 1 of Table 11, Column 2 presents the ODP depth (mbsf) of the core top and core bottom (mbsf). Note that in Column 2 the depth to the bottom of the recovered core is presented. This depth is necessary to place the core-catcher samples in their corect position in the composite depth section and is not the same as the standard ODP core-catcher depth. Column 3 shows the length of core recovered. Column 4 gives the composite depth of the core top and core bottom (in mcd). Column 5 indicates the amount of offset between the ODP depth and the composite depth. For each core, conversion from ODP depth (mbsf) of any sample to composite depth (mcd) is performed by adding the offset listed in Column 5 for that core. To maintain consistency between the portions of the section recovered by APC and by XCB, all XCB cores have been offset by the same amount as the last APC core in the composite depth section.

The creation of the upper 60 m of the composite section for Site 844 was determined mainly from the susceptibility records for Holes 844A, 844B, 844C, and 844D, because GRAPE and percentage of reflectance values have lower amplitude variations in this part of the section (see back-pocket Fig. 26). Below about 60 mcd, the magnetic susceptibility in Holes 844B and 844C becomes much weaker, and the construction of composite depths was guided by both GRAPE and

Table 7. Cores analyzed with pass-through magnetometer system at Site 844.

| Core	Treatment (mT)
138-844A-	
1H	NRM, 10
138-844B-	
1H	NRM, 10
2H	NRM, 10
3H	NRM, 10
4H	NRM, 10
5H	NRM, 10
6H	NRM, 10
7H	NRM, 10
8H	NRM, 10
9H	NRM, 10
10H	NRM, 10
11H	NRM, 10
12H	NRM, 10
13H	NRM, 10
138-844C-	
1H	NRM, 15
2H	NRM, 15
3H	NRM, 15
4H	NRM, 15
5H	NRM, 15
6H	NRM, 15
7H	NRM, 15
8H	NRM, 15
9H	NRM, 15
138-844D-	
1H	NRM, 15

Figure 17. Zijderveld demagnetization diagrams showing the pervasive vertical upward overprint encountered in samples from Site 844. Azimuthal orientation is with respect to the double line on core liner.

percentage of reflectance values. Through approximately 128 mcd, hole-to-hole correlations using GRAPE records were consistent with correlations using percentage of reflectance records. In the interval from approximately 128 to 138 mcd, correlations using the GRAPE records were less well constrained, but the percentage of reflectance records were well correlated in this interval (see back-pocket Fig. 26). From 138 to 204 mcd (the last interval that was cored twice using the APC), construction of composite sections using both GRAPE and percentage of reflectance values again yielded similar results.

Analysis of the composite depth section shows that from the cored intervals in Holes 844A, 844B, 844C, and 844D we recovered a continuous section down to 200 mcd. While Cores 138-844B-3H and -4H appear to indicate a double-cored interval, the offset coring in Holes 844C (Cores 138-844C-3H and -4H) and 844D (Core 138-844D-1H) combine to give a continuous record through this interval (see back-pocket Fig. 26). Cores from Holes 844B and 844C in the remainder of the section continue to overlap one another by between approximately 3 and 6 m. Composite depths for Site 844 appear to be consistent with the locations of magnetic reversal boundaries (see "Paleomagnetism" section, this chapter) in each hole to within less than 30 cm. An exception may be the interval interpreted as covering Chron C4A-n3 and the top of Chron C5n, where further investigation will be required to resolve an apparent conflict.

With few exceptions, all fossil groups gave similar age estimates for the samples examined. Table 12 lists the ages selected to create an age-vs.-depth plot. In view of the excellent paleomagnetic record, magnetic reversals were used for time control in the upper 65 mcd. Figure 27 displays the biostratigraphic data in the general form on which age-vs.-depth plots have been constructed.

Average linear sedimentation rates have been derived from the control points using shipboard composite depths and are shown in
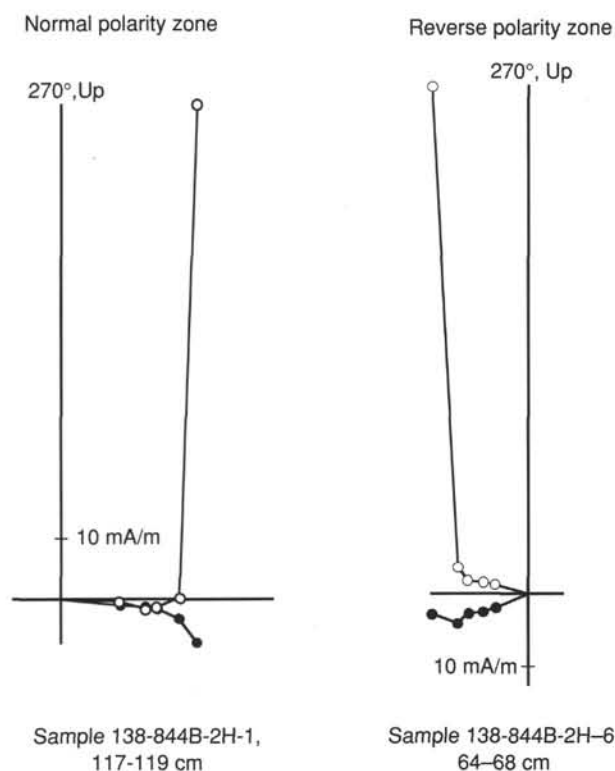
Figure 28 plotted vs. age and in Figure 29, plotted vs. depth. During the Pleistocene, the linear sedimentation rate was about 15 m/m.y. This rate is consistent with magnetic susceptibility cycles (see "Paleomagnetism" section, this chapter) that indicate a wavelength of about 1.5 m for presumed 100-k.y. glacial/interglacial cycles. Below the major glacial cycles, the sedimentation rate decreases to about 5 m/m.y.; this rate was low through the entire Pliocene, with an average near 3 m/m.y. between 2.5 and 4.5 Ma. Late Miocene rates are slightly higher, with a minor peak near 10 m/m.y. between 6.5 and 8 Ma. Despite these low rates, the detailed sequence of microfossil datums that was observed (see "Biostratigraphy" section, this chapter) shows that no significant hiatus occurred, an indication that is supported by the paleomagnetic results. Over the past 10 m.y., paleomagnetic control has allowed us to determine sedimentation rates with a reasonable degree of precision because the magnetic reversals are located to within 5 to 10 cm in the core. However, the absolute ages of the middle Miocene age controls are subject to uncertainties, such that meaningful sedimentation rates may be obtained only by estimating over fairly wide intervals. The interval between 9 and 10.5 Ma indicates a rate of 7.5 m/m.y.; this is preceded by the high rate of 35 m/m.y. over the interval 10.5 to 13.5 Ma. Similar high rates persist to the base of the section; between 13.5 and 16 Ma, 29 m/m.y.; and between 16 Ma and the base of the section, about 39 m/m.y.

The suddenness of the change in sedimentation rate at 10.5 Ma at the point where we lose paleomagnetic control may be exaggerated by the method used for estimating it; nonetheless, because all of Core 138-844B-9H accumulated within Chron 5, a rapid change in sedimentation rate must have occurred near the point where we constructed it. Possibly, the much higher sedimentation rate prior to 10.5 Ma is responsible for the weak magnetic signal in Site 844 below this point. On the other hand, the break in sedimentation rate might not have appeared so sudden had we had better time control at this break point.
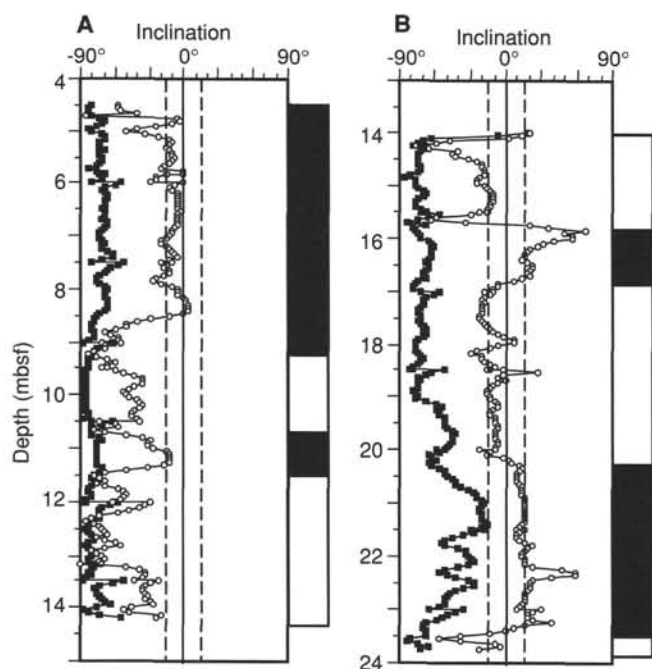
Figure 18. Inclination records from passthrough magnetometer. **A.** Core 138-844B-2H is an example where steep upward overprinting has not been reliably removed with 10-mT demagnetization treatments. **B.** Core 138-844B-3H is an example where steep upward overprinting has been generally well removed with 10-mT treatments. Black represents zones of normal polarity; white, zones of reverse polarity (as determined from complete vector information). Dashed lines show dipole inclination for this site. Solid square = NRM; open circle = 10-mT demagnetization.

The control point that we used to estimate sedimentation rates from 16 to 17.3 Ma is artificial. The lowest sample examined is above a diatom datum that was calibrated to 17.3 Ma. Thus, the rate estimated below 16 Ma should be a lower limit, although in reality it may be exaggerated because the time interval between the nannofossil datum at 16 Ma and the diatom datum at 17.3 Ma was not estimated directly.

INORGANIC GEOCHEMISTRY

Twenty interstitial-water samples were collected at Site 844: six from Hole 844A at depths ranging from 2.0 to 11.0 mbsf and 14 from Hole 844B at depths ranging from 42.6 mbsf to basement at 309.6 mbsf (Table 13). Here, results from these two holes have been considered as constituting a single depth profile. All interstitial-water samples from Hole 844A were recovered within the diatomaceous ooze and clay that composes lithologic Unit I (see "Lithostratigraphy" section, this chapter). Only one interstitial-water sample from Hole 844B (Section 138-844B-6H-4) was collected from within Unit I. The remainder of the interstitial-water samples from Hole 844B were recovered from the carbonate/siliceous sediments of Unit II, including the deepest sample (Section 138-844B-31X-7), which was squeezed from red metalliferous sediment at the bottom of the last section.

Chemical gradients at this site are subtle (Table 13), being governed by the biogenic-rich, organic-carbon-poor character of the sediments and by the diffusive influence of basalt alteration reactions at depth. Interstitial-water profiles at this site are similar to those at the nearby Site 495, occupied during DSDP Leg 67 (Harrison et al., 1982).

Sodium (Fig. 30A), as calculated by charge balance, decreases slightly in the middle of Hole 844B, then increases into basement (309.6 mbsf). Note that sodium increases in a regular way between 280 mbsf and basement then returns to bottom-water values at the bottom of this hole.
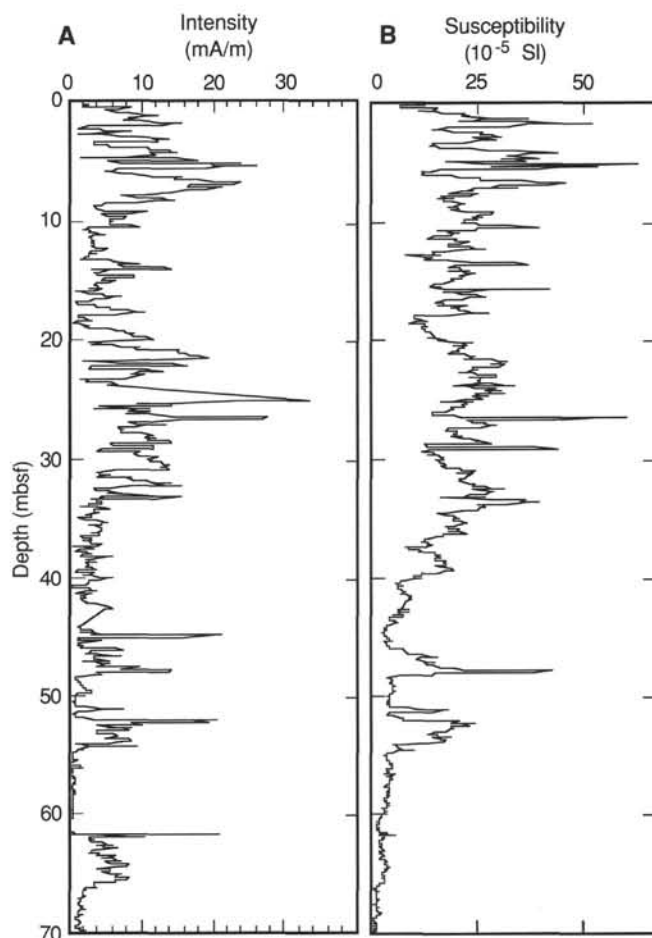

Figure 19. Evolution down the core of remanence intensity (**A**) and low-field initial susceptibility (**B**) in the upper 70 m of Hole 844B.

Chlorinity (Fig. 30B) does not vary at this site (558 ±3 mM), within our ability for measuring this value (0.4%). Chlorinity, while monotonously the same down the core, does demonstrate that pristine, undiluted interstitial waters were collected during coring.

Alkalinity (Fig. 30C) in the top 250 mbsf (through Section 138-844B-25X-4) remains constant (2.990 ±0.076 mM) and only slightly higher than standard seawater from the International Association of Physical Sciences Organizations (IAPSO; 2.45 mM). In contrast, alkalinities for reducing sediments (i.e., 0 sulfate), such as those sampled by Harrison et al. (1982) at Sites 496 and 497 on the slope of the Mid America Trench during DSDP Leg 67, can reach concentrations that are 40 times the levels found at this site. The low alkalinity at Site 844 is indicative of oxidizing sediments and suggests that diagenetic reactions have been restricted to oxic and suboxic reactions during early diagenesis. The profile of sulfate with depth (Fig. 30D) is consistent with this scenario. While sulfate decreases steadily down to 250 mbsf, the absolute change is only 5%.

The total downhole change in magnesium at this site (Fig. 31A) is 2.0 mM, or about 4%, which is 8-fold larger than the precision of the titration technique used to measure this value (0.5%). Nevertheless, it is difficult to identify a discernable trend in this profile.

Downhole changes in calcium at Site 844 (Fig. 31B) are extremely small. The difference between the concentration near the sediment/water interface (10.16 mM) and that in Section 138-844B-30X-4 from 296.5 mbsf is 0.63 mM. Still, this shift represents an overall change of more than 6%. Moreover, slightly elevated dissolved calcium concentrations seem to exist in the most calcareous-rich sections of the hole (see
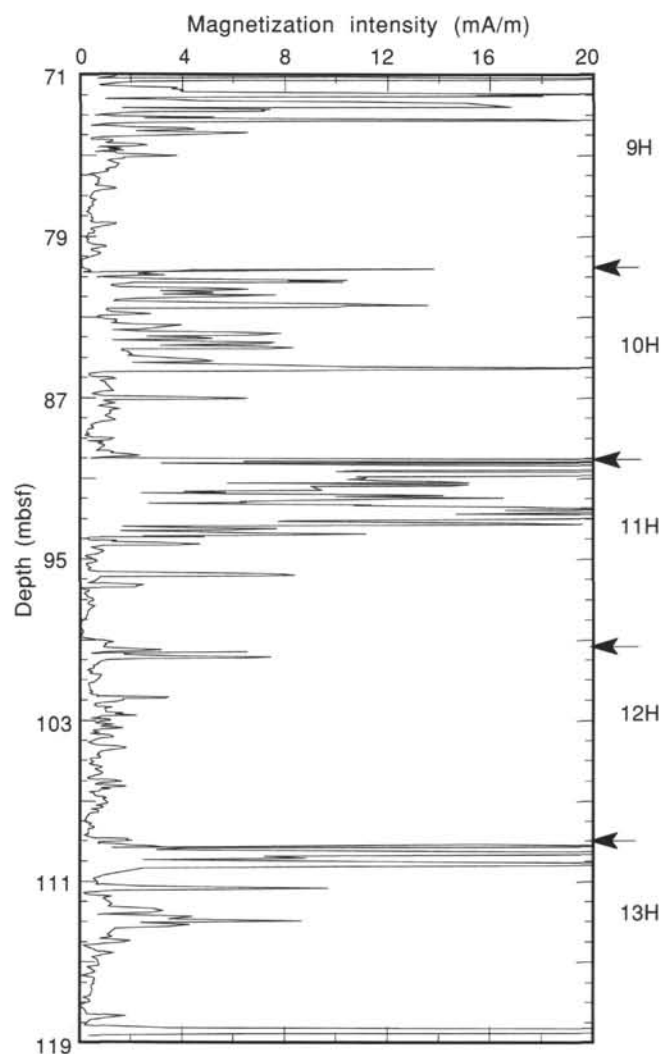
Figure 20. Remanence intensity in Hole 844B over an interval from which no reliable directions were obtained. Arrows indicate depth of core tops.

Table 8. Principal component analysis of Site 844 discrete sample data.

Core, section, interval (cm)	Declination (degrees)	Inclination (degrees)
138-844B-		
1H-2, 40	234.8	19.7
1H-3, 40	284.9	11.6
2H-1, 117	5.5	4.8
2H-6, 64	160.7	−13.3
2H-7, 66	329.5	−13.8
3H-2, 135	139.7	17.0
3H-7, 53	319.0	−10.5
4H-3, 88	249.8	8.1
4H-4, 88	63.6	−0.9
4H-5, 85	98.2	−12.8
5H-1, 70	223.6	−24.6
5H-2, 70	216.1	−14.0
5H-3, 70	234.5	−19.2
5H-4, 80	229.0	−14.8
5H-5, 88	78.7	20.5
5H-6, 78	82.0	22.4
138-844C-		
2H-1, 50	254.0	−24.4
2H-1, 101	255.9	−6.7
2H-1, 101	257.9	−9.6
2H-2, 10	115.0	30.6
2H-3, 76	280.6	−11.2
2H-5, 146	293.1	−9.8
3H-1, 77	129.0	−2.6
3H-3, 135	297.2	11.6
3H-4, 10	115.9	−6.2
5H-3, 48	243.4	6.5
6H-2, 125	252.8	7.8
7H-1, 45	219.0	9.4

Note: Principal component fits are anchored to the origin. Declinations are given with respect to double fiducial lines on core liner.

"Organic Geochemistry" section, this chapter), centered at 180 mbsf. This level consists of foraminifer ooze containing about 60% calcareous nannofossils, with intervals of diatom-rich (up to 25%) sediment. This result suggests that a small degree of recrystallization is occurring, even at these relatively low overburdens. This interpretation should be consistent with silica (Fig. 31D) and strontium (Fig. 32B) profiles at this site, both of which exhibit broad maxima in the middle Miocene sections of this hole.

A small, but statistically significant, decrease in potassium occurs (Fig. 31C) down the core. The total top-to-bottom change in potassium amounts to a relative change of 19%, which is 10-fold larger than the precision of the measurement. Interstitial potassium tends to decrease down this hole, which is opposite to the trend for calcium. In fact, a moderate negative correlation ($R^2 = -0.62$) exists between calcium and potassium down this hole, especially if one ignores the bottommost sample (which obviously is anomalous). The inverse relationship between interstitial potassium and calcium is consistent with the view put forward by McDuff and Gieskes (1976) that distributions of these elements in DSDP pore fluids have been regulated by different processes. In this view, calcium increases in interstitial waters in response to recrystallization of calcite, while potassium often decreases down the core as a result of its uptake during low-temperature alteration of basement rocks (McDuff, 1981).

Recrystallization and basalt alteration seem to dominate the interstitial-water chemistry at Site 844. The effects of these two processes are clearly seen in profiles of silica, lithium, and strontium.

Silica (Fig. 31D) is released to interstitial waters during the recrystallization of biogenic silica (Gieskes, 1974). This process should explain the increase in silica down to about 220 mbsf. The trend below this depth apparently has been influenced by uptake into basal sediment and basement rocks.

Strontium (Fig. 32B) displays a trend similar to silica. Concentrations of interstitial strontium are known to increase during alteration of volcanic material and during the recrystallization of calcite (Elderfield and Gieskes, 1982). Lithium (Fig. 32A) displays a trend opposite to that of strontium. The lithium profile is indicative of substantial removal within the sediment column, with a shift back toward a seawater value in the bottom interval, similar to sodium.

ORGANIC GEOCHEMISTRY

Carbonate and Organic Carbon

Concentrations of inorganic carbon, total carbon, and total nitrogen were measured in samples from the two lithologic units recovered at Site 844. From these data, we calculated the weight percent of calcium carbonate (%CaCO$_3$) and organic carbon (%C$_{org}$). Analytical methods and errors are outlined in the "Explanatory Notes" chapter (this volume). We analyzed lithologic Unit I in greater detail because this unit shows considerable variation in the relative proportions of carbonate and biogenic opal (see "Lithostratigraphy" section, this chapter). The mean analytical result for each chemical index in each sample is listed in Table 14 (CD ROM, back pocket) with respect to
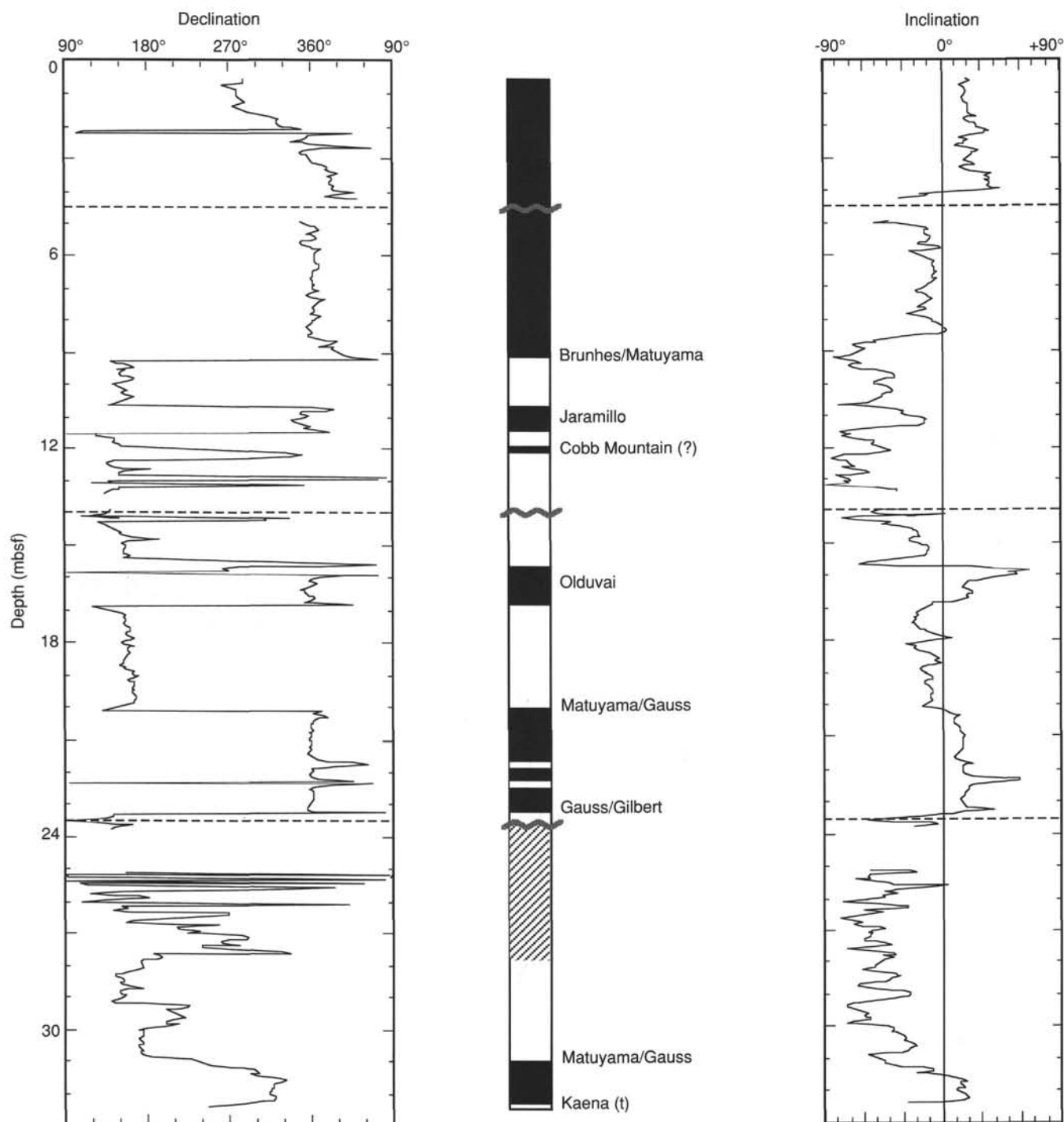
Figure 21. Passthrough magnetometer results (after 10-mT demagnetization) and identification of reversal boundaries from 0 to 33 mbsf in Hole 844B. Black = normal, white = reverse, hatched area = no data or no interpretation. Declinations are rotated as described in text and Table 9. Dashed lines indicate location of core tops.

both ODP depth (mbsf) and to composite depth (mcd; see "Composite Depth" section, this chapter). Duplicate analyses of aliquots from the same sample show that, on average, the percentage of CaCO$_3$ values are reproducible to within 0.4% (Table 15).

The percentages of CaCO$_3$ and C$_{org}$ values from the four holes drilled at Site 844 (Table 14, CD ROM) are presented with respect to ODP depth in Figure 33. Figure 34 shows percentages of CaCO$_3$ and

C$_{org}$ vs. composite depth and age (see also "Sedimentation Rates" section, this chapter).

The average percentage of CaCO$_3$ in lithologic Unit I (0–69.5 mbsf in Hole 844B; 0–76.6 mcd) is 19.3% and ranges from 0% to 79%. Average percentage of C$_{org}$ in Unit I is 0.4% and ranges from 0% to 1.2%. Lithologic Unit II (69.5–290.8 mbsf; 76.6–309.4 mcd in Hole 844B) is composed of nannofossil ooze with variable admixtures of clay and
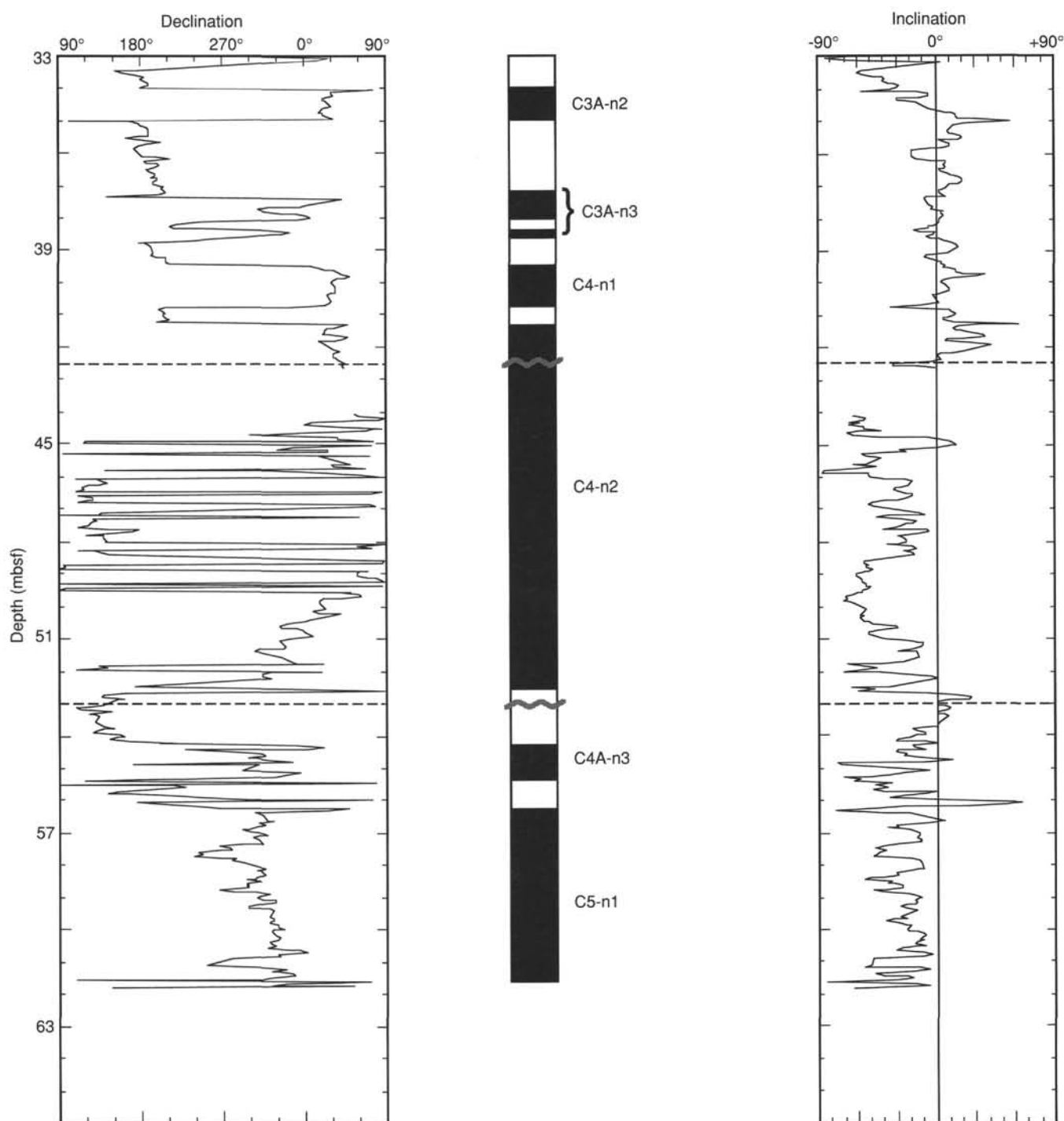
149

Figure 22. Passthrough magnetometer results (after 10-mT demagnetization) and identification of reversal boundaries from 33 to 62 mbsf in Hole 844B. Black = normal, white = reverse. Declinations are rotated as described in text and Table 9. Dashed lines indicate location of core tops.

diatoms. Unit II has a uniformly high percentage of $CaCO_3$ that averages 75% and ranges from 25% to 90%. Concentrations of organic carbon in Unit II could not be determined accurately by shipboard techniques because of high carbonate concentrations and generally were below 0.2%.

Accumulation Rates

We calculated the average values of several sedimentary parameters that correspond to the 14 time intervals extending from 0 to 18 Ma delimited by the chronostratigraphic levels discussed in the "Sedimenta-

tion Rates" section (this chapter). The dry-bulk density (DBD; in g/cm^3) of 87 of the samples listed in Table 14 (CD ROM) was determined in the physical properties laboratory. A curve fit through a scatter plot of percentage of $CaCO_3$ vs. DBD (Fig. 35) is expressed as

$$DBD = 0.2846 \times 10^{\wedge}(0.00599 \times \%CaCO_3) \quad R^2 = 0.91.$$

This empirical relationship was used to estimate a DBD value for every sample in Table 14 for which a percentage of $CaCO_3$ value was
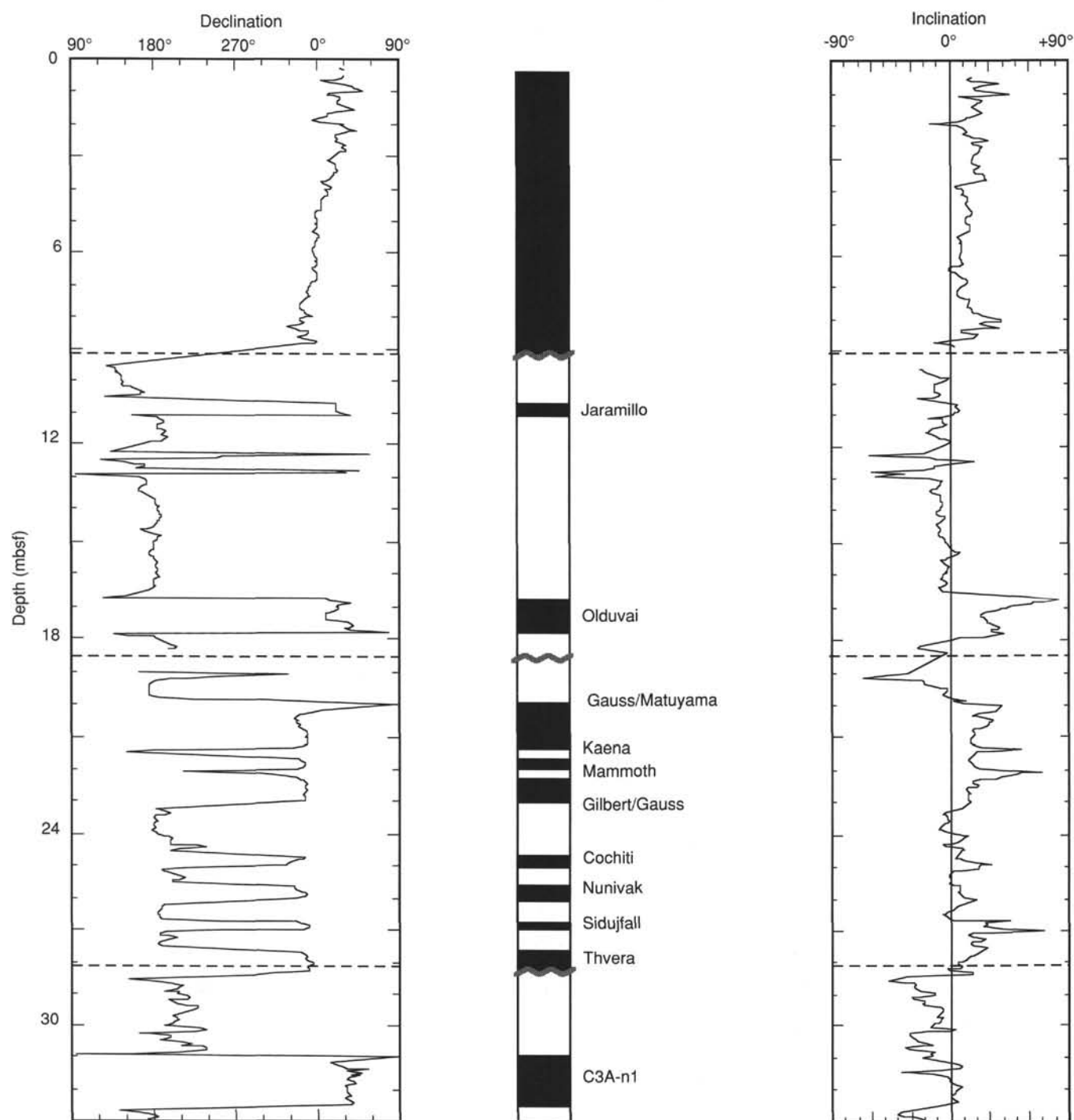
Figure 23. Passthrough magnetometer results (after 15-mT demagnetization) and identification of reversal boundaries from 0 to 33 mbsf in Hole 844C. Black = normal, white = reverse. Declinations are rotated as described in text and Table 9. Dashed lines indicate location of core tops.

determined. The average values of percentages of CaCO₃ and C_org, linear sedimentation rate (LSR), DBD, bulk sediment mass accumulation rate (MAR), CaCO₃ MAR, noncarbonate MAR, and C_org MAR were calculated according to the methodology outlined in the "Explanatory Notes" chapter (this volume) and are listed in Table 16. Accumulation rates are presented in Figures 36 and 37, plotted vs. composite depth and age, respectively. Mean bulk sediment MAR decreased over time from 3 g/cm²/k.y. in the middle Miocene to 0.1 g/cm²/k.y. in the middle Pliocene

(Fig. 37). Pleistocene MARs were a factor of 2 to 4 times higher than Pliocene MARs. The greatest change in the sedimentary record occurred near 10.4 Ma, when the mean LSR and the sedimentary and chemical accumulation rates decreased by a factor of 6 (Fig. 37). Short-term excursions in accumulation rates correspond to abrupt and short-lived changes in lithology and DBD. For example, a distinct decrease in percentage of CaCO₃ and thus in the estimated DBD at 11.7 Ma resulted in a dramatic decrease in bulk sediment and CaCO₃ MAR (Fig. 37).
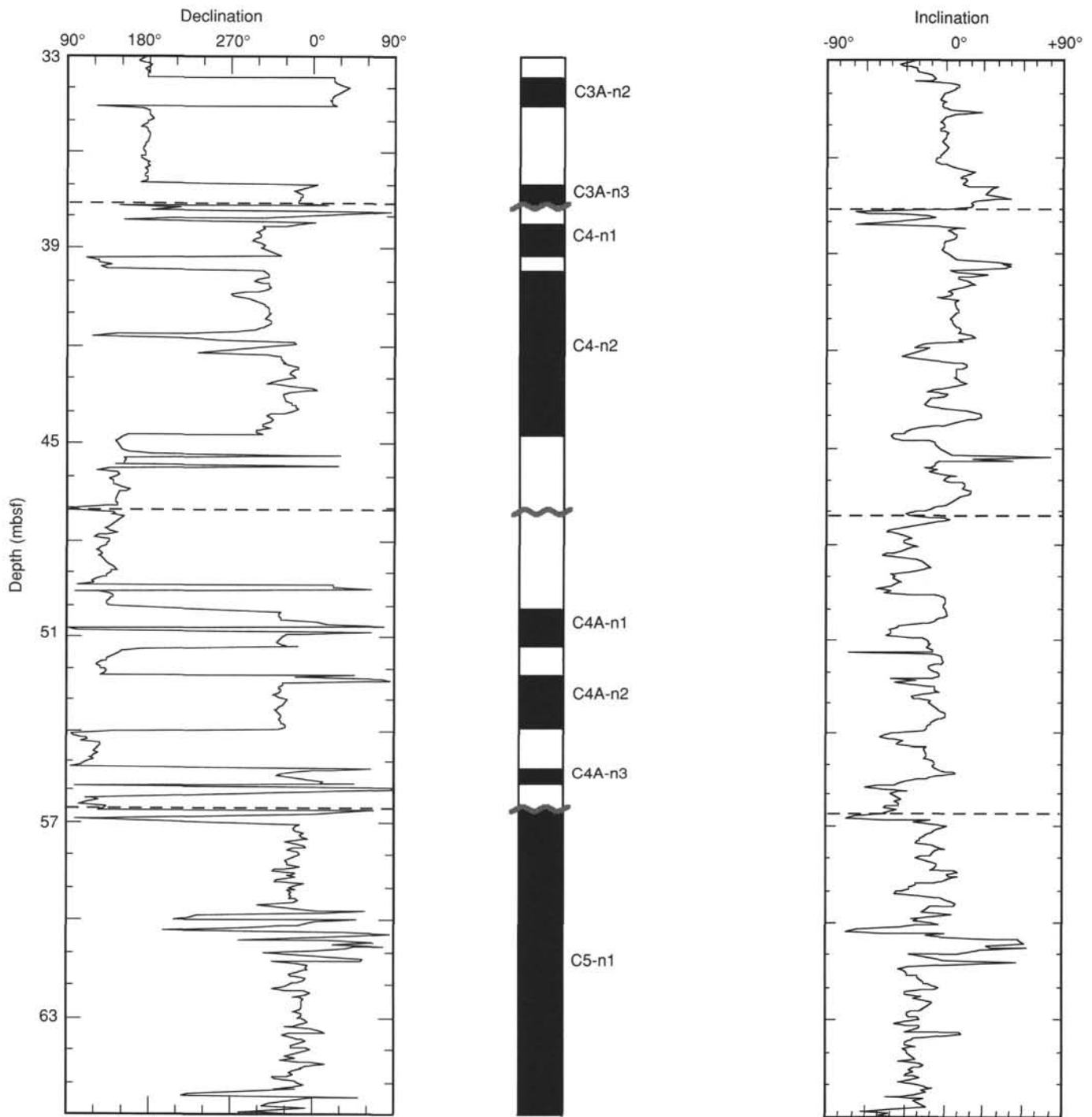
Figure 24. Passthrough magnetometer results (after 15-mT demagnetization) and identification of reversal boundaries from 33 to 66 mbsf in Hole 844C. Black = normal, white = reverse. Declinations are rotated as described in text and Table 9. Dashed lines indicate location of core tops.

Gas Geochemistry

Gas analyses were performed using the headspace technique described in the "Explanatory Notes" chapter (this volume). For this purpose, we took samples in each section of Core 138-844A-1H and in every third core of Hole 844B. As neither methane nor ethane were present in appreciable quantities, we present no data. However, integrated results from several samples yielded traces of butane,

pentane, and hexane, which we suspect are artifacts of either the integration or quantification methods.

In two cores we noted small voids inside the core liners; gas in these voids was extracted into vacutainers that had previously been evacuated using the freeze dryer. The gas was predominantly air, with traces of methane (approximately 200 ppm in Sample 138-844D-1H-1, 95 cm, and 95 ppm in Sample 138-844D-1H-1, 130 cm). Because gas did not occur above or below this interval, we suspect that the

Table 9. Orientations used for Site 844 cores.

Core	Azimuthal orientation (0°–360°)	Deviation from vertical Direction (0°–360°)	Drift (°)
[a]138-844B-			
1H	170		
[a]2H	060		
[a]3H	105		
4H	055	155	3.5
5H	323	135	3.2
6H	258	136	2.4
7H	328	139	2.9
8H	164	154	2.6
9H	026	140	3.0
10H	058	148	2.5
11H	227	135	3.6
12H	337	144	2.9
13H	130	142	2.4
14H	151	142	2.0
15H	186	136	2.0
16H	152	138	1.6
17H	038	146	2.0
18H	357	154	2.0
19H	338	139	1.8
20H	325	137	1.9
21H	No orientation		
[a]138-844C-			
1H	090		
[a]2H	247		
[a]3H	045		
[a]4H	145	170	1.9
[a]4H	330		
5H	072	168	2.1
6H	247	150	2.0
7H	128	170	2.0
8H	092	167	2.3
9H	169	180	2.0
10H	249	155	2.0
11H	036	172	2.2
12H	059	168	2.0
13H	088	177	1.8
14H	249	159	1.9
15H	139	162	1.4
16H	No orientation		
17H	No orientation		
18H	No orientation		
19H	No orientation		

Note: For multishot orientation, declination is corrected by adding to it a multishot azimuthal orientation and the local geomagnetic variation (5.2°).

[a]Secondary orientation (SOR) angle is the value used to adjust average measured declination to 0° or 180° for normal and reverse chronozones respectively, when multishot orientation is not available or is inconsistent. Multishot azimuth values in parentheses are considered erroneous and in our interpretation, we use the SOR value.

occurrence of this methane may have been an artifact, possibly created by drilling.

The absence of biogenic gas production is consistent with results of interstitial-water sulfate analyses (see "Inorganic Geochemistry" section, this chapter); the concentrations of pore water indicate no depletion of sulfate with depth, and alkalinity values remain near the concentration of seawater. In spite of the high biological productivity in this sector of the eastern equatorial Pacific Ocean (Chavez and Barber, 1987), sediments have low concentrations of organic matter, and the sediment/water interface appears to have been well aerated throughout the depositional history at Site 844. The prevailing diagenetic conditions appear to be unfavorable for biogenic methane production. In addition to the aerobic conditions in the sediment, advection of pore waters in the thin sedimen-

tary layer overlying basaltic crust may play a role in inhibiting sulfate reduction and fermentation.

PHYSICAL PROPERTIES

Introduction

Physical properties measured routinely on whole-round sections at Site 844 include GRAPE-density, compressional-wave velocity (using the MST), and thermal conductivity. Vane shear strength and index properties (wet-bulk density, dry-bulk density, water content, porosity, void ratio, and vane shear strength) were measured on discrete samples from split cores. Compressional-wave velocity was determined using the digital sonic velocimeter (DSV). The methods of analyses are described in the "Explanatory Notes" chapter (this volume).

Two discrete physical-property determinations were conducted on each section of the cores from Hole 844B. Cores from Hole 844C were sampled once per section. Index property samples were always taken at the same depth interval as the DSV velocity measurements. Results of the physical properties determined at Site 844 are summarized in Tables 17 through 20 (on CD ROM) and presented graphically in Figures 38 through 44. In this chapter, we describe the downhole distribution of the physical properties from Hole 844B, because two index-property and velocity determinations were performed for each section of the cores from this hole, thus producing the highest resolution data set. Five "physical property" units were defined on the basis of downhole trends in the data at this site.

Index Properties

The distribution of index properties, such as wet-bulk density, water content, grain density, and porosity, have been plotted relative to depth below the seafloor (mbsf) in Figures 38 to 41 and listed in Table 17 (CD ROM). Wet-bulk density (Fig. 38) varies between 1.18 and 1.96 g/cm^3 and generally increases with increasing depth below the seafloor. Physical properties Unit I corresponds to the upper 50 m of sediments, where wet-bulk density increases from about 1.20 to 1.33 g/cm^3. The wet-bulk densities of physical properties Unit II (50–75 mbsf) vary between 1.20 and 1.60 g/cm^3, but most values are less than 1.30 g/cm^3. The upper boundary of physical properties Unit III (75 mbsf) is characterized by a rapid increase of wet-bulk density to values between 1.50 and 1.60 g/cm^3. Wet-bulk density generally increases toward the base of physical property Unit III (171.5 mbsf). In physical properties Unit IV (171.5–187.5 mbsf), wet-bulk densities generally decrease with depth and then increase again toward the base of Hole 844B (290.77 mbsf) in physical properties Unit V.

Water content, expressed relative to dry weight (Fig. 39), varies between 436% and 46%. Physical properties Unit I is characterized by high water content, which decreases with depth. Water contents are highly variable in physical properties Unit II but are higher than the basal portion of the upper unit. The boundary between physical properties Unit II and Unit III is marked by a strong decrease in water content to values around 100%. Water content values remain about 100% throughout physical property Units III and IV. Several depth intervals (101, 208–110, 122, and 126–128 mbsf), however, have significantly higher values, up to 200%. The boundary between physical properties Unit IV and Unit V is marked by a strong decrease in water content.

Grain density (Fig. 40) varies between 2.03 and 2.80 g/cm^3, with most values ranging between 2.50 and 2.70 g/cm^3. Intervals having low grain densities were detected at depths of around 54, 101, 109, 122, 127, 179, 230, and 260 mbsf. These depths also are characterized by high water contents and low wet-bulk densities.

Porosity varies between 91% and 54% (Fig. 41). Because porosity is the volumetric expression for water content, the trends defined for wet-bulk density and water content are similar for porosity.
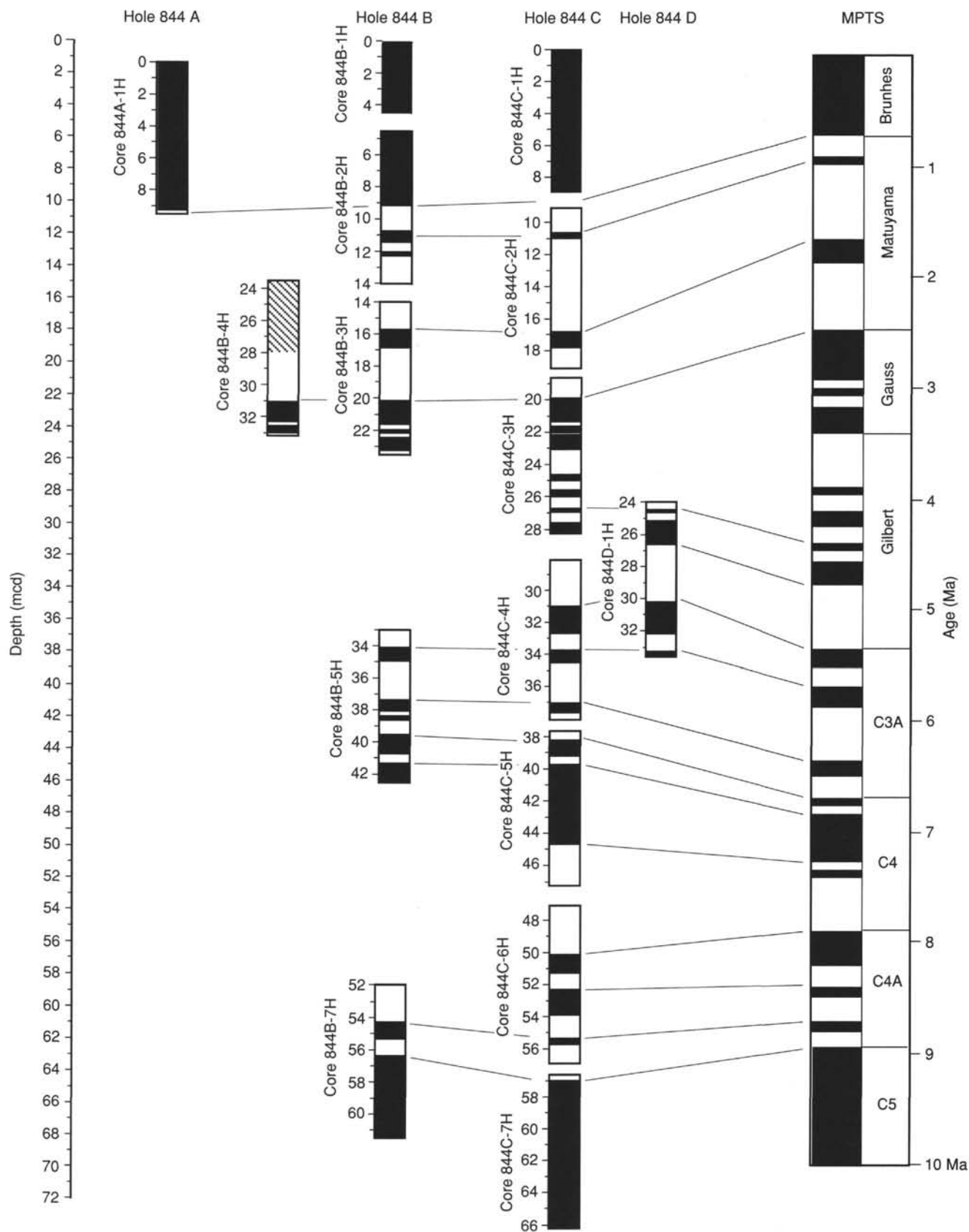
Figure 25. Magnetostratigraphic synthesis. Depth ticks on individual cores in mbsf. Cores are located at appropriate composite depth. Black = zones of normal polarity; white = zones of reversed polarity. Hatched areas = substantial intervals within a core where no interpretation was made.

Table 10. Reversal boundary depths from Site 844.

Core, section interval (cm)	Depth (mbsf)	Depth (mcd)	Interpreted polarity boundary	MPTS Age (Ma)	Comments
138-844B-					
2H-4, 20	9.20	10.33	Brunhes/Matuyama	0.73	
2H-5, 20	10.70	11.83	Jaramillo (t)	0.91	
2H-5, 100	11.50	12.63	Jaramillo (o)	0.98	
2H-6, 30	12.30	13.43	Cobb Mountain (o) (?)	~ 1.1	
3H-2, 20	15.70	17.95	Olduvai (t)	1.66	
3H-2, 135	16.85	19.10	Olduvai (o)	1.88	
3H-5, 15	20.15	22.40	Matuyama/Gauss	2.47	
3H-7, 25	23.25	25.50	Gauss/Gilbert	3.40	
4H-5, 140	30.90	22.35	Matuyama/Gauss	2.47	
4H-7, 0	32.40	23.85	Kaena (t)	2.92	Section break
4H-7, 55	32.50	23.95	Kaena (o)	2.99	
4H-7, 55	33.05	24.50	Mammoth (t)	3.08	
5H-1, 105	34.05	37.70	C3A-n2 (t)	5.68	
5H-2, 50	35.00	38.65	C3A-n2 (o)	5.89	
5H-3, 135	37.35	41.00	C3A-n3 (t)	6.37	
5H-4, 65	38.15	41.80	C3A-n3 (o) (?)	6.50	
5H-4, 90	38.40	42.05	(N->R)		
5H-4, 120	38.70	42.35	C3A-n3 (o) (?)	6.50	
5H-5, 50	39.50	43.15	C4-n1 (t)	6.70	
5H-6, 25	40.75	44.40	C4-n1 (o)	6.78	
5H-6, 80	41.30	44.95	C4-n2 (t)	6.85	
7H-2, 75	54.25	60.95	C4A-n3 (t)	8.71	
7H-3, 30	55.30	62.00	C4A-n3 (o)	8.80	
7H-3, 130	56.30	63.00	C5-n1(t)	8.92	
138-844C-					
2H-2, 0	10.60	11.90	Jaramillo (t)	0.91	Section break
2H-2, 45	11.05	12.35	Jaramillo (o)	0.98	
2H-6, 20	16.80	18.10	Olduvai (t)	1.66	
2H-6, 125	17.85	19.15	Olduvai (o)	1.88	
3H-1, 125	19.85	22.20	Matuyama/Gauss	2.47	Section break
3H-2, 130	21.40	23.75	Kaena(t)	2.92	
3H-2, 150	21.60	23.95	Kaena (o)	2.99	
3H-3, 45	22.05	24.40	Mammoth (t)	3.08	
3H-3, 55	22.15	24.50	Mammoth (o)	3.18	
3H-4, 0	23.10	25.45	Gauss/Gilbert	3.40	
3H-5, 0	24.60	26.95	Cochiti (t)	3.88	
3H-5, 45	25.05	27.40	Cochiti (o)	3.97	
3H-5, 95	25.55	27.90	Nunivak (t)	4.10	
3H-5, 145	26.05	28.40	Nunivak (o)	4.24	
3H-6, 60	26.70	29.05	Sijdfjall (t)	4.40	
3H-6, 90	27.00	29.35	Sijdfjall (o)	4.47	
3H-6, 145	27.55	29.90	Thvera (t)	4.57	
4H-2, 135	30.95	35.10	C3A-n1 (t)	5.35	
4H-4, 10	32.70	36.85	C3A-n1 (o)	5.53	
4H-4, 110	33.70	37.85	C3A-n2 (t)	5.68	
4H-5, 45	34.55	38.70	C3A-n2 (o)	5.89	
4H-6, 140	37.00	41.15	C3A-n3 (t)	6.37	
4H-7, 55	37.65	41.80	C3A-n3 (o)	6.50	
5H-1, 60	38.20	43.45	C4-n1 (t)	6.70	
5H-2, 15	39.25	44.50	C4-n1 (o)	6.78	
5H-2, 60	39.70	44.95	C4-n2 (t)	6.85	
5H-5, 110	44.70	49.95	C4-n2 (o)	7.28	
6H-2, 150	50.10	56.75	C4A-n1 (t)	7.90	Section break
6H-3, 125	51.35	58.00	C4A-n1 (o)	8.21	
6H-4, 65	52.25	58.90	C4A-n2 (t)	8.41	
6H-5, 85	53.95	60.60	C4A-n2 (o)	8.50	
6H-6, 70	55.30	61.95	C4A-n3 (t)	8.71	
5H-5, 115	55.75	62.40	C4A-n3 (o)	8.80	
7H-1, 35	56.95	64.60	C5-n1 (t)	8.92	
138-844D-					
1H-1, 45	24.24	28.94	Sidufjall(t)	4.40	
1H-1, 65	24.65	29.35	Sidufjall(o)	4.47	
1H-1, 120	25.20	29.90	Thvera (t)	4.57	
1H-2, 110	26.60	31.30	Thvera (o)	4.77	
1H-5, 20	30.20	34.90	C3A-n1 (t)	5.35	
1H-6, 75	32.25	36.95	C3A-n1 (o)	5.53	
1H-7, 20	33.20	37.90	C3A-n2 (t)	5.68	

Note: Because of end effects during measurement, reversal boundaries marked as being at section breaks probably are not well located.

Table 11. Depths of top and bottom of each core in Site 844 in the composite depth section.

Core	Depth (mbsf)	Length of core (m)	Depth (mcd)	Delta
138-844A-1H	0–9.94	9.94	1.40–11.34	1.40
138-844B-1H	0–4.53	4.53	0–4.53	0
2H	4.50–14.48	9.98	5.63–15.61	1.13
3H	14.00–24.05	10.05	16.25–26.30	2.25
4H	23.50–33.48	9.98	14.95–24.93	–8.55
5H	33.00–42.90	9.90	36.65–46.55	3.65
6H	42.50–52.52	10.02	46.60–56.62	4.10
7H	52.00–62.06	10.06	58.70–68.76	6.70
8H	61.50–71.46	9.96	68.65–78.61	7.15
9H	71.00–81.10	10.10	79.65–89.75	8.65
10H	80.50–90.27	9.77	91.13–100.90	10.63
11H	90.00–99.99	9.99	103.50–113.49	13.50
12H	99.50–109.59	10.09	113.03–123.12	13.53
13H	109.00–118.95	9.95	122.80–132.75	13.80
14H	118.50–128.26	9.76	133.33–143.09	14.83
15H	128.00–137.82	9.82	143.00–152.82	15.00
16H	137.50–147.43	9.93	153.68–163.61	16.18
17H	147.00–157.07	10.07	162.60–172.67	15.60
18H	156.50–166.43	9.93	173.55–183.48	17.05
19H	166.00–175.83	9.83	183.20–193.03	17.20
20H	175.50–185.58	10.08	194.13–204.21	18.63
21X	185.00–194.69	9.69	203.63–213.32	18.63
22X	194.60–204.27	9.67	213.23–222.90	18.63
23X	204.30–213.90	9.60	222.93–232.53	18.63
24X	213.90–223.65	9.75	232.53–242.28	18.63
25X	223.60–232.04	8.44	242.23–250.67	18.63
26X	233.30–243.06	9.76	251.93–261.69	18.63
27X	242.90–243.30	0.40	261.53–261.93	18.63
28X	252.60–261.66	9.06	271.23–280.29	18.63
29X	261.90–271.75	9.85	280.53–290.38	18.63
30X	271.60–281.47	9.87	290.23–300.10	18.63
31X	281.20–291.25	10.05	299.83–309.88	18.63
138-844C-1H	0–9.10	9.10	0.50–9.60	0.50
2H	9.10–18.62	9.52	10.40–19.92	1.30
3H	18.60–28.66	10.06	20.95–31.01	2.35
4H	28.10–38.18	10.08	32.25–42.33	4.15
5H	37.60–47.56	9.96	42.85–52.81	5.25
6H	47.10–57.20	10.10	53.75–63.85	6.65
7H	56.60–66.73	10.13	64.25–74.38	7.65
8H	66.10–76.30	10.20	75.41–85.61	9.31
9H	75.60–85.78	10.18	85.78–95.96	10.18
10H	85.10–94.92	9.82	96.11–105.93	11.01
11H	94.60–104.66	10.06	106.55–116.61	11.95
12H	104.10–114.15	10.05	116.10–126.15	12.00
13H	113.60–123.62	10.02	126.60–136.62	13.00
14H	123.10–132.71	9.61	138.10–147.71	15.00
15H	132.60–142.80	10.20	147.50–157.70	14.90
16H	142.10–152.16	10.06	157.60–167.66	15.50
17H	151.60–161.50	9.90	168.60–178.50	17.00
18H	161.10–171.19	10.09	178.05–188.14	16.95
19H	170.60–180.80	10.20	189.95–200.15	19.35
138-844D-1H	24.00–34.12	10.12	28.70–38.82	4.70

Table 12. Control points for accumulation rates.

Composite depth (m)	Sed. rate (m/m.y.)	Age (Ma)	Comments
0		0	Top of sedimentary section
	13.6		
12.35		0.91	Base Jaramillo (11.05 mbsf, Hole 844C)
	7.0		
19.15		1.88	Base Olduvai (17.85 mbsf, Hole 844C)
	5.2		
22.20		2.47	Base Matuyama (19.85 mbsf, Hole 844C)
	3.5		
25.45		3.40	Base Gauss (23.10 mbsf, Hole 844C)
	3.6		
29.35		4.47	Base Sijdfjall (27.0 mbsf, Hole 844C)
	6.5		
35.10		5.35	Base Gilbert (30.95 mbsf, Hole 844C)
	6.7		
38.70		5.89	Base C3A-n1 (34.55 mbsf, Hole 844C)
	5.1		
41.15		6.37	Top C3A-n3 (37.00 mbsf, Hole 844C)
	10.1		
56.65		7.90	Top C4A-n1 (50.10 mbsf, Hole 844A)
	7.8		
64.55		8.92	Top C5-n1 (56.95 mbsf, Hole 844A)
	7.4		
75.55		10.40	Bottom core 138-844C-7H, still normal but *Coccolithus miopelagicus* present
	36.6		
189.10		13.50	CN4/CN5, top *Sphenolithus heteromorphus*, Sections 138-844B-19H-4, 65 cm/-19H-5, 65 cm
	27.6		
258.05		16.00	Top *Helicosphaera ampliaporta*, 138-844B-26H-4, 90 cm/-26H-5, 90 cm
	38.7		
308.30		17.30	Bottom of core younger than 17.3 Ma (absence of *Craspedodiscus, coscinodisus* s. st.)

Shear Strength

Shear strength values range from 11.8 to 229 kPa and increase with depth below the seafloor (Fig. 43 and Table 19, CD ROM). Peak shear strength values occur at 70, 72, 108, 109, 127, 128, and 182.5 mbsf. Several of these depth intervals also are characterized by low grain densities and high water contents (e.g., 108–110 and 126–128 mbsf).

Thermal Conductivity

Thermal conductivities vary between 0.61 and 1.31 W/(m • K) (Fig. 44 and Table 20, CD ROM). The profile for thermal conductivity generally mirrors the wet-bulk density profile and is inversely related to water content and porosity.

Relationships of Physical Properties to Lithology

A comparision of physical properties data with lithology reveals that the low wet-bulk densities and high water contents at 50 mbsf correlate with a radiolarian-rich interval and that the high degree of variablity in index properties from 50 to 75 mbsf reflects the interbedded nature of the lithology between a nannofossil ooze and a laminated diatom ooze. The change in lithology to a nannofossil ooze (lithologic Subunit IIB) results in the abrupt increase of wet-bulk density and decrease of water content and porosity at a depth of 75 mbsf. Diatom-rich sections within lithologic Unit II are mirrored by low wet-bulk densities, high water content, and low grain densities.

The downhole distribution of physical properties at Site 844 shows that the variability in physical property data at Site 844 is controlled more by variations in lithology than by gravitational compaction.

Compressional-Wave Velocity

Compressional-wave velocity was measured perpendicular to bedding on split cores from Hole 844B (Fig. 42 and Table 18, CD ROM). Velocities measured at Hole 844B range from 1460 to 1600 m/s and increase with depth. In the upper 50 m of the sedimentary section, compressional-wave velocity decreases with depth. A monotonic increase was observed for the depth interval from 50 to 185 mbsf. A marked decrease in compressional-wave velocity can be seen at 185 mbsf. Below this depth, velocities again increase toward the bottom of the hole at 237 mbsf. The decrease of compressional-wave velocity at 185 mbsf corresponds to the change from APC- to XCB-coring and may result from disturbances of sediment cores during XCB-coring.
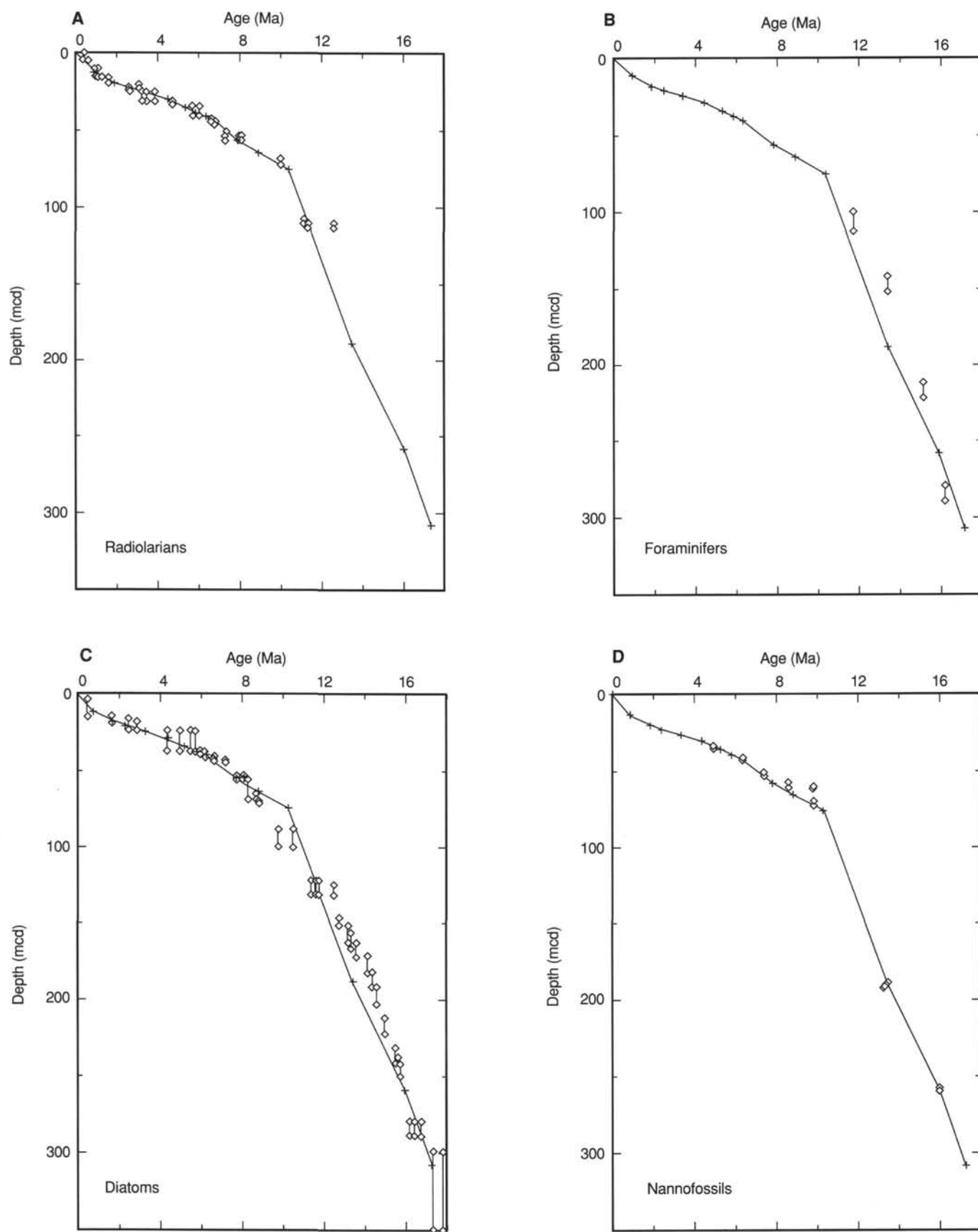
Figure 27. Plot of age vs. depth for Site 844, based upon the calibration points from Table 12 (solid line). **A.** Radiolarians. **B.** Foraminifers. **C.** Diatoms. **D.** Nannofossils. The depth range in which each datum was recognized is indicated by two symbols joined by a line; if the line is not visible, the datums were determined to within size of the symbols.
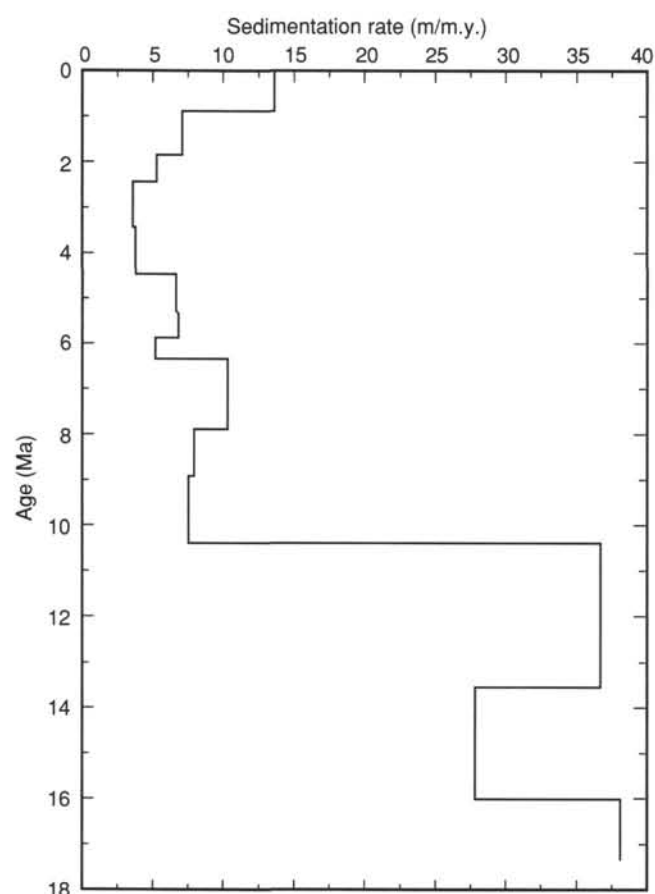
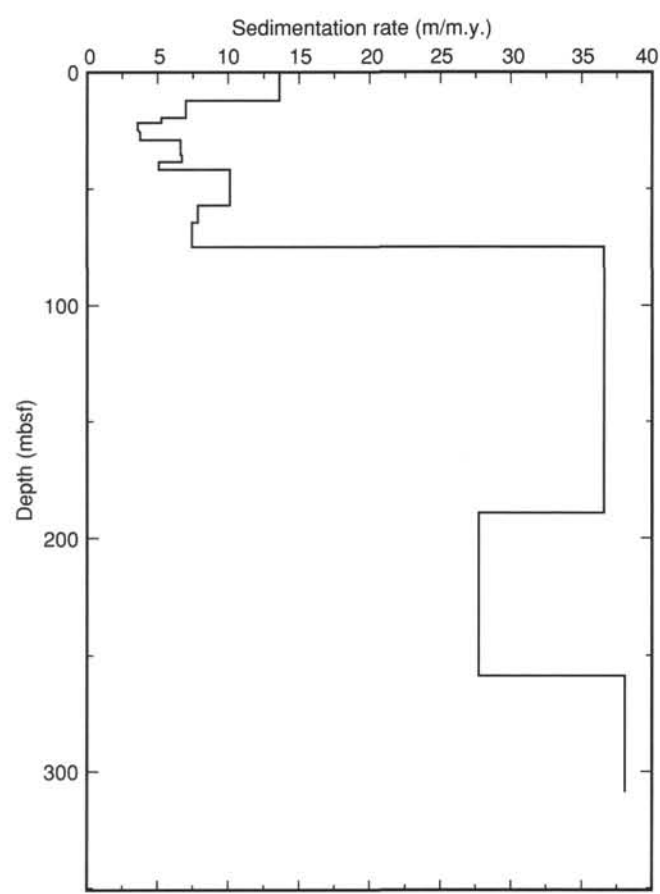Figure 28. Linear sedimentation rate vs. age based on data in Table 12.

Figure 29. Linear sedimentation rate vs. composite depth based on data in Table 12.

Table 13. Interstitial-water geochemical data for Holes 844A and 844B. [a]Measurements were not performed.

| Core, section	Interval (cm)	Depth (mbsf)	pH	Salinity (mM)	Chloride (mM)	Sodium (mM)	Alkalinity (mM)	Sulfate (mM)	Magnesium (mM)	Calcium (mM)	Potassium (mM)	Strontium (μM)	Lithium (μM)	Silica (μM)
138-844A-1H-1	145–150	2.9	7.82	35.5	561	483	2.977	28.83	51.49	10.16	12.8	84.1	28.1	796
1H-2	145–150	4.4	7.71	35.5	559	479	2.966	28.62	52.01	10.12	12.8	87.0	27.4	753
1H-3	145–150	5.9	7.79	35.5	565	484	3.037	28.63	52.18	10.28	12.9	87.0	27.4	728
1H-4	145–150	7.4	7.80	35.0	558	478	3.018	28.73	51.86	10.28	13.3	89.9	27.7	759
1H-5	145–150	8.9	7.79	35.5	556	478	3.045	28.90	51.34	10.23	13.1	87.0	27.7	806
1H-6	145–150	10.4	**	35.5	560	481	**	29.01	51.55	10.18	13.5	87.0	27.4	823
138-844B-6H-4	145–150	42.6	7.72	35.5	555	474	3.072	28.02	52.31	10.22	12.1	95.7	22.3	720
9H-4	145–150	74.6	7.47	35.3	561	479	3.012	28.12	53.08	10.27	11.9	98.6	20.4	829
12H-4	145–150	119.0	7.46	36.0	557	473	2.953	27.28	53.34	10.41	11.3	110	18.2	870
15H-4	145–150	149.0	7.46	35.5	558	475	3.132	27.71	52.52	10.75	11.6	128	15.7	888
18H-4	145–150	179.5	7.75	35.5	557	474	3.003	27.11	52.23	10.79	11.6	139	13.9	917
21X-4	145–150	209.6	7.47	35.8	554	471	3.009	27.32	52.46	10.88	11.0	148	12.4	980
24X-4	142–150	238.5	7.47	36.1	557	473	2.957	26.87	52.65	10.62	11.0	154	11.3	954
25X-4	142–150	248.2	7.55	35.5	554	470	2.834	26.72	52.57	10.62	11.4	148	10.9	863
26X-4	142–150	257.9	7.72	35.8	561	478	2.851	27.08	52.53	10.66	11.0	148	10.9	925
28X-4	142–150	277.2	7.59	35.5	553	470	2.521	27.64	52.63	10.64	11.7	148	11.3	876
29X-4	142–150	286.5	7.58	35.5	557	473	3.016	27.20	52.61	10.66	11.6	142	12.0	851
30X-4	142–150	296.5	7.58	35.8	562	478	2.528	27.35	52.96	10.79	11.4	139	13.5	872
31X-4	142–150	305.8	7.53	35.5	561	478	2.412	27.34	52.66	10.44	11.2	133	13.5	659
31X-7	46–54	309.3	7.72	**	562	484	2.043	27.46	51.36	9.73	10.4	125	21.5	644
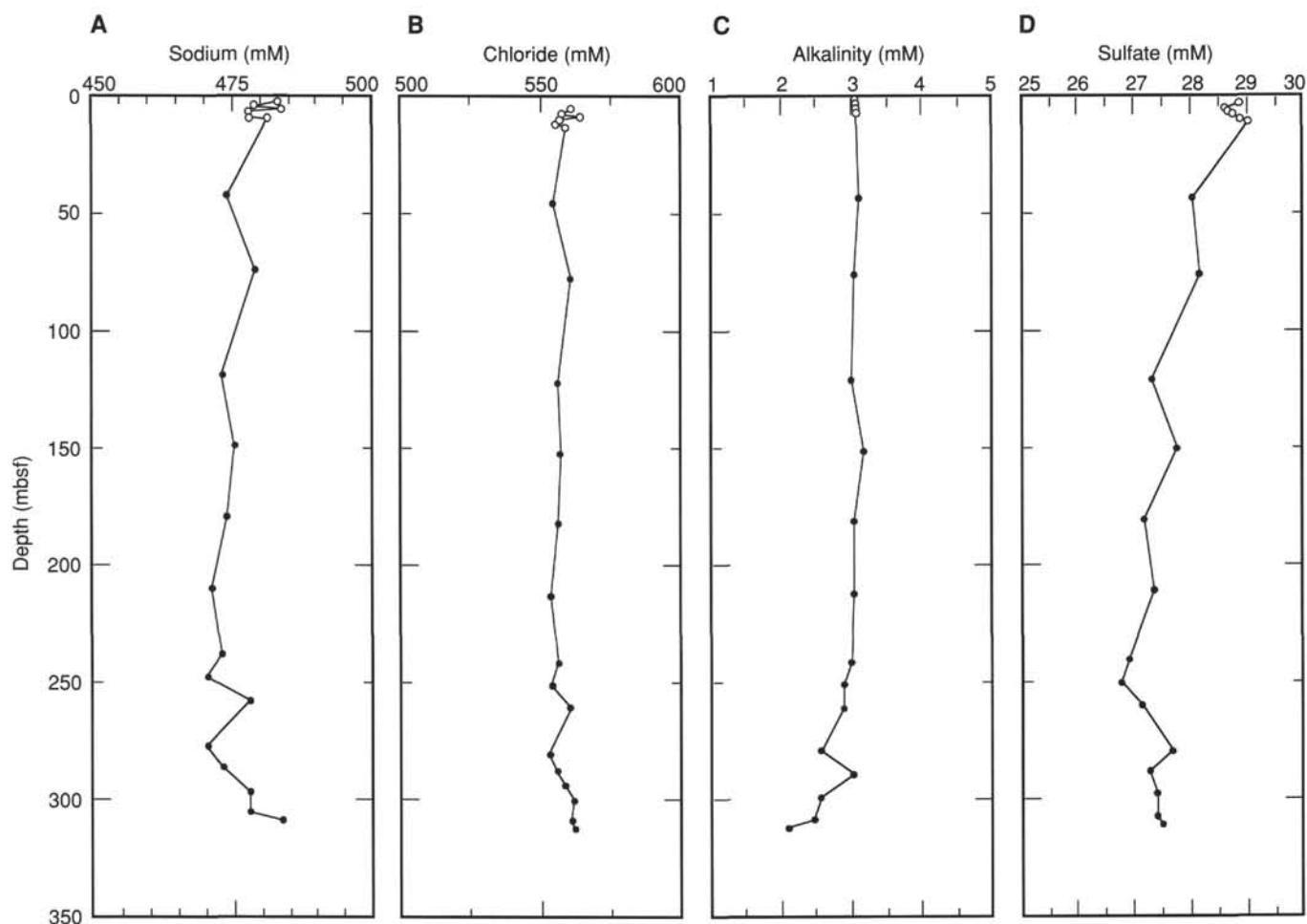
Figure 30. Interstitial-water geochemical data vs. depths (mbsf) for Holes 844A (open circle) and 884B (solid circles). **A.** Sodium. **B.** Chloride. **C.** Alkalinity. **D.** Sulfate.

DOWNHOLE MEASUREMENTS

Data Quality

Table 21 is a list of usable log intervals recorded in Hole 844B. For the most part, these data are of good quality. Logs from the different tool strings had to be shifted with respect to each other to match the natural gamma-ray profiles among runs. We subtracted (i.e., shifted shallower) 1.37 m from the depths recorded for using the geochemical tool string to match depths from the FMS string and subtracted 5.8 m from the GTS to match the FMS string.

By comparing log data with discrete shipboard measurements of physical properties and GRAPE density data, we identified some sections where the density log suffered dropouts, or intervals where the HLDT was displaced from the borehole wall. Bulk density in these intervals is lower than actual *in-situ* values because the borehole water is part of the measured interval. We tied log depths to the ODP mbsf scale in core via a large density gradient at 106.4 mbsf. The largest density dropout is seen between 115 and 118 mbsf, but the interval between 75 and 95 mbsf also may have smaller intervals of poor data.

The FMS data were recorded without the heave compensator and occasionally had unresolvable images because of uncompensated tool accelerations. Nevertheless, most of the log below 170 mbsf is of high quality. Above this depth, the borehole width approached or exceeded the width of the FMS calipers, and we recorded mostly "two-pad" FMS. In a wide hole, this tool tends to ride along one wall while only two of the pads are in contact with the borehole.

Logging Units

High quality logs from all the tool strings were obtained from approximately 75 to about 280 mbsf and were used to divide the section into stratigraphic units. Individual logs extend beyond this depth range and can ultimately provide more stratigraphic information. In particular, using the geochemical tool string, we logged through pipe up to the mud line. Extensive reprocessing will be needed to interpret the chemical log data recorded through pipe from 0 to 40 mbsf; here, we do not discuss the through-pipe geochemical data further.

Log Stratigraphic Unit 1 (Depth, 40–70 mbsf; Age, 6.6–10.5 Ma)

This unit is based solely upon geochemical logging and is recognized by low calcium contents and high natural gamma-ray activity (Fig. 45). High gamma-ray activity normally is indicative of high clay content. Both measurements are consistent with the lithostratigraphic description of the interval (see "Lithostratigraphy" section, this chapter).

Log Stratigraphic Unit 2 (Depth, 70–128 mbsf; Age, 10.5–12.2 Ma)

This unit is a transition between low calcium content, high natural gamma-ray activity sediments to high calcium content, low gamma-ray activity, carbonate-rich sediments. Log Unit 2 also is marked by highly variable physical properties (Figs. 46 and 47). Sonic velocity
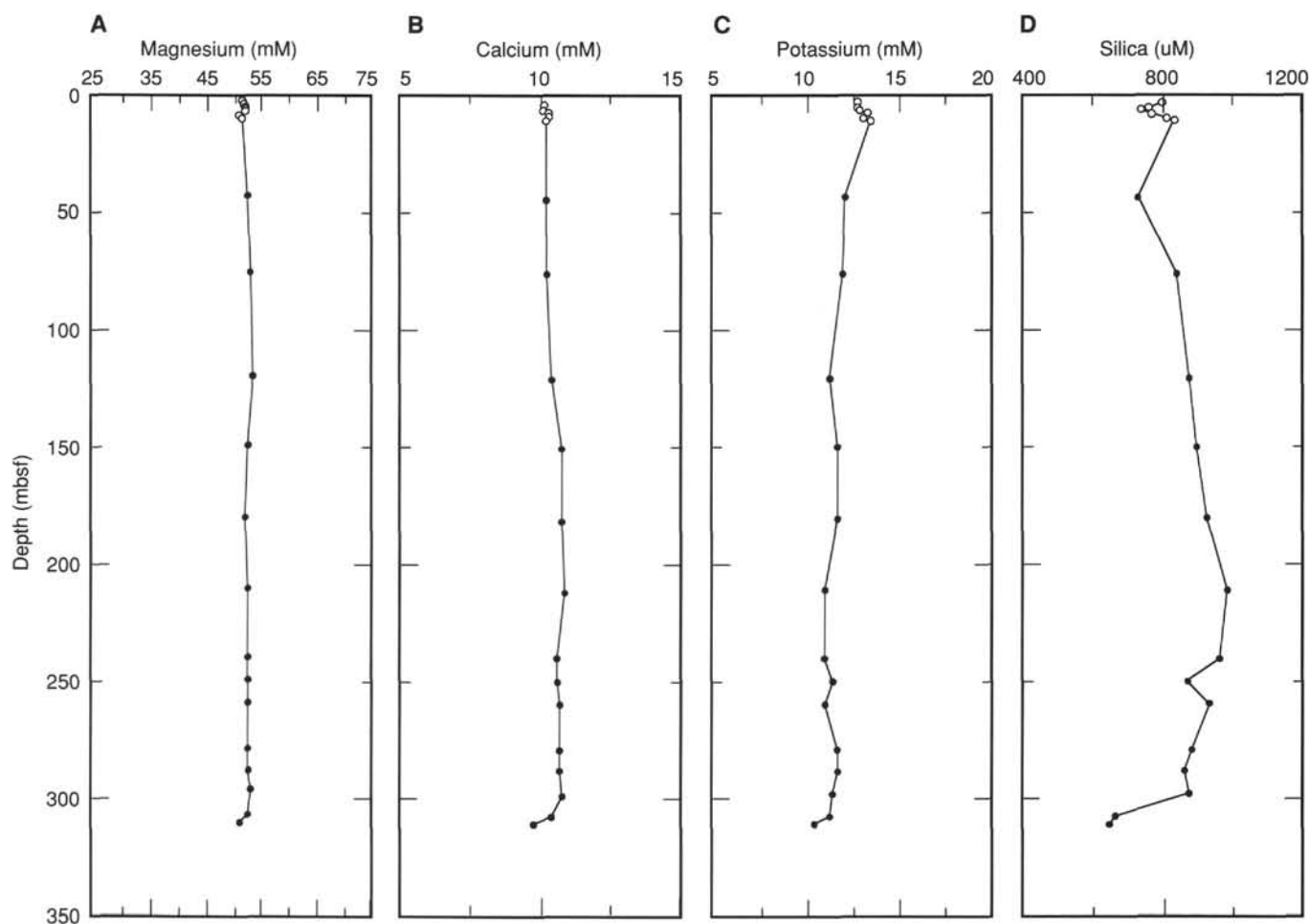
Figure 31. Interstitial-water geochemical data vs. depths (mbsf) for Holes 844A (open circles) and 844B (solid circles). **A.** Magnesium. **B.** Calcium. **C.** Potassium. **D.** Silica.

oscillates between 1.5 and 1.65 km/s, wet-bulk density varies between about 1.35 and 1.65 g/cm³, and resistivity varies between 0.45 and 0.95 ohm-m. All of these variations are coherent.

Log Stratigraphic Unit 3 (Depth, 128–172 mbsf; Age, 12.2–13.6 Ma)

Log Unit 3 has consistently high calcium contents and low natural gamma-ray activity. This unit is marked by ramplike increases in velocity, wet-bulk density, and resistivity, with relatively low amplitude, but high-frequency oscillations about this trend.

Log Stratigraphic Unit 4 (Depth, 172–190 mbsf; Age, 13.6–14.2 Ma)

Log Unit 4 is marked by a decrease in calcium content without a corresponding increase in natural gamma-ray activity. This unit also has higher silicon yields, low velocity, low bulk density, and low resistivity. The interval is probably opal-rich.

Log Stratigraphic Unit 5 (Depth, 190–280 mbsf; Age, 14.2–17.0 Ma)

Log Unit 5 extends from 190 mbsf to the base of the logged interval. This unit is marked by stable physical and chemical logs having moderate amplitude, moderate frequency variations about the mean. Calcium contents are high throughout the unit and also have moderate amplitude variations. Calcium contents and magnitudes of the physical properties measurements also decrease gradually down to 270 mbsf. Below this depth, these values decrease more rapidly.

Comparison of Physical Properties Logs with Core Data

In Figure 48, we show a comparison of GRAPE bulk density measurements from Hole 844B cores with log data from the same interval. The GRAPE data are plotted vs. the composite depth scale formed by splicing overlapping cores from different holes at Site 844 (see "Sedimentation Rates" section, this chapter). The figure emphasizes two important points. First, some offset exists between the GRAPE density measurements and those of the logs. GRAPE density is consistently about 0.08 g/cm³ higher than that measured by the HLDT log. This difference is caused by calibration errors and is not from innate differences between shipboard and *in-situ* measurements. Shipboard density measurements should be slightly lower than log *in-situ* values because the cores should have expanded slightly when retrieved from the seafloor. Nevertheless, trends found in the bulk density log can be found in the GRAPE measurements, even though some type of calibration offset does exist.

The second important point shown in Figure 48 is that the composite depth scale created by splicing different holes into a complete section (see "Sedimentation Rates" section, this chapter) is in fact 9.9% longer than the log record. Detailed comparison of the two records using the inverse signal correlation package CORPAC (Martinson et al., 1982) indicates that the variation downcore is roughly linear. Each small section of the spliced record is approximately 10% longer than the interval from which it came. Because we have no evidence that the cores have been stretched, we do not yet know where the excess material comes from.
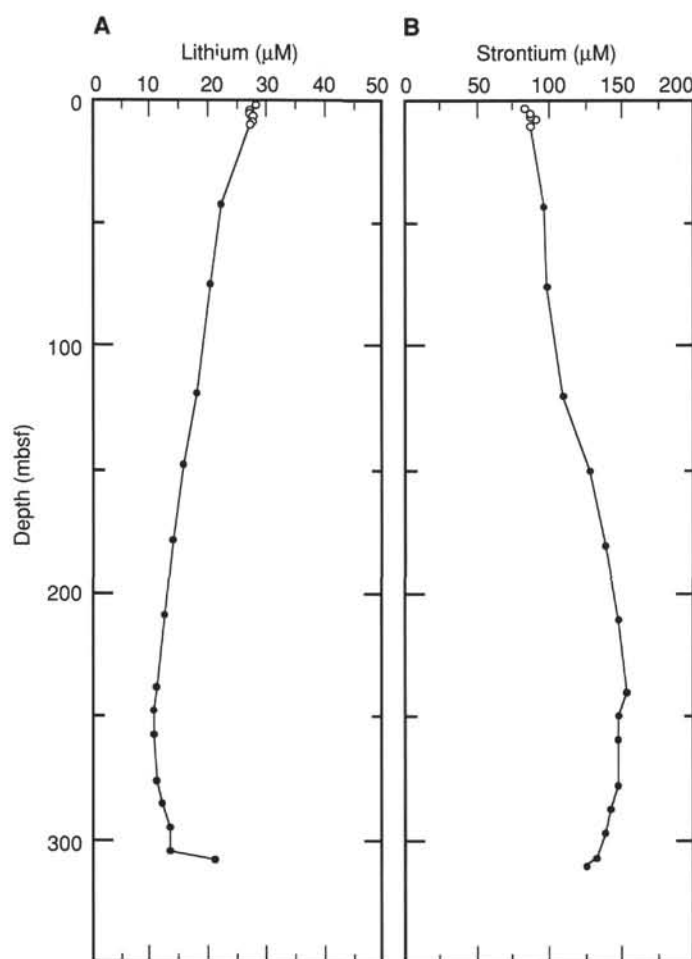
Figure 32. Interstitial-water geochemcial data vs. depths (mbsf) for Holes 844A (open circles) and 844B (solid circles). **A.** Lithium. **B.** Strontium.

Comparison of Laboratory-Measured Density with Logging Data

When discrete gravimetric bulk-density measurements are compared with logging data (Fig. 49), we find that the log and shipboard measurements agree well, with a slight offset between the two data sets. To compare the two, we used CORPAC and the GRAPE data set to get a mapped depth scale between log and core. These gravimetric measurements then were assigned to log-equivalent depths using this map. Figure 49 shows the difference between *in-situ* bulk density measured by logs and shipboard bulk density measured after the cores decompressed. In the interval above 100 mbsf, where the bulk-density log has several possible bad, low density intervals, we observed similar wet-bulk densities between the log and the laboratory measurements. Farther downcore, log densities are consistently greater than laboratory values, showing the effects of decompression of the cores as they came to the sea's surface. Note that the difference between the two bulk density measurements depends on lithology. The largest difference between the two is in log stratigraphic Unit 4, which is probably an opal-rich sediment section.

Comparison of GST Log with Shipboard Calcite Measurements

We also compared the GST log calcium data with the shipboard calcite measurements to determine how useful the calcium logs will be for paleoceanographic reconstructions. Results are shown in Figure 50, a plot

of uncalibrated GST calcium yield vs. shipboard carbonate. We arbitrarily expanded the scale for calcium yield until amplitude was approximately the same for both records. The calcium yield is responding in roughly the same way as shipboard carbonates. For example, the interval between 50 and 59 mbsf is low in carbonate and also has the lowest Ca yield of the record shown, while the interval between 79 and 107 mbsf has both high calcite and a high Ca yield.

The GST Ca yield has a much higher frequency and higher amplitude variation than the shipboard measurements. The frequency difference is most probably the result of the much different sampling frequencies–every 15 cm in the log data vs. at most one or two per section for shipboard calcite. The high amplitude variations of the Ca yield will be attenuated by reprocessing. A strong negative correlation exists between the raw Ca and Cl yields, partly because porosity correlates negatively with calcite content, but also because Cl absorbs neutrons and lowers the number of neutrons that might possibly activate Ca atoms in the calcite.

Mayer (1991) showed that sediment wet-bulk density is a good predictor of calcite content in central and eastern tropical Pacific Ocean sediments. Another way to evaluate the quality of the GST data is to compare the GST Ca yield to the density log (Fig. 51). In the figure, we have performed a linear regression of CA yield to bulk density from the logging data and plotted the data sets on the same scale. This comparison also indicates that the Ca yield is reflecting carbonate variations and that the high-frequency GST Ca signal probably has too high an amplitude. The density-estimated Ca yield appears to be a smoothed version of the GST-measured Ca yield.

Table 15. Duplicate analyses of CaCO$_3$ in samples from Site 844.

Core, section, interval (cm)	ODP depth (mbsf)	Composite depth (mcd)	First run CaCO$_3$ (%)	Second run CaCO$_3$ (%)	Absolute value of CaCO3 (difference)
138-844A-1H-1, 70–72	0.71	2.11	2.33	1.92	0.42
1H-3, 48–49	3.49	4.89	5.08	5.00	0.08
138-844B-2H-1, 46–47	4.97	6.10	19.42	19.67	0.25
2H-7, 25–26	13.76	14.89	5.75	5.92	0.17
3H-5, 101–103	21.02	23.27	6.50	6.75	0.25
3H-6, 39–40	21.90	24.15	0.75	0.17	0.58
5H-7, 65–66	42.66	46.31	40.50	40.25	0.25
7H-4, 70–71	57.21	63.91	0.38	0.33	0.04
10H-3, 145–150	84.98	95.61	82.67	83.84	1.17
12H-6, 65–66	107.66	121.19	56.34	57.34	1.00
12H-7, 65–66	109.16	122.69	24.75	24.92	0.17
14H-4, 100–102	124.01	138.84	90.42	90.13	0.29
Average					0.39

Note: Average difference between the original and duplicate analyses was 0.40% for CaCO$_3$. The average value of the original and the duplicate analyses is reported in Table 14 (CD ROM).

Both comparisons indicate that the GST data are of good quality and, after reprocessing, will provide integrated carbonate measurements over the entire length of Hole 844B. A close examination of the raw Ca yield shows that the carbonate time series has periods of 1.5 to about 4 m. Eventually, these variations can be used to help tune time scales for the hole.

SEISMIC STRATIGRAPHY

Introduction

To better relate the seismic record to stratigraphic changes found in the borehole, we generated synthetic seismograms. Using laboratory and logging density and velocity data, the acoustic impedance (the product of density and velocity) and the reflection coefficient (the rate of change of acoustic impedance) were determined as functions of depth. A reflection coefficient profile represents what a seismic profile should look like with a source of infinite bandwidth. A synthetic seismogram is produced by convolving the water-gun source signature with the reflection coefficient profile. Correlation of a synthetic seismogram with the seismic section can provide insight into the interaction of seismic pulse with geologic structure, which can lead to direct interpretation of a seismic record in terms of stratigraphic change.

However, stratigraphic correlation of a seismic record suffers from two problems. First, seismic events are presented as a function of traveltime, not depth. Second, seismic systems have a limited bandwidth; thus, one cannot realize resolution on the scale of the true geological variability. Consequently, seismic reflectors are often interference composites resulting from the interaction of the true geological structure and the outgoing pulse of the seismic system (Mayer, 1979). Both problems are important in the eastern equatorial Pacific Ocean, where subtle changes in physical properties resulting from paleoceanographic change result in a seismic section having many closely spaced reflectors. Thus, interference must be active in producing seismic reflectors, and given the close spacing of the reflectors, inaccuracies in traveltime-to-depth conversion would result in miscorrelation of a reflector with a geological event. Therefore, to convert a seismic section into a depth section, an accurate sonic velocity model is required.

Modeling Procedure

A density model was created by merging laboratory density to *in-situ* log density. Log density was used from 76.8 to 278.3 m (logging depths). Log density was depth-shifted to meters below seafloor by correlation with the GRAPE density over the interval 76.8 to 183.4 m (78.1–183.2 mbsf) (see "Logging" section, this chapter). From 183.2 to 278.1 mbsf, the log depth was shifted by –0.2 m, an amount equal to the difference in laboratory and log depths of the final log density. Dropouts in the log values were eliminated between 88.4 and 91.9 and 117.1 to 122.0 m. Over the intervals 0 to 78.1 and 279.6 to 290.8 mbsf, a 10-point-boxcar filtered GRAPE density and laboratory wet-bulk density, respectively, were merged with the depth-shifted log density.

A velocity model was created in a similar manner as above. From 78.9 to 268.8 mbsf, we used a depth-shifted log velocity, with data from intervals having had dropouts eliminated. To fill the gap in the upper part of the section, laboratory velocities collected with the digital sonic velocimeter (DSV) were corrected to *in-situ* conditions for changes of sound speed as a function of temperature and pressure. From 268.8 to 290.0 mbsf, we used a constant velocity equal to the final log velocity (1710 m/s).

The accuracy of the traveltime-to-depth conversion can be evaluated by the generation of synthetic seismograms and subsequent comparison to the seismic record collected over the site. Synthetic seismograms were generated using the above merged velocity and density data. These data were resampled at a 1-ms sample interval (approximately 60 cm) and then used to calculate acoustic impedance and reflection coefficients and, finally, a synthetic seismogram. Density and velocity values typical of basalt (2.5 g/cm^3 and 3000 m/s, respectively) were added at the basement depth (291 mbsf) to generate a basement reflector in the synthetic seismogram. The model we used to generate this synthetic seismogram assumes plane waves, no multiples, and no signal attenuation; this model is described in Mayer et al. (1985). The final synthetic seismogram was filtered from 70 to 250 Hz, the same filter parameters as the field record collected during the site-survey cruise aboard the *Thomas Washington*.

Results

A comparison of the synthetic seismogram with the seismic profile collected at Site 844 shows a good match between the two (Fig. 52). A nearly one-to-one correspondence exists between reflectors, with an excellent match at basement. This suggests that the traveltime-to-depth conversion is fairly accurate.

Given an acceptable velocity model, the origin of some of the reflectors at Site 844 can be analyzed. We emphasize that these are preliminary results that will undoubtedly be modified after more careful analyses. Seventeen major reflectors or reflector packages were identified. These reflectors were selected on the basis of amplitude and lateral coherency in the seismic record in the immediate area
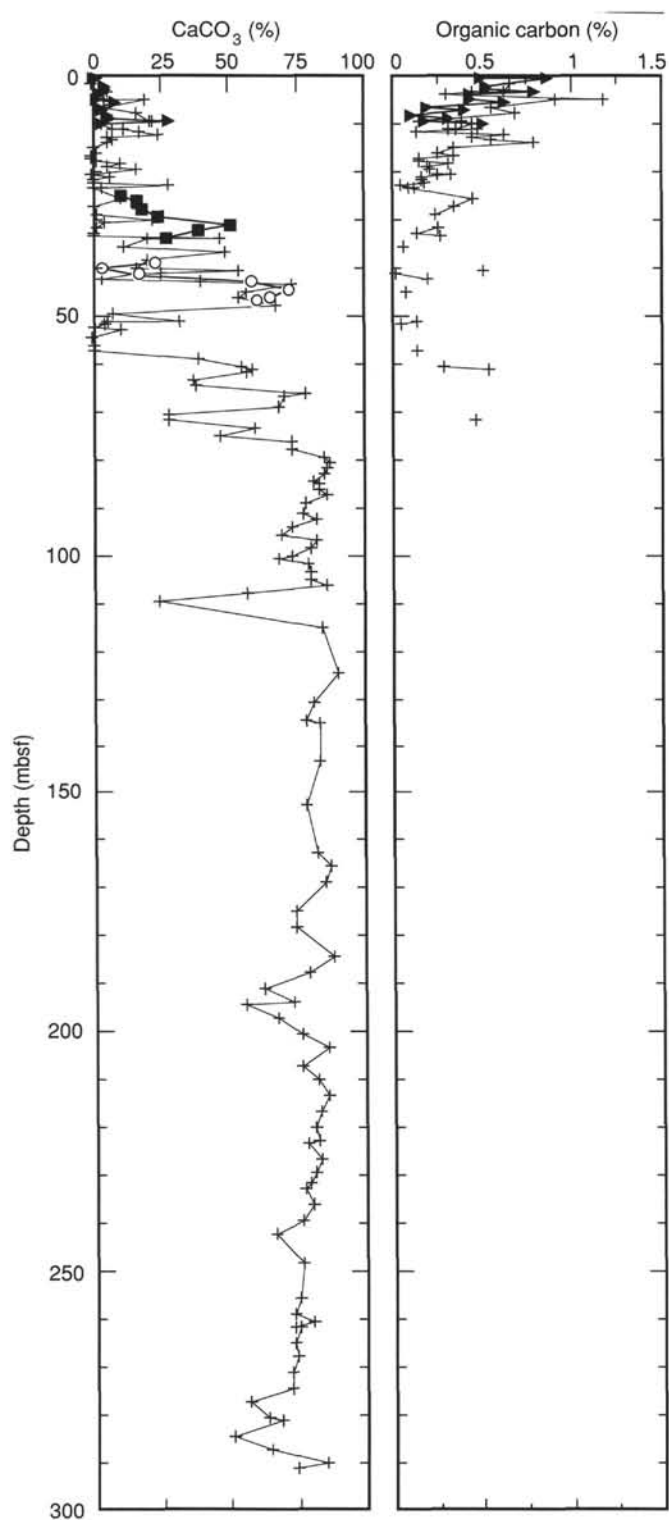
Figure 33. Records of percentages of CaCO$_3$ and C$_{org}$ vs. ODP depth for Holes 844A (triangles), 844B (crosses), 844C (circles), and 844D (squares).

of Site 844. We measured the two-way traveltime in the synthetic seismogram of the top and bottom of each reflector, and by using the assumed velocity model, we determined the depth range of each reflector.

With each major reflector, an associated change in acoustic impedance occurred. Sometimes, a large reflector can result from the constructive interference of several small impedance contrasts, but, for the most part, significant changes in acoustic impedance are the cause of major reflectors. We compared the velocity, density, and acoustic impedance models to the depth ranges calculated from the traveltime to determine any changes in physical properties causing these selected seismic reflectors.

In general, within 1 m of each calculated depth range, a large variation in density and/or velocity may be associated with each reflector (Fig. 53). Reflectors for the upper 100 m (synthetic depth; reflectors 0 through 5) are related solely to large changes in density. Beyond 100 m (synthetic depth), the reflectors are the result of synchronous, large fluctuations in velocity and density. The depths (synthetic, mbsf, and mcd) and ages (based on magnetostratigraphy and biostratigraphy of Site 844; see "Sedimentation Rates" section, this chapter) of these reflectors are presented in Table 22. A detailed understanding of the lithologic, biostratigraphic, and, ultimately, the paleoceanographic significance of these events must await shore-based studies at this time.

SUMMARY AND CONCLUSIONS

Double (and where necessary, triple) APC-coring, in conjunction with real-time analyses of continuous core logs (GRAPE, susceptibility, and color) assured our recovery of a continuous record of sedimentation at Site 844 that spanned the last 17.3 Ma. The sedimentary section recovered at this site records the complex interplay among the divergence-driven equatorial current system, the shoaling of the thermocline associated with the Costa Rica Dome, terrigenous influx, tectonic plate movements, and ocean chemistry. While a detailed reconstruction of these complex interactions must await shore-based studies, we present here a brief preliminary geologic history of Site 844 based on our initial shipboard results.

Site 844 is located on the Cocos Plate on crust formed about 17.5 Ma at the East Pacific Rise. Backtracking the site using the absolute plate motion for the Cocos Plate showed that the site formed at about 2° north of the equator. Based on present-day oceanographic boundaries, this should place the nascent Site 844 beneath the South Equatorial Current (SEC). The first sediment to accumulate at the site was a metalliferous diatom nannofossil ooze, a product of the productive waters of the SEC and hydrothermal emanations associated with rifting. Following this initial phase of sedimentation, calcareous sediments, mostly foraminfer nannofossil oozes, accumulated at rates as high as 35 m/m.y. during the early to middle Miocene. Siliceous sedimentation also was important during this interval, with radiolarians and, especially, diatoms increasing in abundance through the middle Miocene. Sedimentation rates of 30 to 35 m/m.y. are typical of those of the divergence-driven system of today's eastern equatorial Pacific Ocean.

At about 10.4 Ma, sedimentation rates rapidly decreased to about 10 m/m.y., with lithology characterized by alternating carbonate and siliceous clay-rich oozes. The paleolatitude of the site at this time was about 4°N; assuming present current circulation patterns, this should place the site near the northern edge of the present SEC and into a
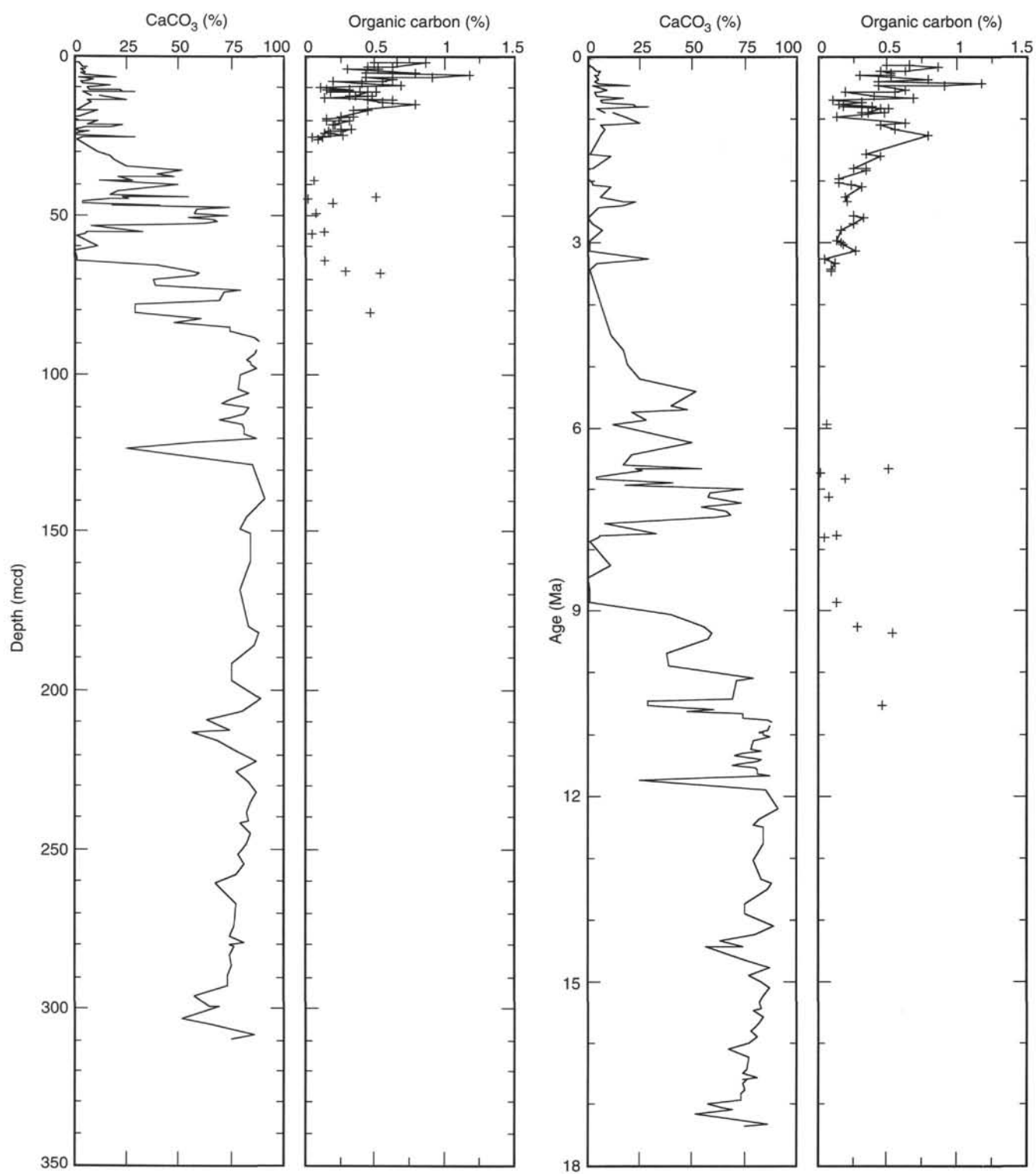
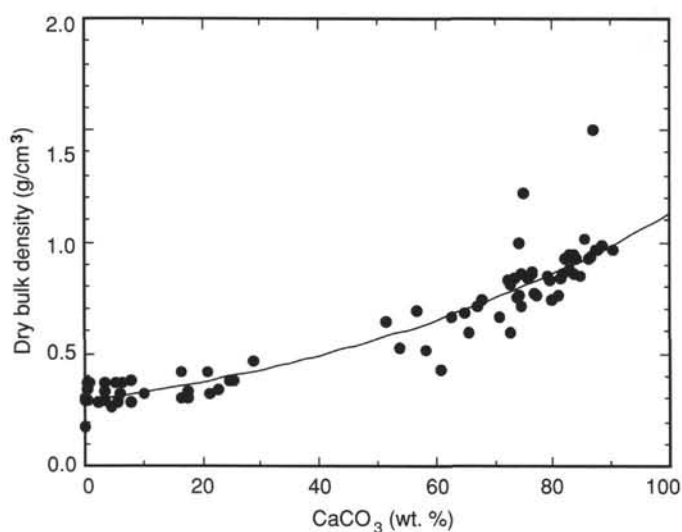Figure 34. Records of percentages of CaCO$_3$ and C$_{org}$ vs. composite depth (mcd) and age (Ma from Site 844.

Figure 35. Relationship between percentage of CaCO$_3$ and dry-bulk density (DBD) at Site 844 used to estimate DBD in samples for which DBD has not been determined. Equation is given in text.

region presently characterized by relatively low sedimentation rates. While the reduction of sediment accumulation at this time may, in part, result from the location of the site relative to surface circulation patterns, evidence exists to indicate that this reduction may be related to a major reorganization of oceanic circulation.

Large variations in carbonate sedimentation have been observed near the middle/late Miocene boundary at a number of sites around the

Pacific Ocean (in the central equatorial Pacific, Mayer, Theyer, et al., 1985; on Hess Rise, the mid-Chron 10 event, Vincent, 1981; in the Southern Ocean, Barker, Kennett, et al., 1990). Widespread formation of hiatuses (Barron and Keller, 1982), an increase in provincialism between high- and low-latitude microfossil assemblages (Bukry, 1985), and a rapid change in the "eustatic sea level" curve of Haq et al. (1987) also characterized this time period. These events, expressed as a widespread, synchronous seismic event first mapped in the central equatorial Pacific (Mayer et al., 1986) and subsequently found in the western equatorial Pacific (Berger et al., in press) and now at Site 844, are evidence of a significant change in the characteristics of Pacific Ocean bottom waters. Coincident with this restructuring of Pacific Ocean bottom water is the occurrence of major erosional events in the deep North Atlantic Ocean (Mountain and Tucholke, 1983; Tucholke and Laine, 1982). The intensification of North Atlantic Deep Water (NADW) associated with these erosional events may have resulted in increased partitioning of silica and carbonate between the Atlantic and Pacific oceans and may have accounted for the major changes in the Pacific Ocean carbonate record at this time (Mayer et al., 1986). Detailed shore-based study should help to resolve the causes and effects of this far-reaching oceanographic event.

Sedimentation during the late Miocene and Pliocene is characterized by a continuation of alternating calcareous and siliceous lithologies, with sedimentation rates relatively low (less than 10 m/m.y.), as compared with that during the early to middle Miocene. Siliceous microfossils, especially diatoms, suggest that surface production during this interval was elevated, as compared to the open tropical Pacific Ocean. Radiolarian assemblages exhibit significant differences from tropical sites of the same age, again suggesting a different oceanographic environment at the site.

During the late Pliocene, sedimentation rates increase, probably the result of an increase in noncarbonate biogenic accumula-

Table 16. Average values of sedimentary parameters measured or calculated over time intervals defined by chronostratigraphic levels. See "Sedimentation Rates" section (this chapter) for a discussion.

Composite depth (mcd)	Age (Ma)	Mean CaCO$_3$ (%)	Mean C$_{org}$ (%)	Mean sed. rate (m/m.y.)	Mean DBD (g/cm^3)	Mean bulk MAR (g/cm^2-k.y.)	Mean CaCO$_3$ MAR (g/cm^2-k.y.)	Mean non-CaCO$_3$ MAR (g/cm^2-k.y.)	Mean C$_{org}$ MAR (mg/cm^2-k.y.)
0.00	0.00								
		7.60	0.50	13.57	0.32	0.43	0.04	0.40	2.16
12.35	0.91								
		7.57	0.44	7.01	0.32	0.22	0.02	0.20	0.97
19.15	1.88								
		8.96	0.22	5.17	0.32	0.16	0.02	0.15	0.35
22.20	2.47								
		4.33	0.20	3.49	0.30	0.11	0.01	0.10	0.21
25.45	3.40								
		0.71	0.10	3.64	0.29	0.10	0.00	0.10	0.10
29.35	4.47								
		17.67		6.53	0.36	0.24	0.04	0.20	
35.10	5.35								
		37.15		6.67	0.48	0.32	0.12	0.19	
38.70	5.89								
		30.42	0.07	5.10	0.45	0.27	0.10	0.17	0.12
41.15	6.37								
		34.07	0.17	10.13	0.48	0.49	0.21	0.28	0.83
56.65	7.90								
		3.03	0.15	7.75	0.30	0.23	0.01	0.22	0.32
64.55	8.92								
		54.49	0.42	7.43	0.62	0.47	0.27	0.20	1.98
75.55	10.40								
		75.00	0.47	35.63	0.80	2.85	2.20	0.65	7.02
186.00	13.50								
		78.09		28.82	0.84	2.44	1.93	0.52	
258.05	16.00								
		71.11		38.65	0.76	2.95	2.12	0.83	
308.30	17.30								

Note: After this table was constructed on board the ship, changes were made to depths of the age control points (see "Sedimentation Rates" section, this chapter, for final selection of age control points). These depth changes are often minor (less than 5 m). None of these changes have been incorporated here nor in the accompanying Figures 36 and 37.
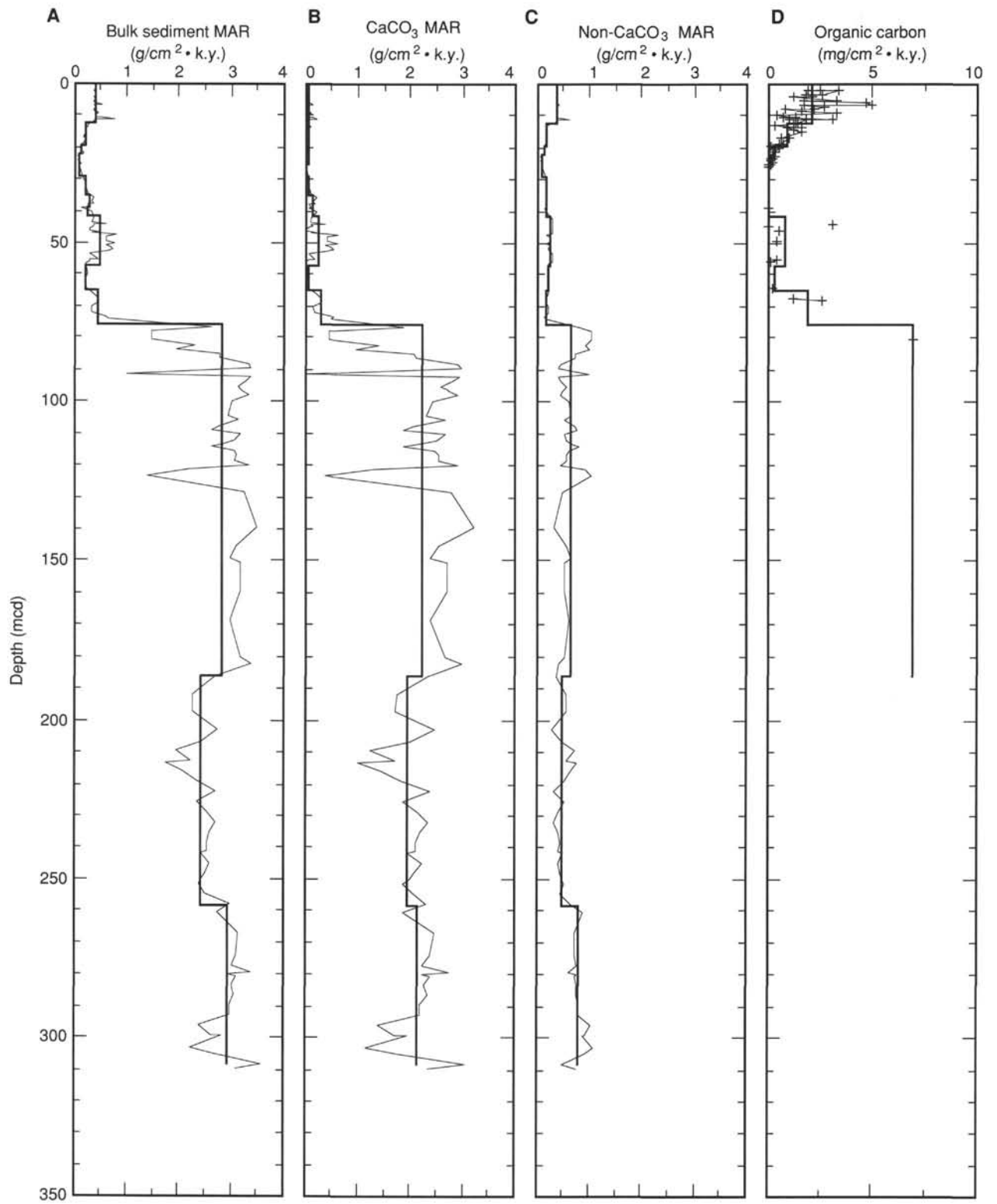DBD = dry-bulk density; MAR = mass accumulation rate.

Figure 36. Accumulation rates of bulk sediment (**A**), CaCO$_3$ (**B**), non-CaCO$_3$ (**C**), and C$_{org}$ (**D**) sedimentary components vs. composite depth at Site 844. Note different units for C$_{org}$. Thick line = mean value between each stratigraphic datum plane; thin line = discrete accumulation rates calculated for each sample.
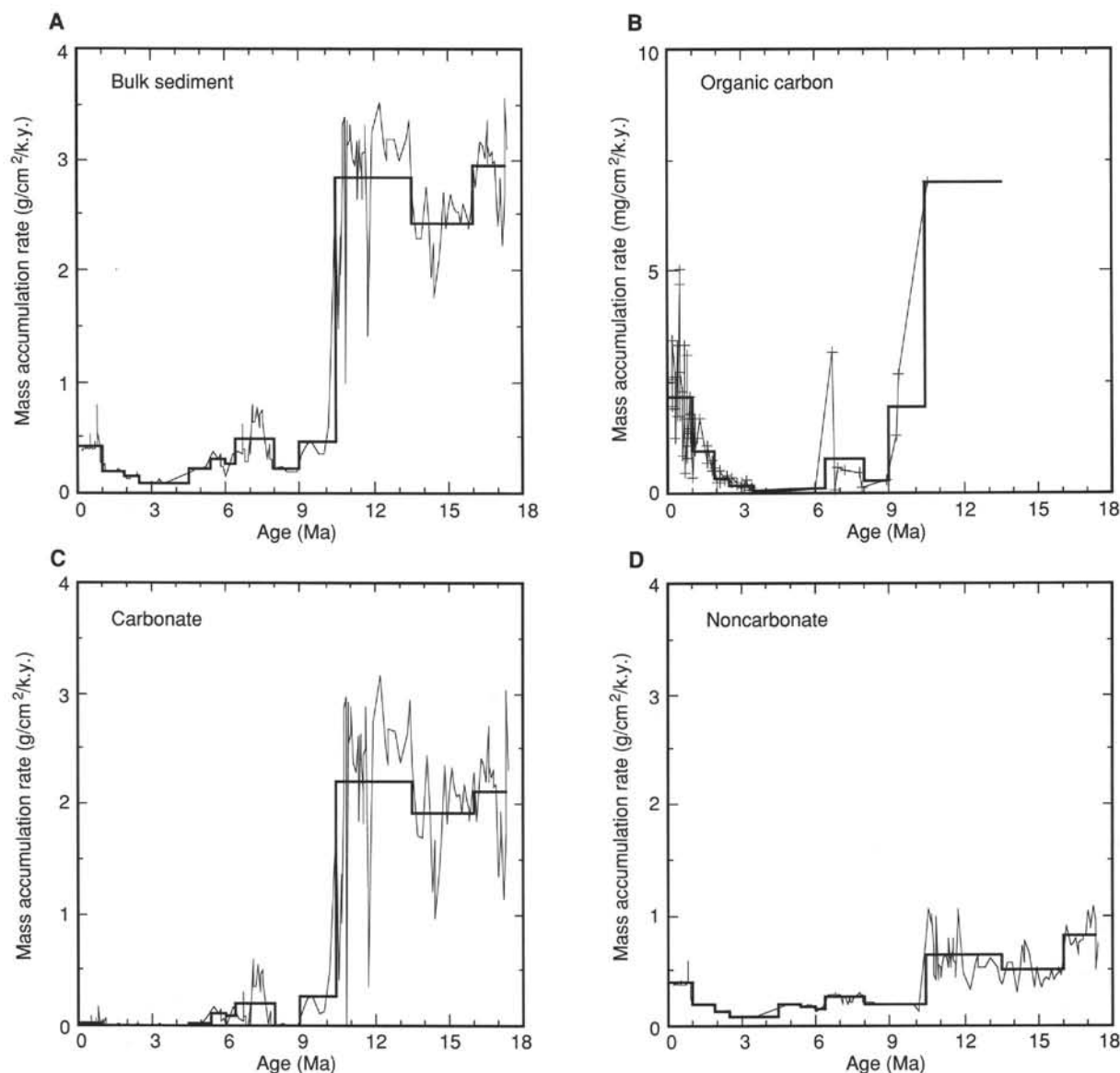
Figure 37. Accumulation rates of bulk sediment (**A**), C_{org} (**B**), $CaCO_3$ (**C**), and non-$CaCO_3$ (**D**) vs. age in sediments from Site 844. Thick line = mean value between each stratigraphic datum plane; thin line = discrete accumulation rates calculated for each sample.

tion. The paleolatitude of the site at this time (Table 23) is within 1° of its present position within the high productivity zone associated with the Costa Rica Dome. While increased sedimentation resulting from the enhanced ocean production associated with the Costa Rica Dome was expected in the Pleistocene, the depth of the site precludes accumulation of calcium carbonate and thus sedimentation rates in the youngest part of the section do not reach the levels found in the Miocene section, nor those presently found in areas of the eastern equatorial Pacific Ocean where carbonate has been accumulating.

Superimposed on these long-term trends in sedimentation is a high degree of variability, as demonstrated in the continuous sediment parameters collected by color reflectance, GRAPE density, and magnetic susceptibility. This variability occurs on scales from centimeters to meters; further high-resolution studies will be necessary to determine the processes responsible for this variability. For example, we are still unable to determine if the high-frequency variability in carbonate sedimentation during the Miocene reflects changes in production and/or changes in preservation (processes that are not necessarily uncoupled in pelagic sediments), or whether this variabil-

ity is related to external climate forcing, such as that observed in the Pleistocene climate's response to orbital variations.

REFERENCES

Backman, J., Schneider, D. A., Rio, D., and Okada, H., 1990. Neogene low-latitude magnetostratigraphy from Site 710 and revised age estimates of Miocene nannofossil events. *In* Duncan, R. A., Backman, J., Peterson, L. C., et al., *Proc. ODP, Sci. Results,* 115: College Station, TX (Ocean Drilling Program), 271–276.

Barker, P. F., Kennett, J. P. et al., 1990. *Proc. ODP, Sci. Results,* 113: College Station, TX (Ocean Drilling Program).

Barron, J. A., 1985. Late Eocene to Holocene diatom biostratigraphy of the equatorial Pacific Ocean, Deep Sea Drilling Project Leg 85. *In* Mayer, L., Theyer, F., Thomas, E., et al., Init. Repts. DSDP, 85: (U.S. Govt. Printing Office), 413–456.

Barron, J. A., and Keller, G., 1982. Widespread Miocene deep-sea hiatuses: coincidence with periods of global cooling. *Geology,* 10:557–581.

Berger, W. H., Kroenke, L. W., Mayer, L. A., Backman, J., Janecek, T. R., Krusek, L., Leckie, M., Lyle, M., Mahoney, J., and the Shipboard Scientific Party, in press. The record of Ontong Java Plateau: main results of ODP Leg 130. *Geol. Soc. Am. Bull.*
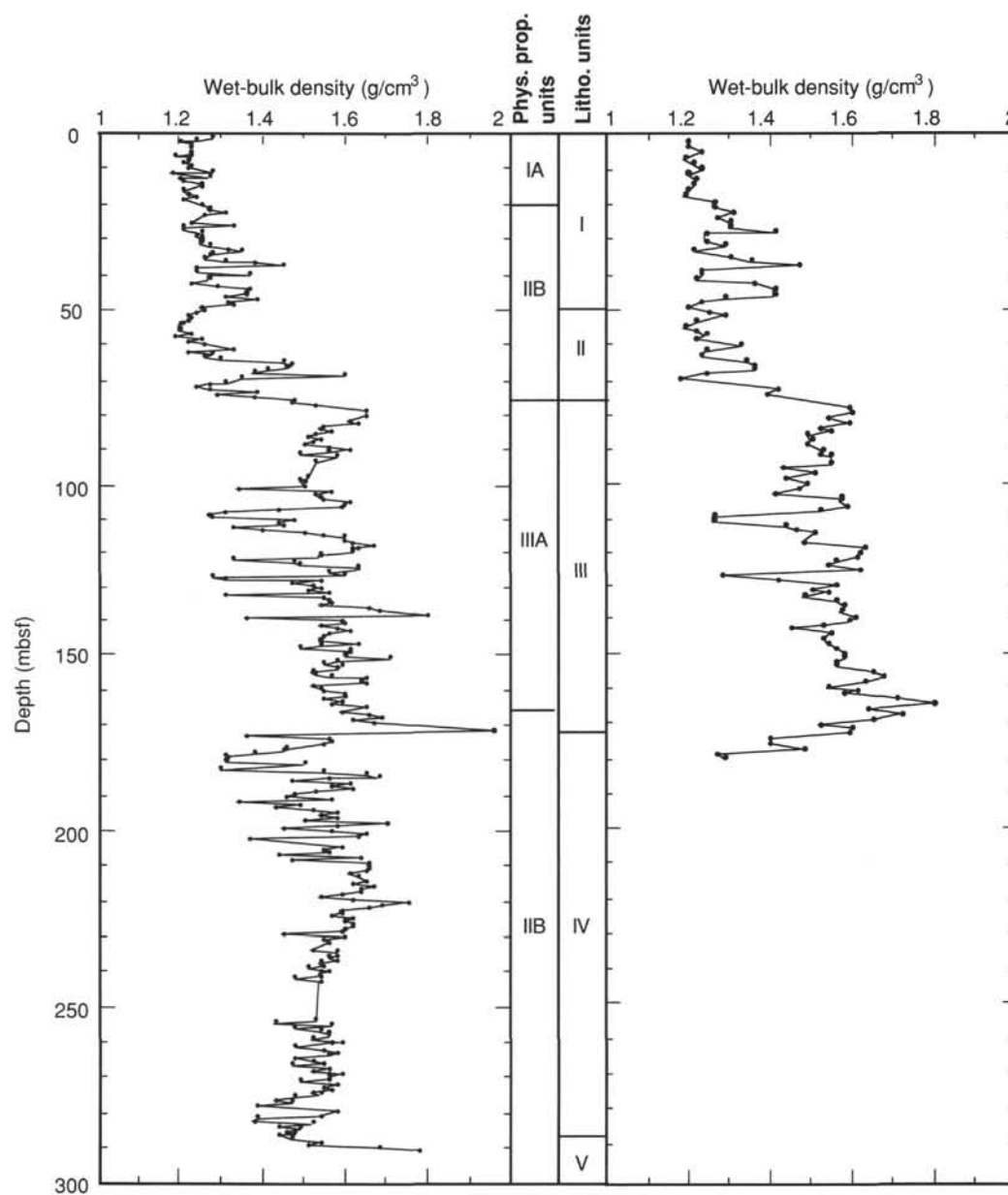
Figure 38. Wet-bulk density vs. depth, Holes 844B (left) and 844C (right). Lithologic and physical property units are shown for comparison.

Bukry, D., 1985. Tropical Pacific silicoflagellate zonation and paleotemperature trends in the late Cenozoic. *In* Mayer, L. A., and Theyer, F., et al., 1985. *Init. Repts. DSDP*, 85: Washington (U.S. Govt. Printing Office), 477–498.

Chavez, F. P., and Barber, R. T., 1987. An estimate of new production in the equatorial Pacific. *Deep Sea Res. Part A*, 34:1229–1243.

Elderfield, H., and Gieskes, J. M., 1982. Sr isotopes in interstitial waters of marine sediments from Deep Sea Drilling Project cores. *Nature*, 333:493–497.

Gieskes, J. M., 1974. Chemistry of interstitial waters of marine sediments. Annu. Rev. Earth Planet. Sci., 3:433–394.

Harrison, W. E., Hesse, R., and Gieskes, J. M., 1982. Relationship between sedimentary facies and interstitial water chemistry of slope, trench, and Cocos Plate sites from the Middle America Trench transect, active margin off Guatemala, Deep Sea Drilling Project Leg 67. *In* Aubouin, J., von Huene, R., et al., *Init. Repts. DSDP*, 67: Washington (U.S. Govt. Printing Office), 603–613.

Haq, B. U., Hardenbol, J., and Vail, P. R., 1987. Chronology of fluctuating sea levels since the Triassic. *Science*, 235:1156–1167.

Hey, R., Johnson, G. L., and Lowrie, A., 1977. Recent plate motions in the Galapagos area. *Geol. Soc. Am. Bull.*, 88:1385–1403.

Hofmann, E. E., Busalacchi, A. J., and O'Brien, J. J., 1981. Wind generation of the Costa Rica Dome. *Science*, 214:552–554.

Martini, E., 1971. Standard Tertiary and Quaternary calcareous nannoplankton zonation. *In* Farinacci, A. (Ed.), *Proc. 2nd Planktonic Conf. Roma*: Rome (Ed. Tecnosci), 739–785.

Martinson, D. G., Menke, W., and Stoffa, P., 1982. An inverse approach to signal correlation. *J. Geophys. Res.*, 87:4807–4818.

Mayer, L. A., 1979. The origin of fine scale acoustic stratigraphy in deep-sea carbonates. *J. Geophys. Res.*, 84:6177–6184.

————, 1991. Extraction of high-resolution carbonate data fro paleoclimate reconstruction. *Nature*, 352:148–151.

Mayer, L. A., Shipley, T. H., Theyer, F., Wilkens, R. W., and Winterer, E. L., 1985. Seismic modelling and paleoceanography at DSDP Site 574. *In* Mayer, L. A., Theyer, F., Thomas, E., et al., *Init. Repts. DSDP*, 85 Washington (U.S. Govt. Printing Office), 947–970.

Mayer, L. A., Shipley, T., and Winterer, E. L., 1986. Equatorial Pacific seismic reflectors as indicators of global oceanographic events. *Science* 233:761–764.
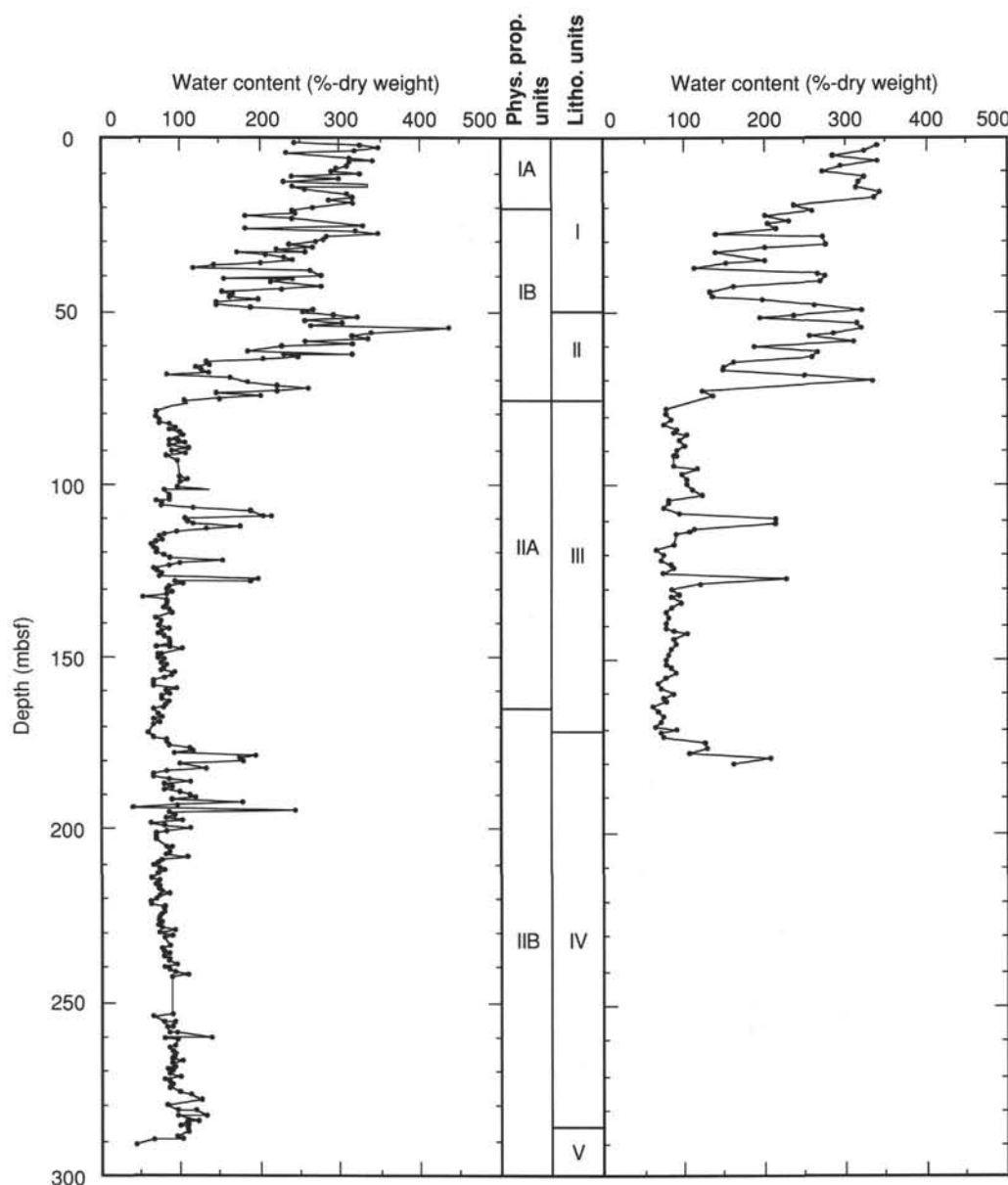
Figure 39. Water content (% dry weight) vs. depth, Holes 844B (left) and 844C (right). Lithologic and physical property units are shown for comparison.

Mayer, L. A., Theyer, F., Thomas E., et al., 1985. *Init. Repts. DSDP*, 85: Washington (U.S. Govt. Printing Office).

McDuff, R. E., 1981. Major cation gradients in DSDP interstitial waters: the role of diffusive exchange between seawater and the upper ocean crust. *Geochim. Cosmochim. Acta*, 45:1705–1713.

McDuff, R. E., and Gieskes, J. M., 1976. Calcium and magnesium in DSDP interstitial waters: diffusion or reaction? *Earth Planet Sci. Lett.*, 33:1–10.

Mountain, G. S., and Tucholke, B. E., 1983. Abyssal sediment waves. *In* Bally, A. W. (Ed.), *Seismic Expressions of Structural Styles*. AAPG Stud. Geol., 15.

Okada, H., and Bukry, D., 1980. Supplementary modification and introduction of code numbers to the low-latitude coccolith biostratigraphic zonation (Bukry, 1973; 1975). *Mar. Micropaleontol.*, 5:321–325.

Rio, D., Fornaciari, E., and Raffi, I., 1990. Late Oligocene through early Pleistocene calcareous nannofossils from western Equatorial Indian Ocean (Leg 115). *In* Duncan, R. A., Backman, J., Peterson, L. C., et al., *Proc.*

ODP, Sci. Results, 115: College Station, TX (Ocean Drilling Program), 175–235.

Tucholke, B. E., and Laine, E. P., 1982. Neogene and Quaternary development of the lower continental rise off the central U.S. east coast. *In* Watkins, J. S., and Drake, C. L. (Eds.), *Studies in Continental Margin Geology*. AAPG Mem., 34:295–307.

Vincent, E., 1981. Neogene carbonate stratigraphy of Hess Rise, central North Pacific and paleoceanographic implications. *In* Larson, R. L., Moberly, R., et al., *Init. Repts. DSDP*, 32: (U.S. Govt. Printing Office), Washington, D.C., 571–606.

Wyrtki, K., 1965. Surface currents of the Eastern Tropical Pacific Ocean. *Bull. Inter-Am. Tropical Tuna Comm.*, 9:271–304.

Ms 138A-109

NOTE: For all sites drilled, core description forms ("barrel sheets") and core photographs have been reproduced on coated paper and can be found in Section 4, beginning on page 397. Forms containing smear-slide data can be found in Section 5, beginning on page 663.

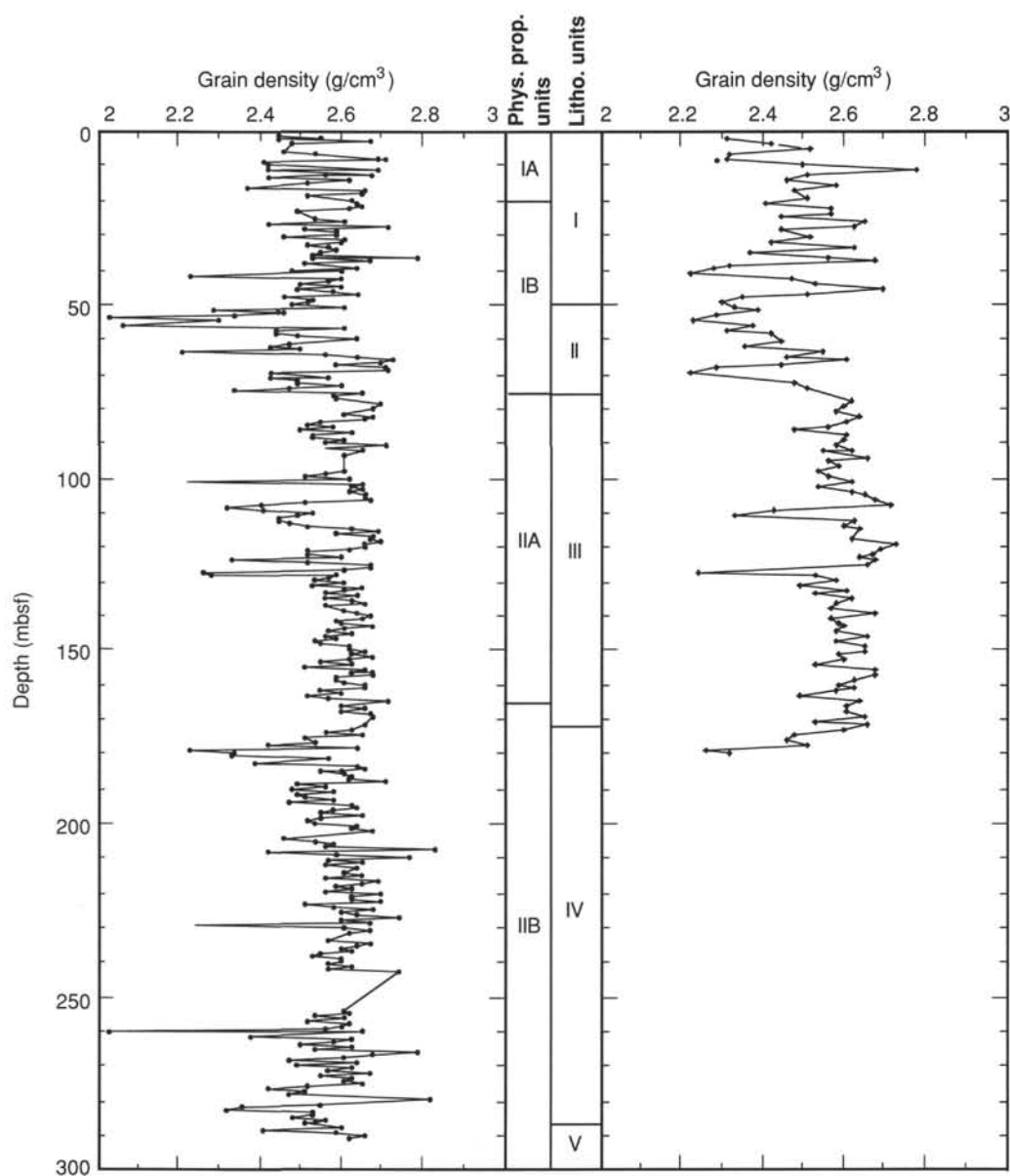**Formation microscanner images for this site are presented on microfiche in the back of Part 2.**

Figure 40. Grain density vs. depth, Holes 844B (left) and 844C (right). Lithologic and physical property units are shown for comparison.
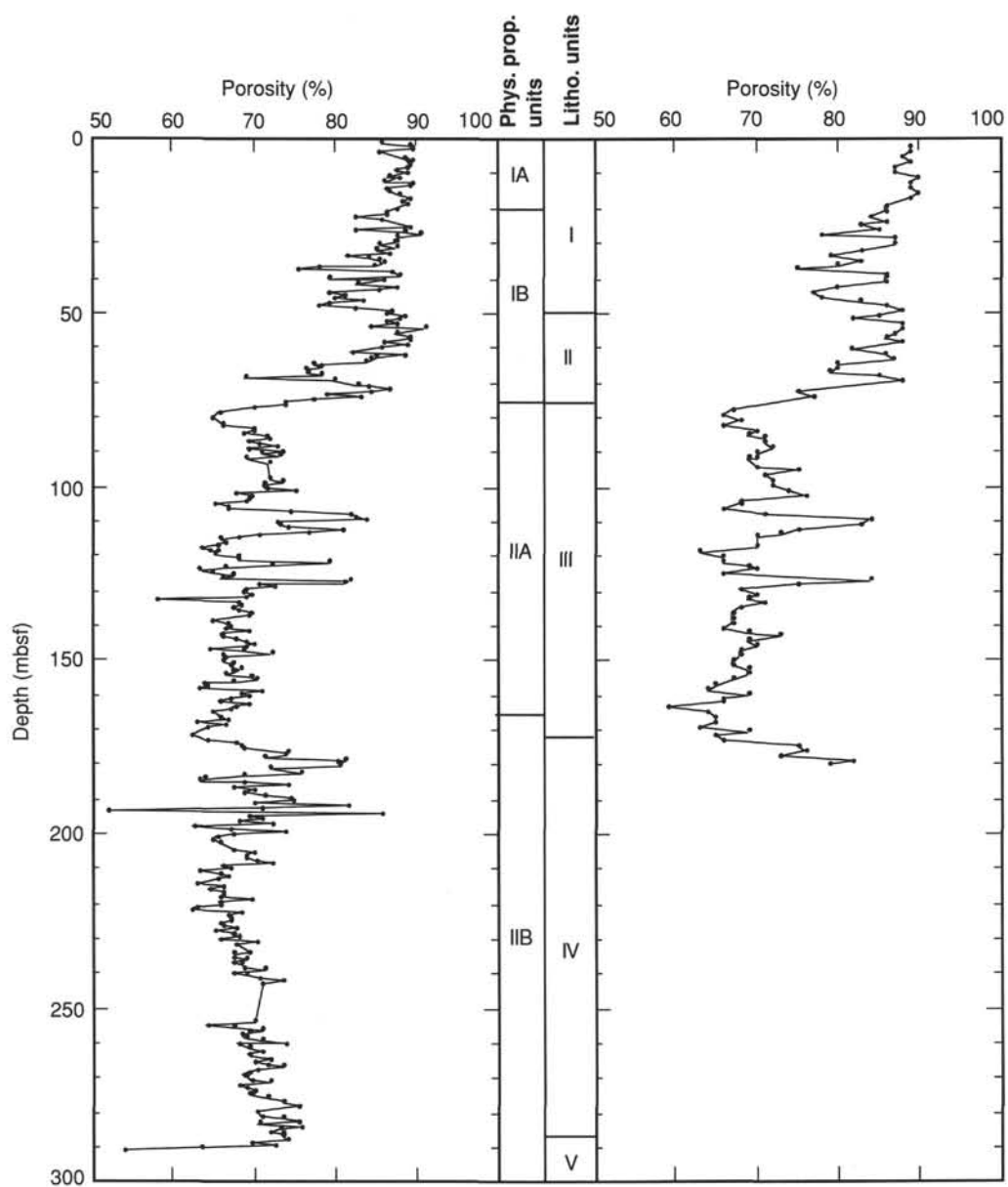
Figure 41. Porosity vs. depth, Holes 844B (left) and 844C (right). Lithologic and physical property units are shown for comparison.
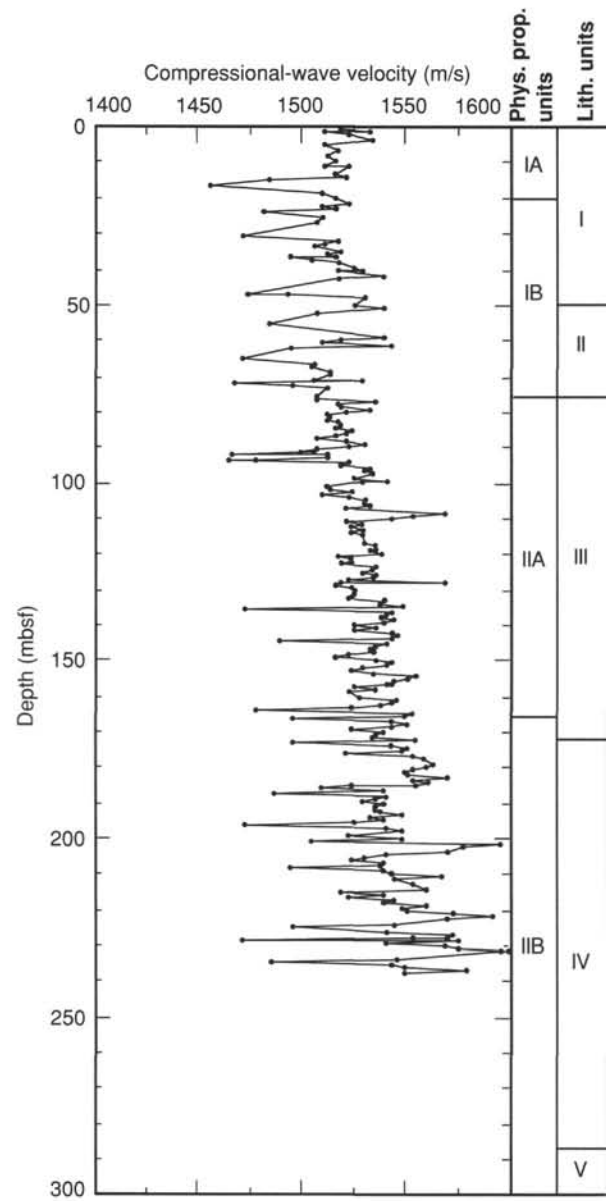
Figure 42. Compressional-wave velocity vs. depth, Hole 844B. Lithologic and physical property units are shown for comparison.
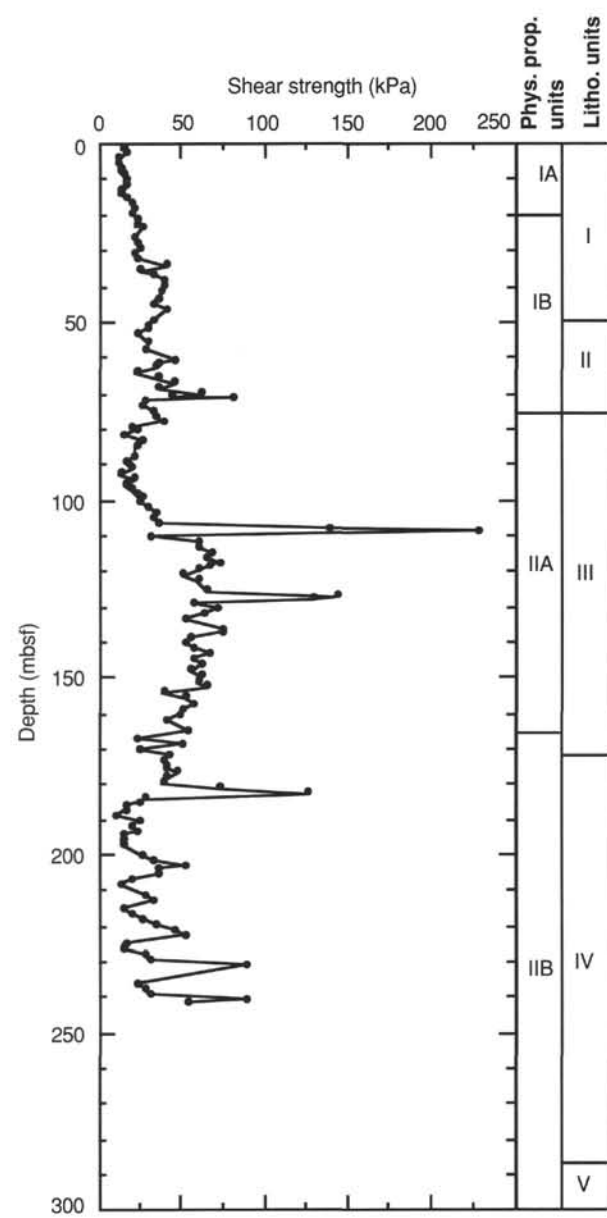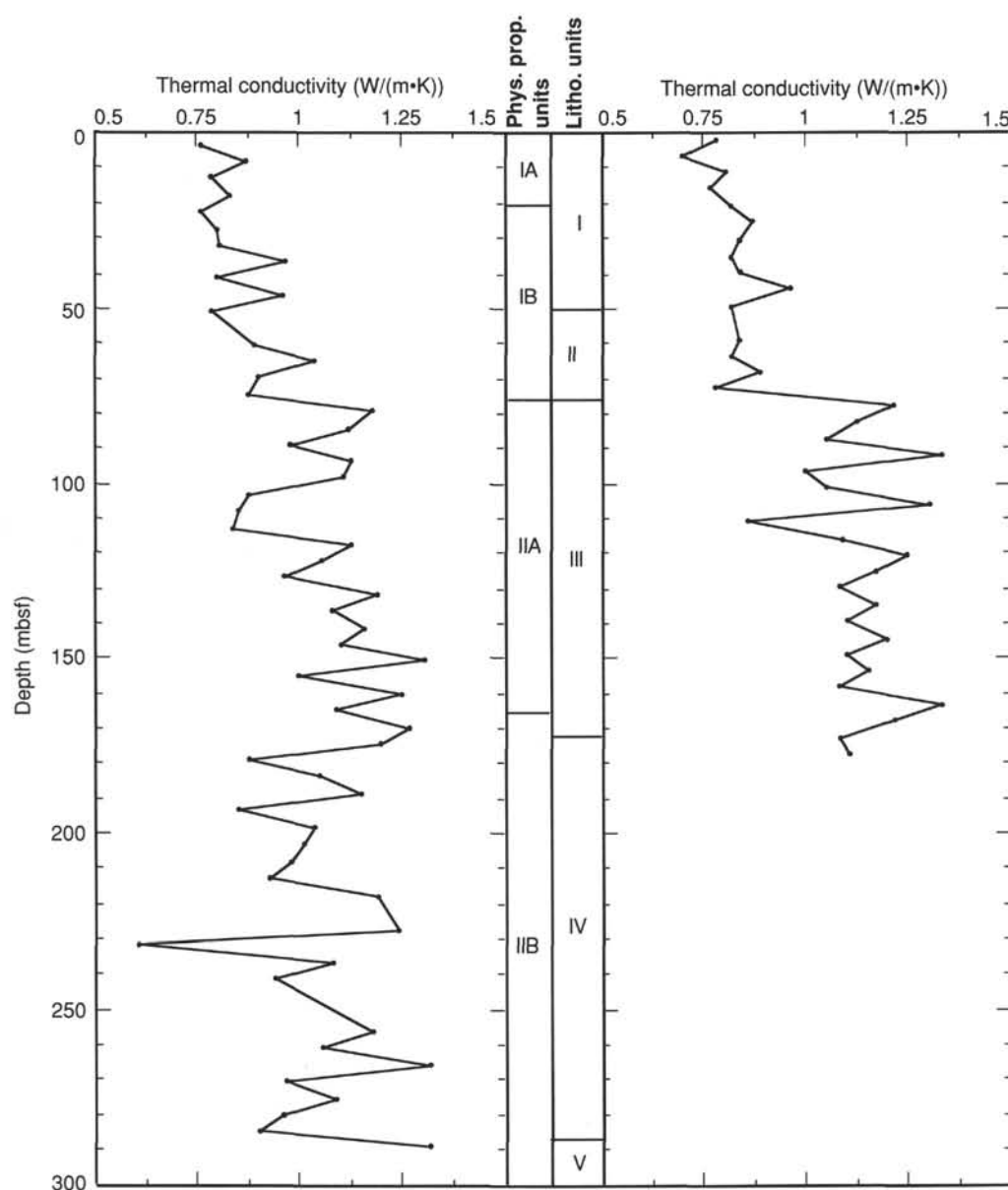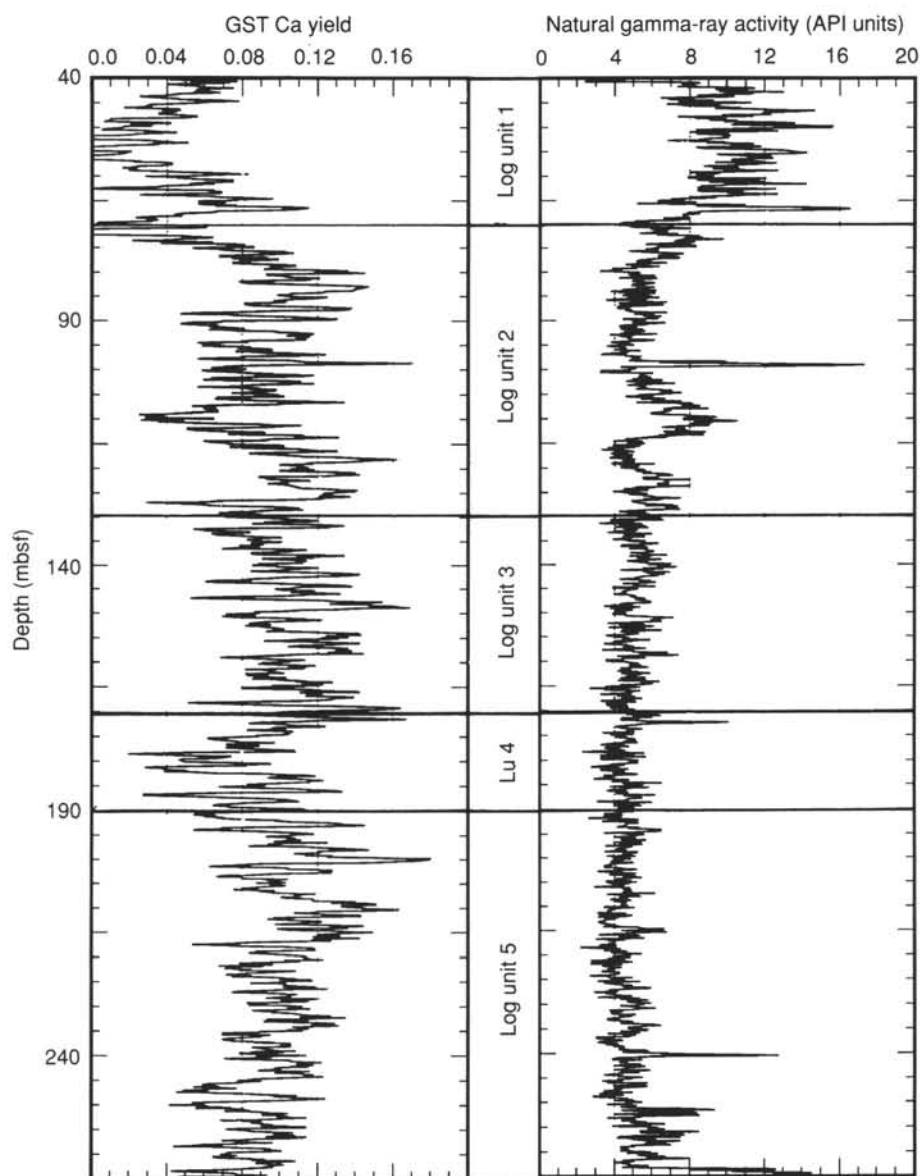

Figure 43. Undrained shear strength vs. depth, Hole 844B. Lithologic and physical property units are shown for comparison.

Figure 44. Thermal conductivity vs. depth, Holes 844B (left) and 844C (right). Lithologic and physical property units are shown for comparison.

Figure 45. Variations of Ca (represented by Ca yield from GST) and natural gamma-ray activity down Hole 844B. Log-derived stratigraphic units also are marked.
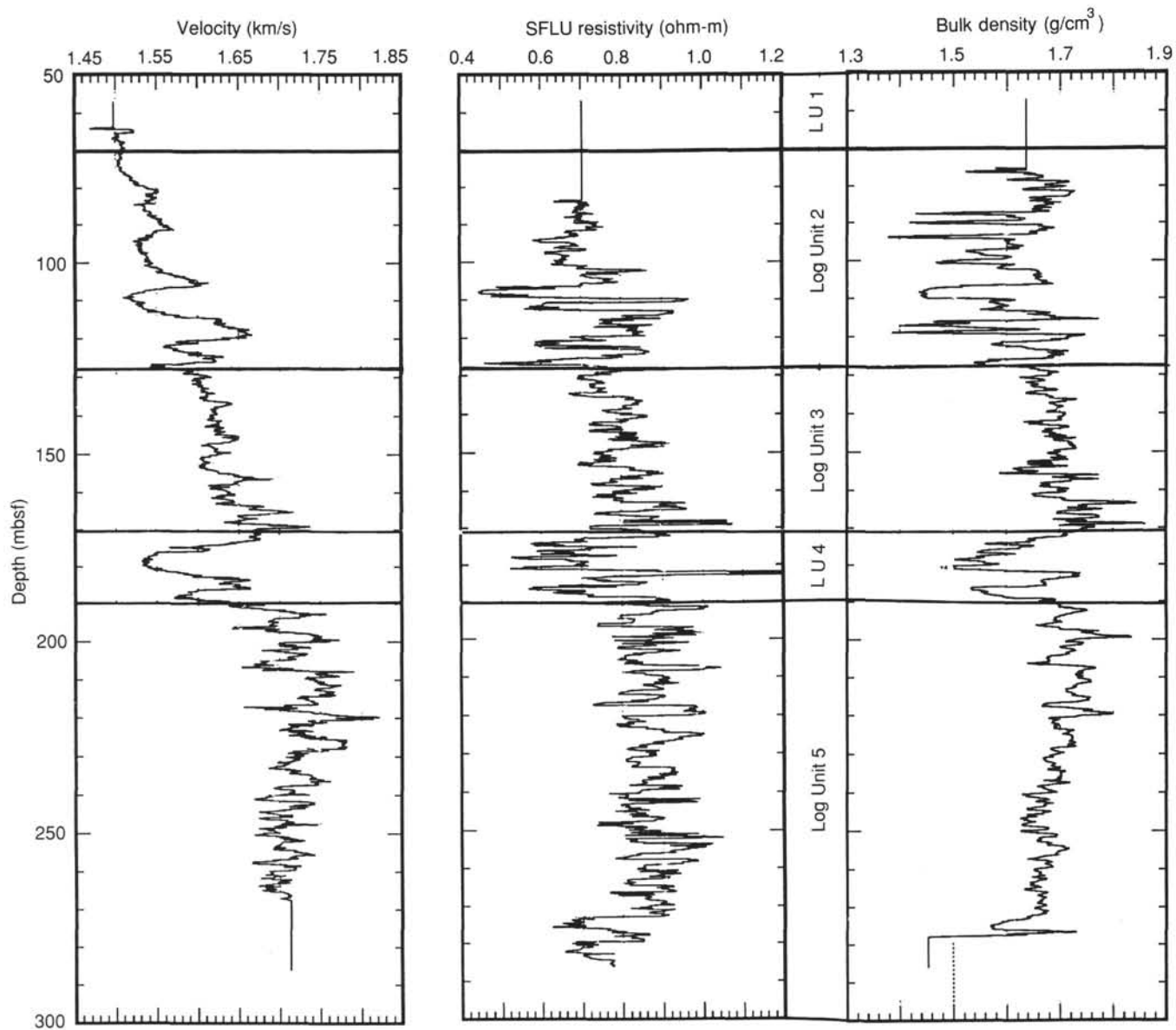
Figure 46. Variations of sonic velocity, wet-bulk density, and resistivity down Hole 844B. Log-derived stratigraphic units also are marked.
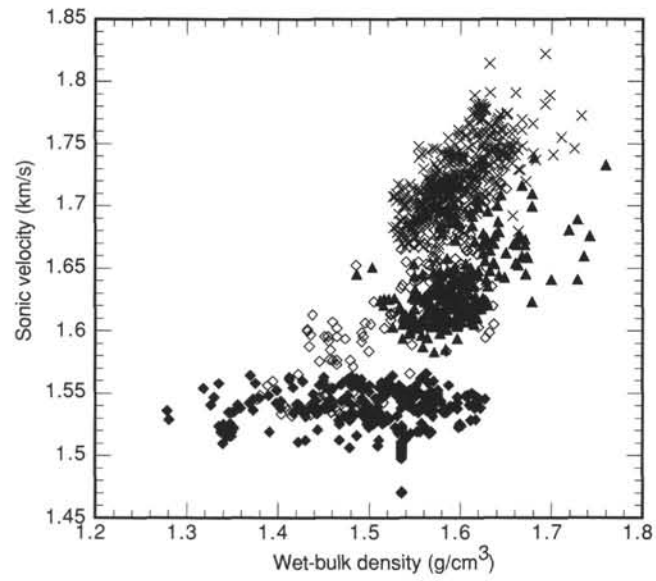
Figure 47. Cross plot of sonic velocity vs. wet-bulk density, showing rationale behind chosen log stratigraphic units. Solid diamond = log Unit 2 (70–128 mbsf); solid triangle = log Unit 3 (128–172 mbsf); open diamond = log Unit 4 (172–190 mbsf); cross = log Unit 5 (190–base of hole).
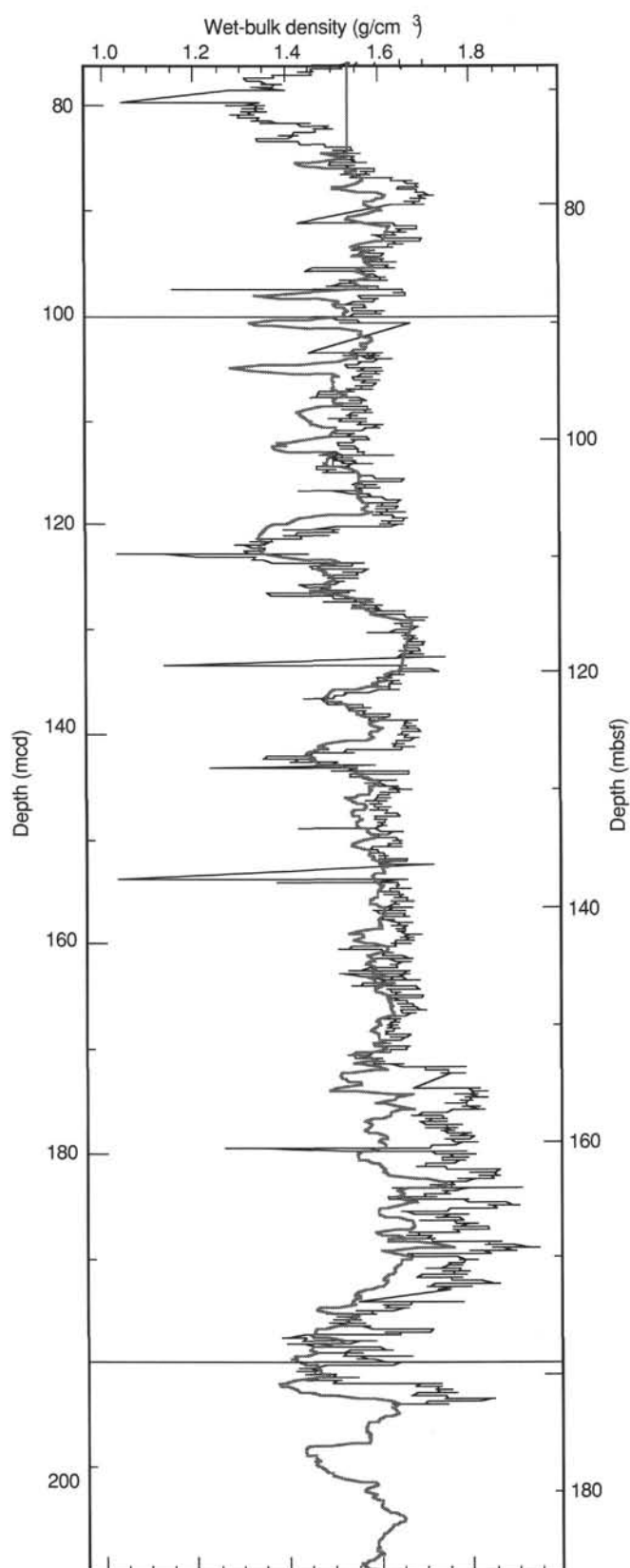
Figure 48. Comparison of HLDT log bulk density (gray line) with continuous
GRAPE bulk density (thin solid line) measured in recovered core. GRAPE data
are plotted using composite depth scale (see "Sedimentation Rates" section,
this chapter), while log data are plotted using ODP mbsf scale. Note that
composite depth scale has been stretched by an approximately linear factor of
9.9% with respect to mbsf scale. Note also that GRAPE data are consistently
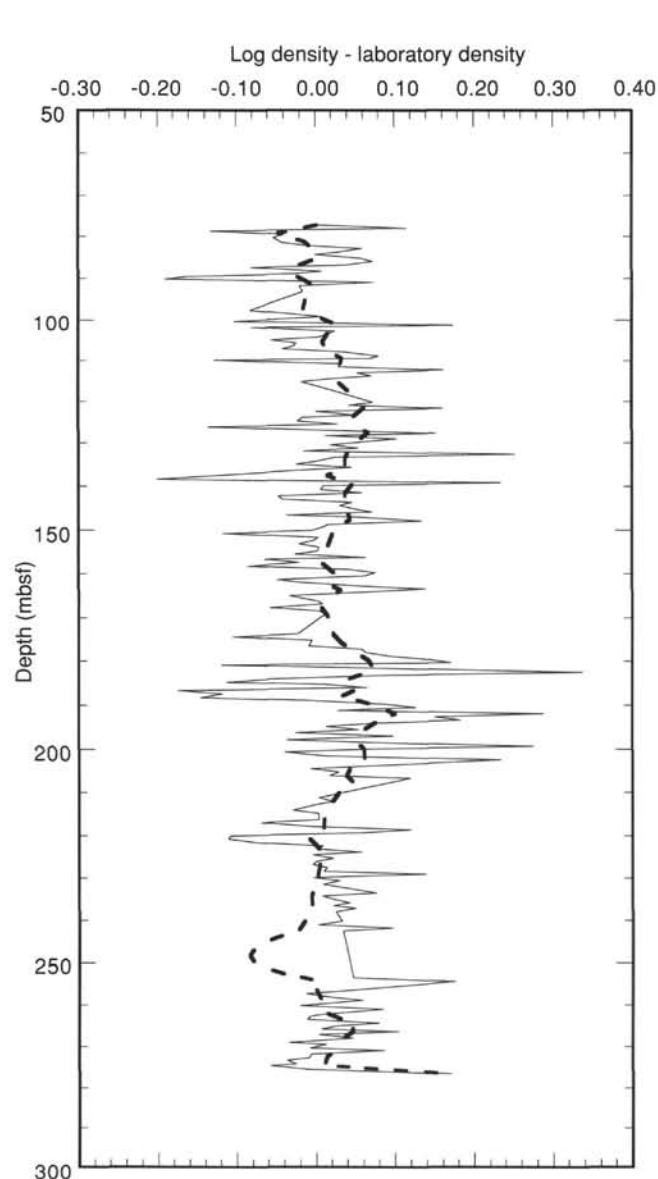higher than logging data for the same intervals.

Log density - laboratory density

Figure 49. Difference between wet-bulk density measured using logs and shipboard physical properties measurements at Hole 844B (solid line). Laboratory data have consistently lower measurements, because cores decompressed during retrieval from below the seafloor. The amount of difference between *in-situ* logging data and shipboard measurements seems to depend on lithology. Dashed line = smoothed average.
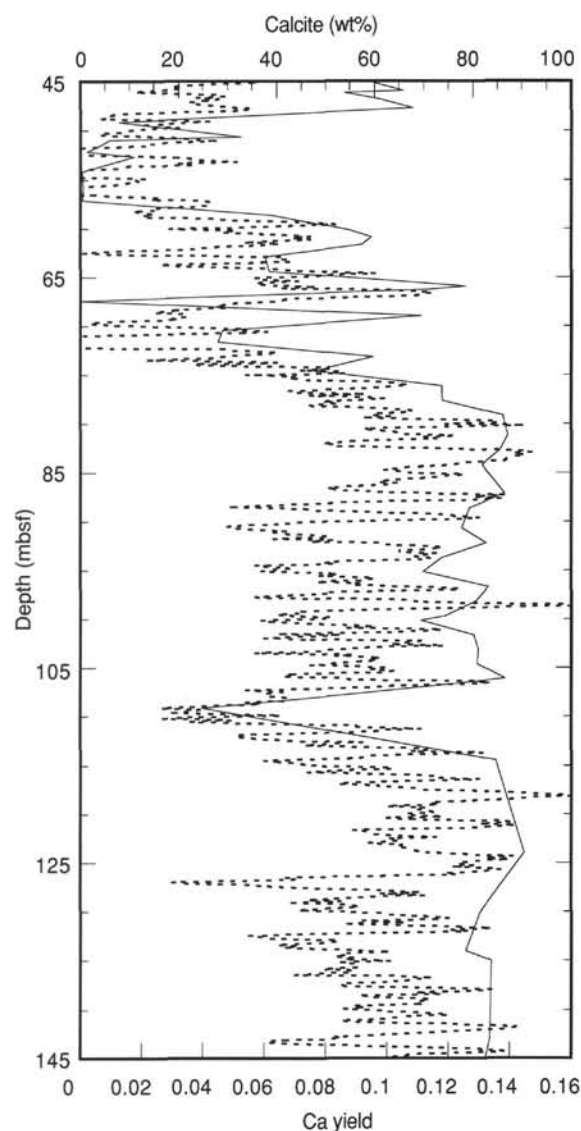
Calcite (wt%)

Ca yield

Figure 50. Comparison of GST Ca yield (dashed line) with shipboard carbonate measurements using coulometer (solid line) at Hole 844B. Axis on Ca yield was expanded until the two records have approximately the same amplitude. This comparison shows that events can be found on both records and implies that a good log-based calcite record may be obtained.
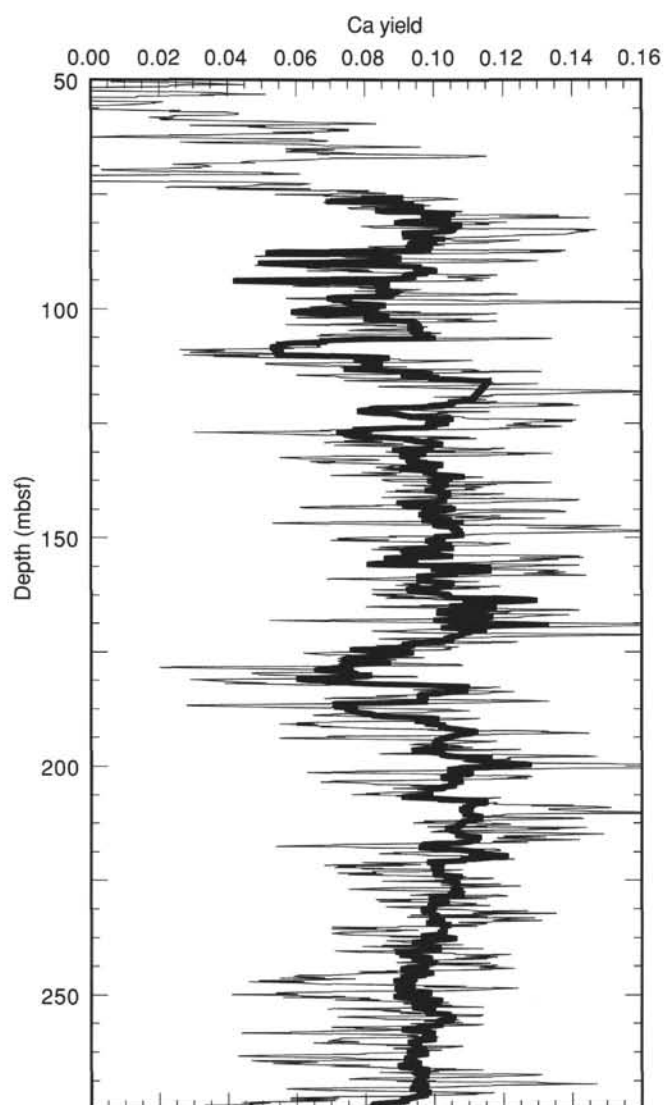
Figure 51. Comparison of GST Ca yield (thin solid line) with an estimated Ca yield from a linear regression of log bulk density (thick line). Mayer (1991) showed that bulk density should be a good predictor of calcium carbonate in the eastern tropical Pacific Ocean.
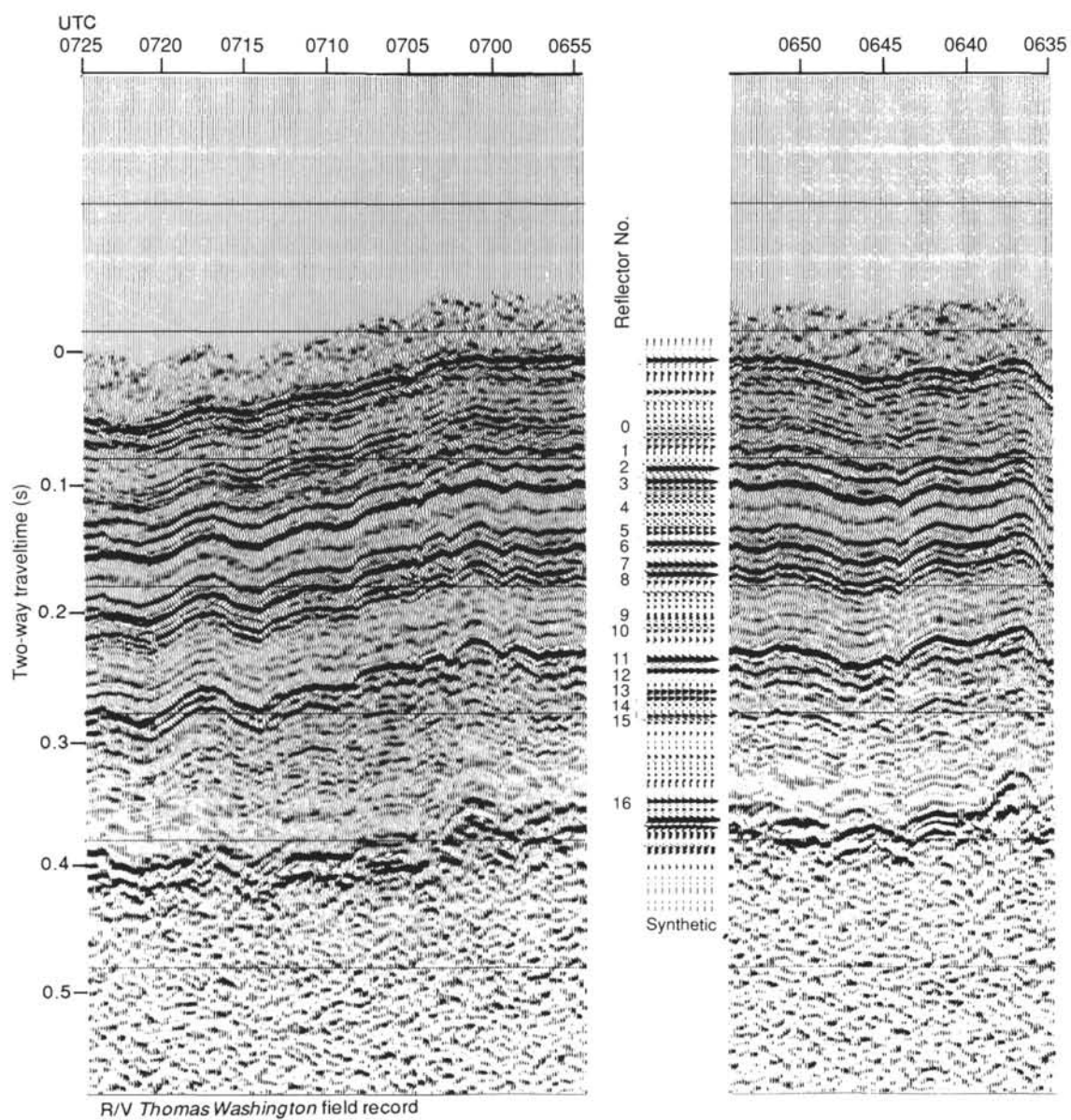
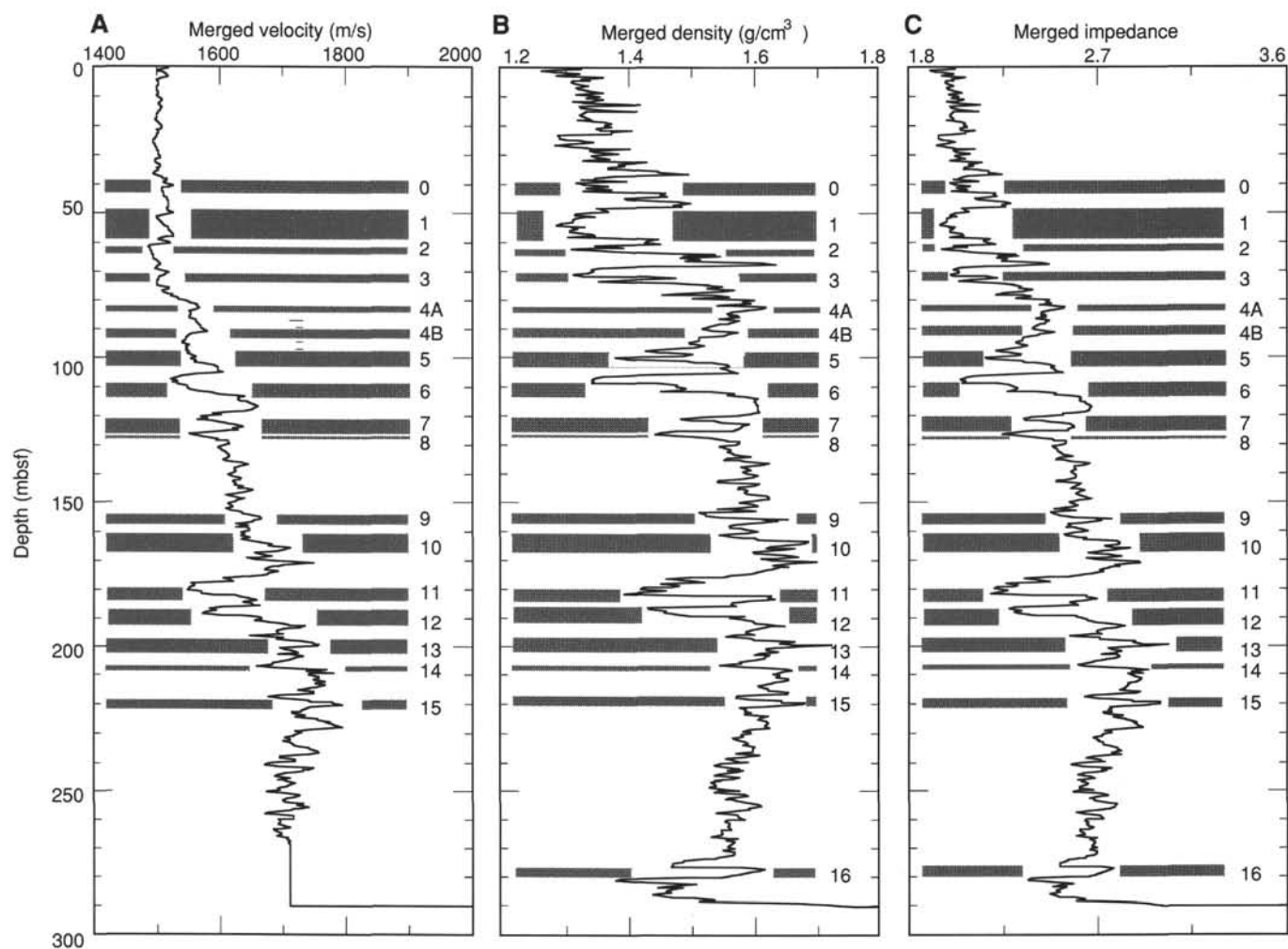Figure 52. Comparison of synthetic seismogram with field record, Site 844.

Figure 53. Velocity (**A**), density (**B**), and acoustic impedance (**C**) data used for generating Site 844 synthetic seismograms. The 17 reflectors selected from the synthetic seismogram are shown for comparison.

Table 21. Well-log data, Hole 844B.

Log type	Depth (mbsf)
Resistivity	77.5–287.8
Bulk density	77.2–279.7
Sonic velocity	65.5–269.4
Sonic waveforms	65.5–269.4
Gamma ray/U-Th-K	00.0–287.3
Aluminum	00.0–274.4
Geochemistry	00.0–285.0
Caliper	66.2–290.1
Formation microscanner	66.2–290.1
LDGO temperature	00.0–290.1

Note: Data assumes seafloor at 3425.0 mbrf and all logs correlated; depth shifted to the FMS gamma-ray log.

**Table 22. Summary of traveltimes, depths, and ages for Site 844 reflectors.**

Reflector	Traveltime (sec)	Synthetic depth (m)	Depth (mbsf)	Depth (mcd)	Age (Ma)
R0	0.053	39.80	40.00	43.65	6.60
	0.057	42.80	43.00	46.65	6.89
R1	0.068	51.30	50.00	54.10	7.65
	0.076	57.30	60.00	66.70	9.21
R2	0.085	64.00	63.00	70.15	9.60
	0.089	67.00	65.00	72.15	9.67
R3	0.096	72.30	72.00	80.65	10.54
	0.104	78.30	75.00	83.65	10.71
R4	0.112	84.50	83.50	94.13	10.92
	0.123	93.10	94.00	107.50	11.30
R5	0.132	100.00	99.00	112.50	11.44
	0.139	105.50	104.00	117.50	11.58
R6	0.145	110.20	110.00	123.80	11.75
	0.149	113.30	115.00	128.80	11.89
R7	0.161	123.00	122.50	137.30	12.13
	0.166	127.00	127.00	141.80	12.26
R8	0.169	129.40	127.50	142.30	12.27
	0.174	133.40	130.00	145.00	12.35
R9	0.201	155.40	155.00	170.60	13.07
	0.206	159.40	158.00	175.05	13.19
R10	0.209	161.90	162.00	179.05	13.30
	0.217	168.80	168.00	185.20	13.48
R11	0.232	180.90	181.00	199.60	13.97
	0.238	185.70	184.00	202.60	14.08
R12	0.243	189.80	187.00	205.60	14.18
	0.248	193.90	193.00	211.60	14.39
R13	0.255	199.90	198.00	216.60	14.56
	0.263	206.70	202.00	220.60	14.70
R14	0.266	209.30	207.50	226.10	14.89
	0.270	212.80	209.00	228.10	14.96
R15	0.280	221.40	219.00	237.60	15.29
	0.283	224.00	222.00	240.60	15.39
R16	0.345	277.20	277.00	295.60	16.97
	0.350	281.40	281.00	299.60	17.00
Basement	0.360	290.00	290.00	308.60	17.30

Table 23. Paleolatitudes for Site 844.

Pole of rotation: 21.9°N 115.5°W
Angluar Velocity: - 0.948,/ m.y.

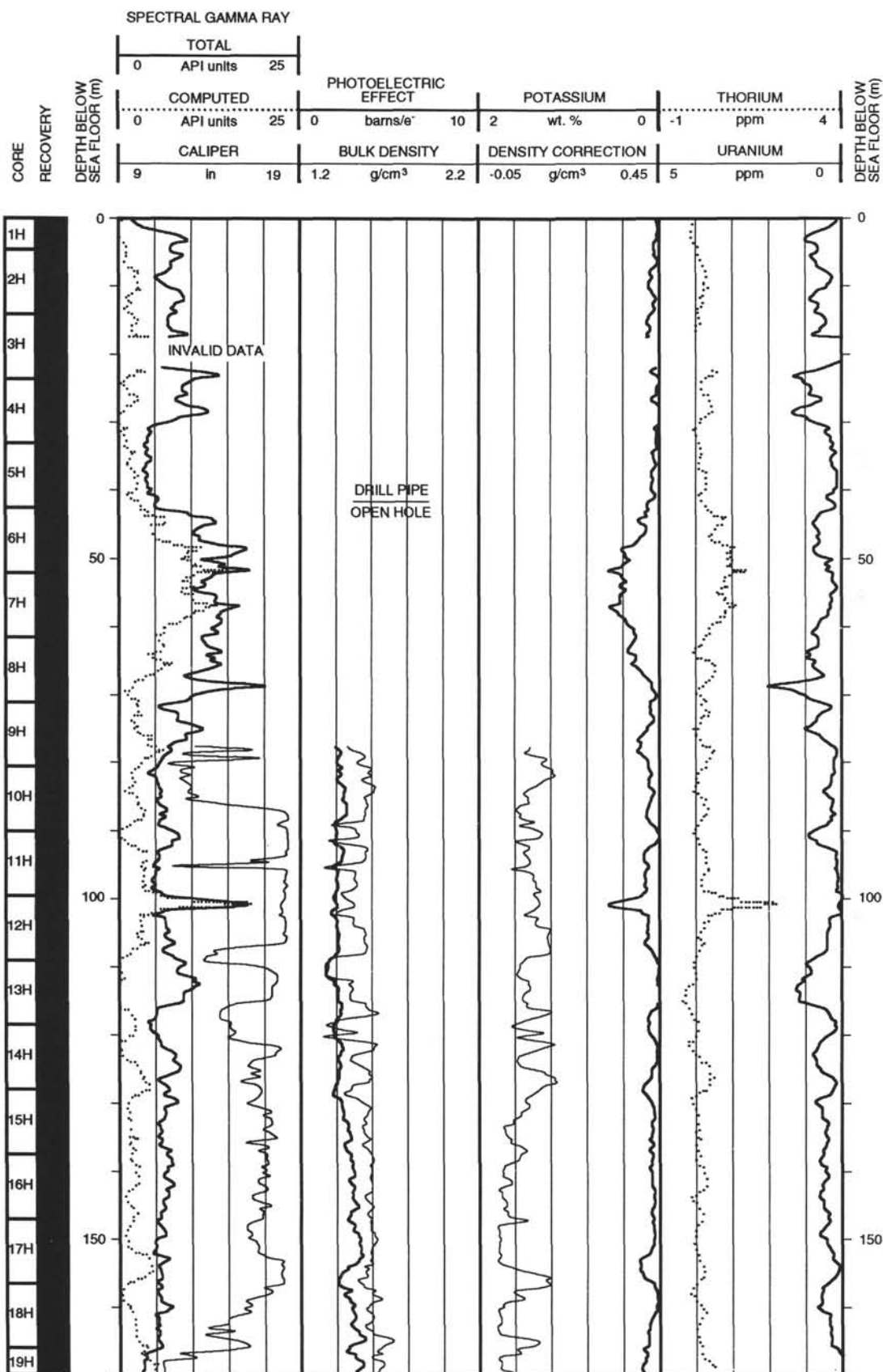| Age (Ma)	Latitude (°N)
0	7.90
1	7.53
2	7.16
3	6.79
4	6.43
5	6.07
6	5.72
7	5.37
8	5.02
9	4.68
10	4.34
11	4.00
12	3.67
13	3.34
14	3.02
15	2.71
16	2.39
17	2.08

Hole 844B: Resistivity-Sonic-Natural Gamma Ray Log Summary
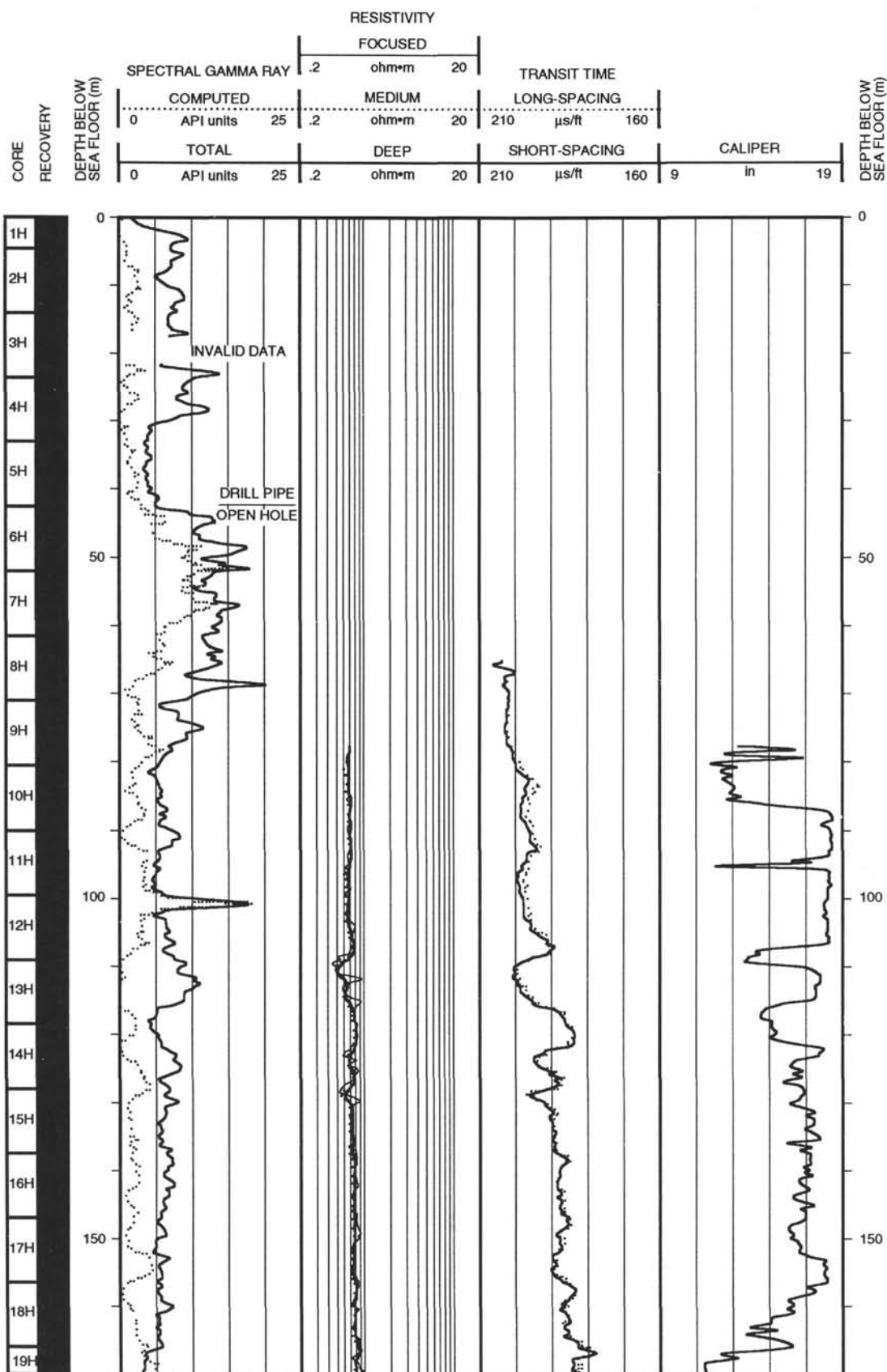
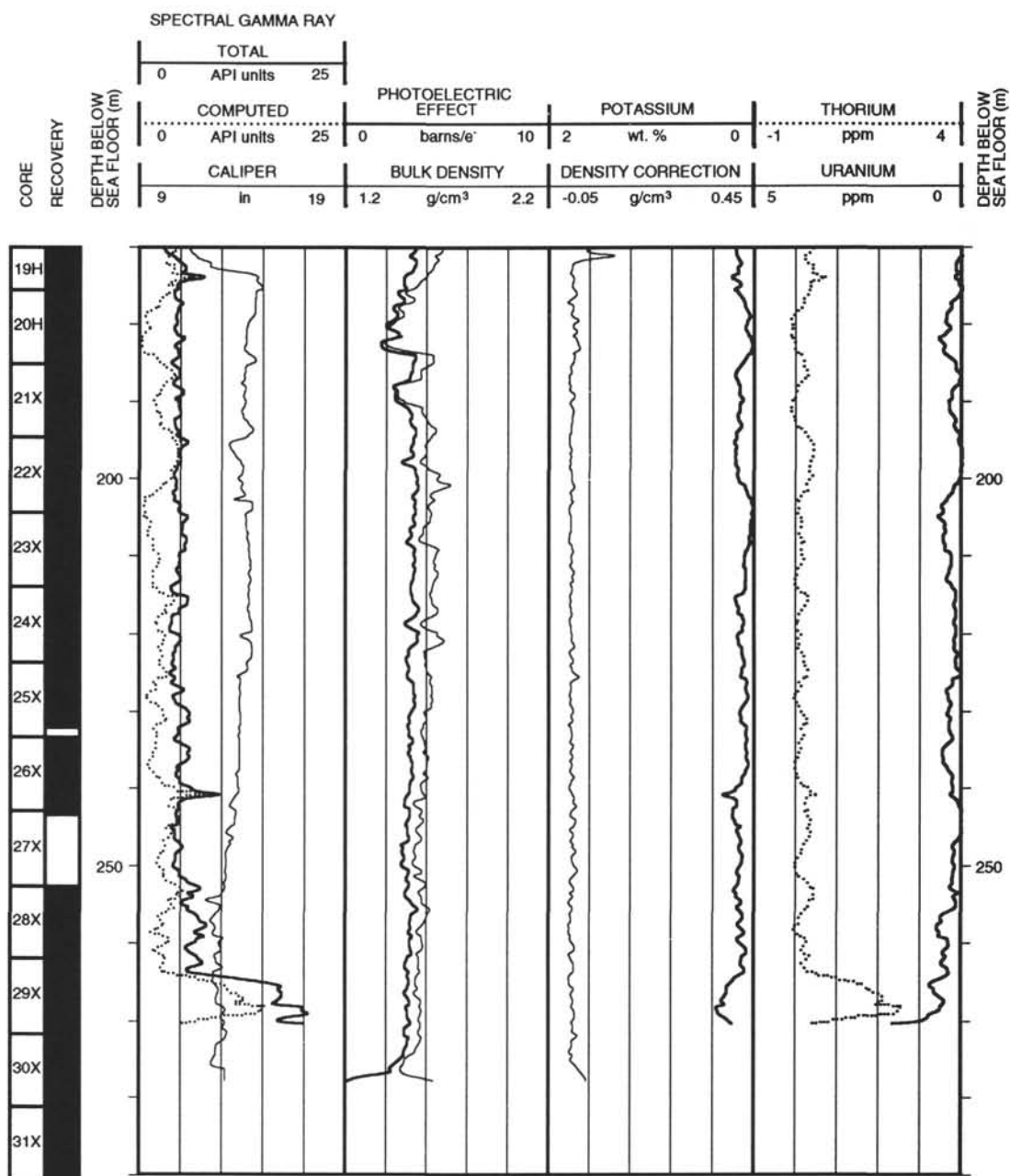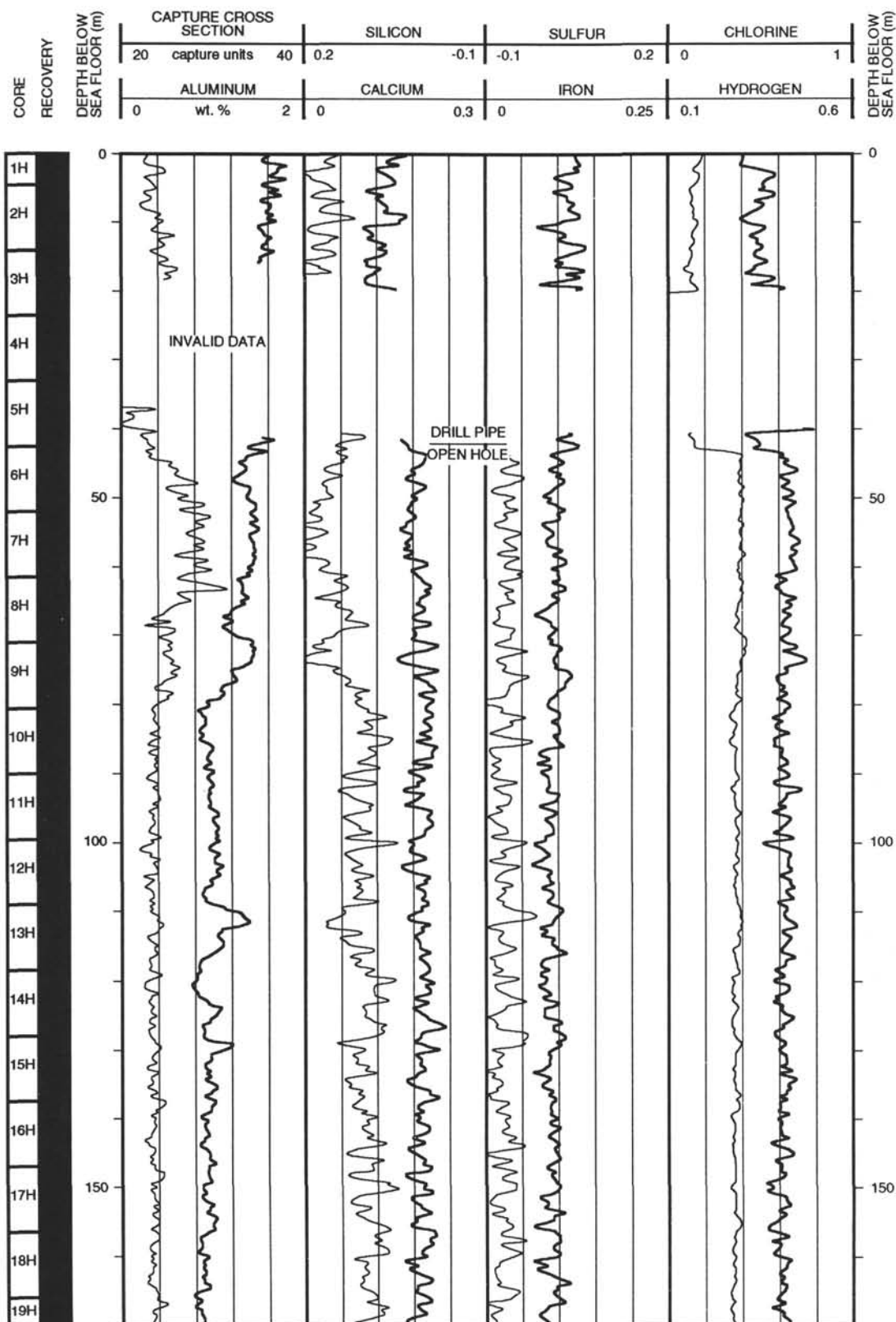Hole 844B: Resistivity-Sonic-Natural Gamma Ray Log Summary (continued)
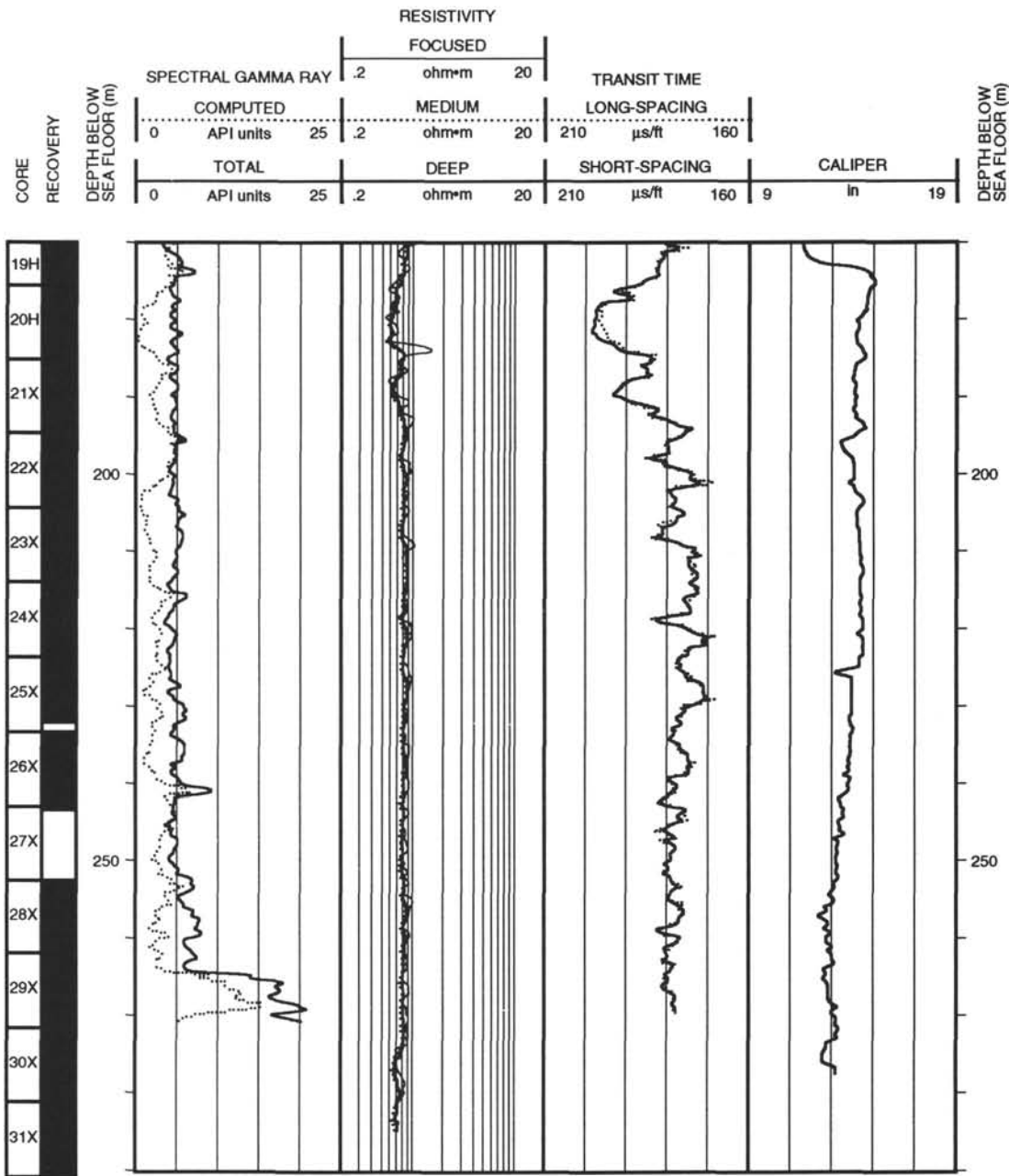
Hole 844B: Density-Natural Gamma Ray Log Summary

Hole 844B: Density-Natural Gamma Ray Log Summary (continued)

Hole 844B: Geochemical Log Summary

Hole 844B: Geochemical Log Summary (continued)